

https://dspace.org/

# Polymorphism and structural studies of isoniazid derivatives

**Hean, Duane**

**2015-05-21**
http://hdl.handle.net/10539/18526

Downloaded from a DSpace repository. https://dspace.org/

# Polymorphism and Structural Studies of Isoniazid Derivatives

Duane Hean

A Dissertation submitted to the Faculty of Science, University of the Witwatersrand, Johannesburg, in fulfilment of the requirements for the degree of Master of Science

signed on 21 May 2015 in Johannesburg

**DECLARATION**

I declare that this Dissertation is my own, unaided work. It is being submitted for the Degree of Master of Science at the University of the Witwatersrand, Johannesburg. It has not been submitted before for any degree or examination at any other University.



_____

(Signature of candidate)

21 day of May in 2015

## ABSTRACT

Crystal polymorphism is the capacity of a solid crystalline form to exist in more than one structural arrangement. In the pharmaceutical setting investigations into the polymorphic forms of potential drugs are of vital importance since different crystalline forms can affect bioavailability, mechanical, thermal, and chemical properties. One such example is isonicotinic acid-(1-phenylethylidene) hydrazide (IPH), a derivative of the popular drug isoniazid (used as first line treatment against *Mycobacterium tuberculosis*) was found to crystallise in six different polymorphic forms. Each crystal structure was determined using X-ray diffraction techniques and including the thermal phase relationships of the polymorphic compound were delineated. In addition to polymorph elucidation, isonicotinic acid-(1-phenylethylidene) hydrazide was modified with –OH and $–NH_2$ at various aromatic positions, creating geometric pyridyl isomers. In-depth studies of these pyridyl isomers revealed a diverse range of supramolecular aggregates. Preliminary thermal screening suggests that only a small selection of these pyridyl isomers present potential polymorphic activity for further study.

**ACKNOWLEDGEMENTS**

Special acknowledgements are given to Prof. Joseph P. Michael and Dr Andreas Lemmerer for nurturing a young undergraduate student into a competent post-graduate student. Additional thanks are also given to the Wits Structural Group for their support throughout the Master's duration as well as to the School of Chemistry for providing superb education during my undergraduate years. On a final note I would like to thank the National Research Foundation for funding throughout my post-graduate years and to the University of the Witwatersrand for giving me the edge.

## LIST OF ABBREVIATIONS

**CSD:** Cambridge Crystallographic Structural Database

**DSC:** Differential Scanning Calorimetry

**IPH**: Isonicotinic acid-(1-phenyl-ethylidene) hydrazide

**IR**: Infrared Spectroscopy

**IUPAC**: International Union of Pure and Applied Chemistry

**HSM**: Hot-stage Microscopy

**PXRD**: Powder X-ray Diffraction

**SCXRD**: Single Crystal X-ray Diffraction

## LIST OF FIGURES

**Figure 1**: Parent structure of the nicotinamide based anti-TB drug isoniazid. ..... 1

**Figure 2**: Isonicotinic acid-(1-phenylphenylethylidene) hydrazide (IPH) prepared from isoniazid and acetophenone. ..... 1

**Figure 3**: Pyridyl isomers of isoniazid: nicotinic acid hydrazide (A) and picolinic acid hydrazide (B). ..... 2

**Figure 4:** Hydrogen bond bridges. a) Typical hydrogen bond with a single donor and acceptor. b) Bifurcated hydrogen bond with two acceptors. c) Trifurcated hydrogen bond involving a single donor with three acceptors. ..... 4

**Figure 5:** A schematic representation of the hydrogen bond potential energy versus distance between donor and acceptor atoms, *d*. Taken from reference 26. ..... 5

**Figure 6**: The metastable state (1) then moves to a transitional configuration (2) and finally to a stable state having minimum energy (3). Taken from reference 46. ..... 6

**Figure 7**: Free energy vs. temperature diagrams for the enantiotropic (left) and monotropic (right) systems for solid phases of polymorphic forms A and B. The enthalpies (heats of fusion) are represented with red arrows. Taken from reference 61. ..... 7

**Figure 8**: The asymmetric units of IPH **I** – **VI**. The displacement ellipsoids are drawn at 50% probability level. H on C atoms are omitted for clarity. ..... 15

**Figure 9**: Packing arrangements of IPH **I** – **VI** viewed along their respective axes. IPH **I** demonstrates significant twisting of the pyridine ring relative to the carbonyl motif to facilitate dimerization hydrogen bonding. A common chain hydrogen bond motif is observed throughout the remaining polymorphs (with exception to IPH **II** co-forming a dimer by hydrogen bonding). Despite this commonality the unit cell parameters differ from polymorph to polymorph. ..... 16

**Figure 10**: Hydrogen bond patterns for polymorphs IPH **I** – **VI**. These hydrogen bond patterns are used as a point of reference to juxtapose the conformational twisting of each polymorph. ..... 17

**Figure 11**: Plate-like crystal of IPH recovered from bulk recrystallization. Photograph a) shows IPH **V** before onset transition temperature (129°C), whilst b) shows the transition with the encroaching wave front (yellow arrows) in the crystal. c–d) shows the progress of the phase transition until the crystal has completely transformed into IPH **III**. ..... 18

**Figure 12**: Thin-film photo micrographs of the phase transition cycle of IPH as observed on the polarised microscope. The cycle begins by recrystallization from melt, producing concomitant forms IPH **I**, **III**, **IV** and **VI**. Upon commencement of the heating cycle, the first phase transition (145°C) follows the encroaching wave front (red arrows) where IPH **IV** and **VI** transform into IPH **III**. This phase transition continues until IPH **IV** and **VI** are completely transformed into IPH **III** and **I**. The second phase transition (155°C) occurs with IPH **III** converting into IPH **I** until the sample is dominated by IPH **I**. Melting of IPH occurs with the onset of 173°C, and subsequent cooling allows for recrystallization and completion of the phase transition cycle. ..... 19

**Figure 13**: Recrystallised islands of IPH and subsequent slow heating. Photograph a) shows pronounced recrystallization of IPH **IV**; b) shows concomitant recrystallization of IPH **III**, **IV** and **VI**; c) shows the onset of melting of IPH **VI** at 145°C, while a phase transition of IPH **VI** to **III** marked by red arrows occurs; d) shows the completion of the phase transition with the onset of 155°C. Finally, melting of IPH **III** (onset of 165°C) is shown in e) and f). ..... 20

**Figure 14**: Super-cooled amorphous solid after quench cooling from melt. Photograph a) shows the amorphous solid with intentional breakage exemplifying rigidity; b) and c) show melting with the onset of 65°C of the amorphous solid with the presence of seed crystallites of IPH **I**; d) shows completed recrystallization of IPH **I**. ..... 21

**Figure 15**: DSC traces of five successive heating /cooling runs beginning with IPH **V**. The initial trace shows the first phase transition (trs) from IPH **V** to **III** followed by a second phase transition of IPH **III** to **I**, and finally melting endotherm of IPH **I**. This is followed by the recrystallization of forms IPH **I**, **III**, **IV** and **VI** during the cooling runs. The second heating cycle shows phase transition of IPH **IV**, **VI** to **III** at 145°C and IPH **III** to **I** at 165°C respectively. The following heating/cooling cycles repeat the $2^{nd}$ and $3^{rd}$ heating and cooling cycles. The heating rate is 15 K/min. ..... 22

**Figure 16**: DSC trace of heating run for the super-cooled amorphous solid. At 65°C, a broad exothermic peak is observed, indicating a phase transition to IPH **I**. This is followed by eventual melting of IPH **I**. ..... 23

**Figure 17**: The asymmetric units **1** – **6**. The displacement ellipsoids are drawn at 50 % probability level; H on C atoms are excluded for clarity. ..... 26

**Figure 18**: The asymmetric units **7** – **13** with **11** excluded. The displacement ellipsoids are drawn at 50 % probability level. H on C atoms are excluded for clarity. Note that 13 is the only 2-pyridyl modification made. ..... 27

**Figure 19**: (a) Hydrogen bond motif of **1**, where molecule A and B interchangeably form a hydrogen bond chain. (b) Viewing along the *b*-axis, the alignment of the backbone with the phenyl ring is observed. ..... 31

**Figure 20**: (a) Two hydrogen bond columns are formed, including larger hydrogen bond rings are formed between connecting the columns by utilising the phenol donor in the *meta* position of the phenyl ring in **2**. (b) Viewing along the *b*-axis, the hydrogen bond rings are observed as well as the chains running along the *ac* direction. ..... 32

**Figure 21**: Compound **3** forms a 2D hydrogen bond array with amide donor and phenol donor in the *para* position. ..... 32

**Figure 22**: Packing representations of compound **4**. (a) With pyridyl nitrogen in the 3-position; parallel hydrogen bond chains are formed from symmetry independent molecules A and B. The hydrogen bond chains run along the *a*-axis with the pyridine rings involved in π···π interactions. (b) Hydrogen bond chains for A and B form along the *a* axis whilst these columns pack along each other along the *c* direction and alternate between column A and B along the *b* axis. (c) π···π interactions between phenol rings of molecule A and B are observed. ..... 33

**Figure 23**: Packing representations for compound **5**. (a) Hydrogen bond chains are observed with the *meta* positioned phenol donor and 3-positioned pyridyl nitrogen. (b) A head-to-tail molecular aggregate is observed running along the *c*-axis. ..... 34

**Figure 24**: (a) Compound **6** forms a 2D sheet of hydrogen bonds by utilising the amide donor and carbonyl acceptor pair along with the phenol donor and pyridyl *N* pair. By utilising six hydrogen bonded molecules, a larger ring is formed with graph set notation $R66(40)$ while the centre of this ring formation provides further linkage of neighbouring molecules. (b) The head-to-tail molecular aggregation is observed with the hydrogen bond chains running in the *a* and *c* axis. ..... 34

**Figure 25**: (a) Compound **7** possesses the greatest number of hydrogen bonds amongst the isoniazid derivatives and forms a 2D hydrogen bond chain array. (b) The 2D hydrogen sheets are demonstrated extending along the *a* and *c* axes forming larger hydrogen bond rings. ..... 35

**Figure 26**: (a) Compound **8** forms a hydrogen bond with amide donor and carbonyl acceptor. The N-H···N(pyridyl) is a short contact interaction (2.416 Å). (b) The *meta* positioned amino group always faces the same direction for each molecule. ..... 36

**Figure 27**: (a) Compound **9** forms a hydrogen bond between the amino donor and pyridyl acceptor; however a short contact interaction is observed between the amide donor and carbonyl acceptor (2.485 Å). (b) A head-to-tail motif is observed with amino hydrogen donor contributing to a N-H···π (2.830 A) interaction. ..... 36

**Figure 28**: (a) The *ortho* positioned amino group of compound **10** generates a variety of hydrogen bond rings. By utilising the amino, amide and hydrazone groups, a hydrogen bonded ring is formed using exclusively N-H···N bonds. (b) With the pyridyl nitrogen in the 3- position, a larger hydrogen ring is formed by utilising the second amino hydrogen donating to pyridyl nitrogen. π···π interactions are shown in blue (c) The hydrogen bond interactions are placed in context with the rings forming side by side. ..... 37

**Figure 29**: In compound **12** the amino donor placed in the *para* position with pyridyl nitrogen in the 3-position creates a 2D array of hydrogen bond chains (the amide donor and carbonyl acceptor utilised as the second hydrogen bond chain). A disorder of 50 % for the phenyl rings is observed. ..... 38

**Figure 30**: (a) Compound **13** forms a dimeric cluster with phenol donor and carbonyl acceptor. The pyridyl nitrogen forms an interaction with the amide hydrogen. (b) The linear dimeric clusters form zig-zag patterns proceeding along the *b*-axis. ..... 38

**Figure 31**: DSC trace of **1** showing the lack of a crystallization exotherm on cooling, forming a super-cooled melt. ..... 44

**Figure 32**: DSC trace of **4**. Recrystallization occurs only during the 2$^{nd}$ heating cycle, when a lower melting point for this form is observed. This thermal cycle is then repeated for the 3$^{rd}$ heating/cooling cycle. ..... 45

**Figure 33**: DSC trace for **8** where the initial melting is observed as a doublet. Upon cooling and sequential heating crystallization occurs and a new melting point is observed. ..... 46

**Figure 34**: DSC trace for **9** where an initial thermal event occurs before melting. During cooling minimal crystallization is observed and upon heating a lower doublet melting point is observed. ..... 47

**Figure 35**: DSC trace exemplifying decomposition of **11**. ..... 48

**Figure 36**: DSC trace for **12** where a thermal event occurs with the onset of 78°C thereafter which melting occurs. During cooling, crystallization is not observed. ..... 48

## LIST OF TABLES

**Table 2**: Crystallization solvents and melting points for the isoniazid derivatives. ..... 12
**Table 3**: Crystallographic data for IPH **I** – **VI**. ..... 17
**Table 4**: Thermochemical data for polymorphs of IPH **I** – **VI**..... 21
**Table 5**: Crystallographic data for compounds **1** – **6**. ..... 28
**Table 6**: Crystallographic data for compounds **7** – **12**. ..... 30
**Table 7**: Hydrogen bond parameters for compounds **1** – **6**. ..... 39
**Table 8**: Hydrogen bond parameters for compounds **7** – **13**. ..... 40
**Table 9**: Selected torsional angles for compounds **1** – **13** (**11** excluded). ..... 42

**TABLE OF CONTENTS**


DECLARATION ..... i

ABSTRACT ..... ii

ACKNOWLEDGEMENTS ..... iii

LIST OF ABBREVIATIONS ..... iv

LIST OF FIGURES ..... v

LIST OF TABLES ..... viii

CHAPTER 1INTRODUCTION ..... 1

1.1 Background to isonicotinic acid hydrazide (isoniazid) ..... 1

1.2 Solid-state crystalline manipulation ..... 2

1.2.1 Crystal engineering ..... 2

1.2.2 Supramolecular synthesis ..... 3

1.3 Intermolecular interactions ..... 3

1.4 Polymorphism ..... 5

1.4.1 Types of polymorphism ..... 6

1.4.2 Characterisation of polymorphs ..... 7

1.5 The effect of solvent on the crystallization process ..... 8

1.6 Hypotheses and aims ..... 8

CHAPTER 2 MATERIALS AND METHODS ..... 10

2.1 Synthesis and crystallization ..... 10

2.1.1 Synthesis of isonicotinic acid-(1-phenylphenylethylidene) hydrazide (IPH) ..... 10

2.1.2 Preparation of diffraction quality crystals of IPH ..... 10

2.1.3 Synthesis and crystallization preparations of derivatives **1** – **13** ..... 11

2.2 Instrumentation ..... 12

2.2.1 Crystal data and X-ray structural analysis ..... 12

2.2.2 Powder X-ray diffraction ..... 13

2.2.3 Differential scanning calorimetry (DSC) ..... 13

2.2.4 Hot-stage microscopy (HSM) ..... 13

2.2.5 Fourier-transform infrared (FT-IR) and Raman spectroscopy ..... 13

CHAPTER 3 POLYMORPHISM STUDIES OF ISONICOTINIC ACID-(1-PHENYLETHYLIDENE) HYDRAZIDE ..... 14
3.1 Introduction ..... 14
3.2 Crystal structure description of IPH **I** – **VI** ..... 15
3.2.1 Crystal structure of IPH **I** ..... 15
3.2.2 Crystal structure of IPH **II** ..... 15
3.2.3 Crystal structures of IPH **III** - **VI** ..... 16
3.3 Phase relationships ..... 18
3.3.1 Hot-stage microscopy of IPH ..... 18
3.3.2 Differential scanning calorimetry analysis and thermodynamic data ..... 21
CHAPTER 4 SUPRAMOLECULAR AGGREGATION STUDIES OF ISONIAZID DERIVATIVES ..... 24
4.1 Introduction ..... 24
4.2 Structural determinations ..... 25
4.2.1 Previous determinations ..... 31
4.2.2 Structural aggregations of derivatised isoniazid with phenol donor ..... 31
4.2.3 Structural aggregations of derivatised isoniazid with amino donor ..... 35
4.2.4 Structural description of pyridyl isomer at the 2- position ..... 38
4.3 Comparisons of changing substituted positions ..... 40
CHAPTER 5 THERMAL ACTIVITY STUDIES FOR ISONIAZID DERIVATIVES ..... 43
5.1 Introduction ..... 43
5.2 Thermal behaviour of IPH ..... 43
5.3 Thermal events of interest for compounds **1** – **13** ..... 43
5.3.1 Thermal events of interest for phenol modified compounds ..... 44
5.3.2 Thermal events of interest for amino modified compounds ..... 45
CHAPTER 6 CONCLUDING REMARKS AND FUTURE WORK ..... 49
6.1 Concluding remarks ..... 49
6.2 Future work ..... 49
REFERENCES ..... 50

APPENDICES ..... 52
1.1 Supporting Information for polymorphism studies of IPH ..... 52
1.1.1 Representative DSC traces for IPH **I** – **III** ..... 52
1.1.2 Powder X-ray diffraction patterns for forms IPH **I** – **III** and **V** ..... 54
1.1.3 FT-IR and Raman spectra of IPH **I** – **III** and **V** ..... 56
1.2 Supporting thermal activity information for supramolecular aggregate studies of isoniazid derivatives ..... 58

# CHAPTER 1 INTRODUCTION

This chapter briefly introduces the medicinal discovery of isonicotinic acid hydrazide and important functional groups contained within isonicotinic acid hydrazide derivatives. The following section introduces the main aspects of this project: structural manipulation of the isonicotinic acid hydrazide derivatives by applying concepts including crystal engineering, polymorphism and molecular interactions. The final section will discuss hypotheses and aims of this project.

## 1.1 Background to isonicotinic acid hydrazide (isoniazid)

Isonicotinic acid hydrazide (isoniazid) (Figure 1) was first prepared by Meyer and Malley in 1912 from ethyl isonicotinate and hydrazine.[1] Only in 1945 were its biological properties discovered when it was shown that nicotinamide had anti-*Mycobacterium tuberculosis* (TB) properties. This sparked the search for other pyridine derivatives with activity against TB.[2] TB subsequently developed strong resistance against the isoniazid drug which led to the search for isoniazid derivatives to combat the drug resistance.[3] At the time of drug resistance, derivatised forms of isoniazid such as isonicotinic acid-(1-phenylethylidene) hydrazide (IPH) (prepared from isoniazid and acetophenone) (Figure 2) were solely developed to combat TB. However such derivatised isoniazid compounds (and geometric isomers shown in Figure 3) now contains the functional group hydrazone ($R_1R_2C{=}NNH_2$). This hydrazone belongs to a larger Schiff base family containing the azomethine -NHN=CH functional group, a broad range anti-microbial enhancing functional group.[4]

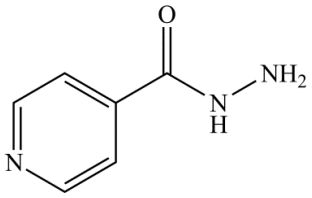


**Figure 1:** Parent structure of the nicotinamide based anti-TB drug isoniazid.

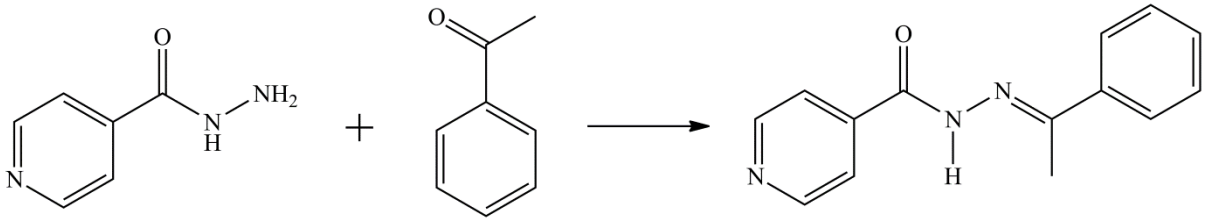


**Figure 2:** Isonicotinic acid-(1-phenylphenylethylidene) hydrazide (IPH) prepared from isoniazid and acetophenone.

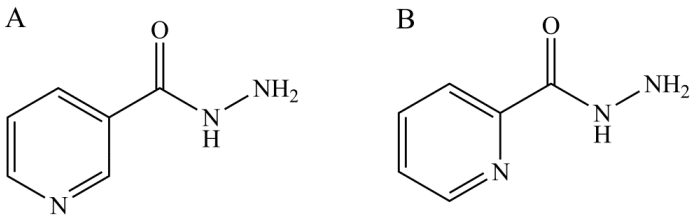


**Figure 3:** Pyridyl isomers of isoniazid: nicotinic acid hydrazide (A) and picolinic acid hydrazide (B).

In addition the hydrazone scaffold is considered a very important pharmacophore responsible for antimicrobial activity.[5] The International Union of Pure and Applied Chemistry (IUPAC) defines a pharmacophore as "an ensemble of steric and electronic features that is necessary to ensure the optimal supramolecular interactions with a specific biological target and to trigger (or block) its biological response".[6] The hydrazine group is considered a viable lead structure for the synthesis of drugs with broad spectrum and more efficacious antimicrobial activity.[5] The hydrazone functional group provides a backbone for numerous condensation reactions in benzo-fused *N*-heterocycles which allows for further development of critical new drugs.[7] Furthermore, established drugs containing the hydrazone functional group display anticonvulsant properties which can potentially open a new path for the treatment of epilepsy.[8] Therefore, *N*-isonicotinoyl arylketone hydrazones are an excellent group of compounds for solid state crystalline manipulation.

## 1.2 Solid-state crystalline manipulation

### 1.2.1 Crystal engineering

Crystal engineering is the attempt at pre-meditated control and design of crystal structures from organic, inorganic and hybrid species.[9] Crystal engineering is applied by understanding principles of intermolecular interactions that dominate in molecular solids in order to fine-tune their optical, magnetic or electronic properties, or simply to increase the knowledge base for the design of crystals.[10] The nascent field of crystal engineering can be extended to intermolecular assemblies such as the rational design of supramolecular polymers, protein ligand identification, drug delivery systems, as well as non-crystalline solids that have a degree of molecular organization.[11] Although the fundamental question in crystal engineering remains: 'What is the crystal structure of an organic compound, when solely provided with the molecular structure?' this question can be rephrased as 'During a crystallization event, do molecules recognise one another?'. Currently there is no general answer to this question but it can be dissected into smaller questions that may shed light on the situation as shown below:[12]

$$\text{One} \rightarrow \text{Few} \rightarrow \text{Many} \rightarrow \text{Crystal}$$

The above schematic implies that the crystallization process is initiated by a few molecules that assemble to form a cluster, which may then aggregate to form larger clusters.[12] After which a nucleation event occurs when these larger clusters interact with one another, which in turn leads to the creation of the first crystal.[12] When crystals are built up from a large number of molecules, the crystallization is not necessarily a smooth and continuous process in which the final structure of the crystal is established.[13]

The larger and smaller clusters possess local order which eventually leads to long-range order and periodicity associated with the crystalline state. However, the when and how of the crystallization process is complicated, and details of the timing largely remain unknown.[14] A small cluster may not exemplify a good model for a larger aggregate, as the process leading up to nucleation may contain discontinuities in the process of building up of clusters into nucleation and growth of a crystal.[15] Ultimately it becomes a difficult task to observe and understand the molecule-to-crystal progression.[16] Despite the difficulties faced in crystal engineering, the field can be broken down into three stages to provide a framework for de-convoluting the crystallisation process. The three stages of study are: (i) the study of intermolecular interactions; (ii) a strategy for crystal construction in the context of the packing modes and these intermolecular interactions; and (iii) the study of crystal properties.[17] These stages concurrently form the basis for supramolecular synthesis which is used in controlling crystal formation outcomes.

### 1.2.2 Supramolecular synthesis

The central dogma of supramolecular chemistry states that, just as atoms are built up and connected with covalent bonds to form a molecule, a supramolecule is built up with molecules, and intermolecular interactions are used as connectors between these molecules.[18] In other words crystal engineering can be considered as a form of solid state supramolecular synthesis since it is the design and construction of a molecular crystal.[19] Furthermore, crystallization is likened to supramolecular reaction (involving supramolecular synthons) where the crystal nucleus can be compared to a conventional transition state.[20] The required supramolecular synthons are defined as structural units that show the fundamental features of a crystal structure as well as encapsulate molecular recognition in crystals.[21] These synthons consist of molecular fragments (functional groups) and contain a variety of supramolecular associations (intermolecular interactions) (see Section 1.3) between them that direct the assembly. Predominantly the directional specificity of the hydrogen bonds is utilised.[22] Self-assembly of supramolecular arrays occurs when crystallization takes places and these supramolecular arrays will pack according to the most thermodynamically stable packing arrangement at a given temperature.[23] However, the kinetic product can potentially crystallise in a pseudo-stable state first, and may not necessarily be the most thermodynamically stable form.[23]

## 1.3 Intermolecular interactions

Intermolecular interactions play a crucial role in the determination of the molecular arrangement in a crystal.[24] Specific molecular arrangements are stabilised by these interactions, which are then able to cause changes in torsion angles, resulting in different conformations.[25] The most stabilised molecular conformation is the most stable equilibrium conformation, but various molecular conformations can have similar energy. The most important interaction for isoniazid derivatives and derivatised structural isomers is the hydrogen bond. As stated in a recent review by Nangia, "The hydrogen bond is the most important of all directional intermolecular interactions",[25] as the hydrogen bond is operational in a large variety of molecular aggregations.[25] The hydrogen bond is the most cohesive directive force in organic molecules and is considered a very strong bond with the typical bonding values of about 4 – 15 kcal $mol^{-1}$ for standard hydrogen bonds such as O-H···O, N-H···O, or O-H···N.[25] Hydrogen bonding resembles the start of proton transfer reactions where the typical hydrogen bond D-H···A, D-H is the proton donor and A is the proton acceptor (commonly referred to as donor and acceptor).[26]

Other weaker non-covalent intermolecular interactions include C-H···O hydrogen bond, π···π, as well as X···X (X = halogen) and C-H···π interactions.[24] In a typical hydrogen bond only a single donor and acceptor interact (Figure 4a) however a donor can also simultaneously interact with two or three acceptors (Figure 4b, c). A trifurcated hydrogen bond is not a common occurrence as stringent conditions are required.

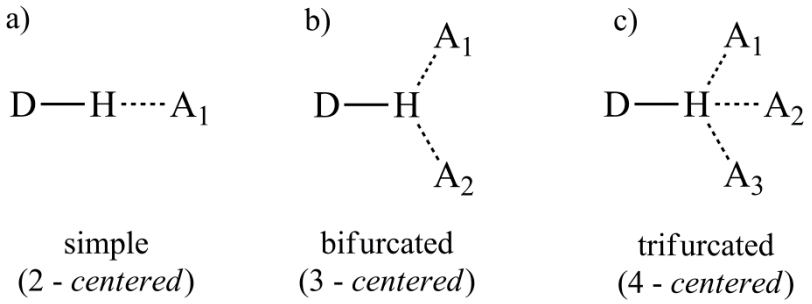


**Figure 4:** Hydrogen bond bridges. a) Typical hydrogen bond with a single donor and acceptor. b) Bifurcated hydrogen bond with two acceptors. c) Trifurcated hydrogen bond involving a single donor with three acceptors.

The schematic diagram of the hydrogen bond potential energy versus distance between donor and acceptor atoms in Figure 5 shows that a stabilising interaction (that is, with $E > 0$) is associated with a repulsive force if it is shorter than the equilibrium distance. Negative and positive bond energies of hydrogen bonding are described by the terms *stabilising* (i.e. bonding) and *destabilising* (i.e. anti-bonding), respectively.[26] Figure 5 shows the typical hydrogen bond of stabilising ($E < 0$) and destabilising ($E > 0$) interactions. The hydrogen bond potential is a stabilising interaction when the equilibrium distance is longer than the associated repulsive force.[26] If the *attraction* interaction has a distance of $d > d_0$ and the *repulsion* interaction has a distance of $d < d_0$ then this implies that the hydrogen bond length differing in length from $d_0$ will force a geometry to tend to lower energy.[26] Energies in the range of 0.5-10 kcal $mol^{-1}$ are similar to both *intra*molecular torsions and *inter*molecular non-bonded interactions.[27] Therefore there is a very strong possibility that polymorphism (see Section 1.4) in conformationally flexible systems can occur with relative ease.[27] Strong hydrogen bonding may be optimised when the geometry of the new polymorph causes multiple subtle deformations that lead to extreme deformation of one torsion angle.[28] This then causes the overall crystal packing to be influenced by molecular conformation and hydrogen bonding.[29] Depending on the molecular environments the packing arrangements may be rearranged into closely related or disparate molecular structures resulting in the occurrence of polymorphism.

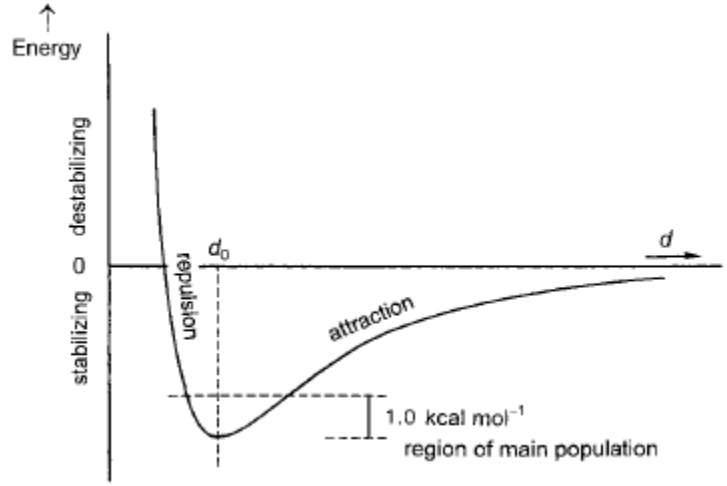


**Figure 5:** A schematic representation of the hydrogen bond potential energy versus distance between donor and acceptor atoms, *d*. Taken from reference 26.

## 1.4 Polymorphism

Since the middle of the 18th century it has been known that substances can crystallise into more than one form; however the topic of polymorphism of drug compounds has received extensive attention only recently by academia and industry, including the much publicised debate by patent lawyers.[30] It is well known that the adoption of a particular crystalline structure has profound influence over the solid-state properties of a compound. This was illustrated by early pioneering reports of Aguiar and colleagues at Parke–Davis where polymorphism was shown to influence the bioavailability and dissolution rates of chloramphenicol palmitate.[31, 32] The influence on solid-state properties is not limited to dissolution[33] and bioavailabilities[34] only, but has extensive influence on melting points,[35] mechanical processing,[36] shelf-life,[37] and meta-stabilities.[38] Polymorphism is now a well-established phenomenon in the development of drug compounds as it is of essential importance to understand and control the development of which polymorph is obtained, as the change in the solid-state properties of one form to another may have drastic consequences in the manufacturing processes in pharmaceutical production.[39] In addition, different polymorphs may influence every stage of drug compound development starting from pre-clinical stages to post marketing phase of the drug product, including patent protection.

Polymorphism is the manner in which a compound can rearrange itself in 3-D space in such a way as to have different packing arrangements or different conformational arrangements.[40-42]. Furthermore conformational polymorphism is where a flexible molecule can rearrange itself to produce more than one different conformation in the solid state.[42] However, most often both packing and conformational differences are observed among two or more different polymorphs.[43] The conformation of organic compounds is a subtle but an important property in polymorphism.[25] As the polymorphs can be interconverted by solid-to-solid phase transformations or via a solvent-mediated process; phase transformations can also be induced by heat or mechanical stress.[44]

When developing such drug compounds it is crucial to develop an understanding of the phase transformation relationships between various polymorphic forms. This enables drug developers to determine the most stable form and whether the desired form with the most beneficial solid-state properties will remain stable throughout the lifespan of the drug compound. The importance of polymorphs in a research and commercial setting is that they are able to exhibit many different physical properties, for example melting points and crystals habits. More importantly in the pharmaceutical industry, a change in compressibility and/or solubility of a potential drug candidate can greatly influence tableting procedures as well as bioavailability properties.[45] Polymorphism is mostly found in organic molecules such as alkanes, aromatic $\pi$-bonded systems, amino acids and carboxylic acids.[43] Contrary to popular belief, the crystal structures described by researchers are not necessarily supramolecular aggregates that have a minimum in the global free energy of the solid-state, as some polymorphic forms are actually metastable states, i.e. the kinetic product (Figure 6).[46] This kinetic product is described by Ostwald: "When leaving a metastable state, a given chemical system does not seek out the most stable state, rather the nearest metastable one that can be reached with minimum loss of free energy".[46]

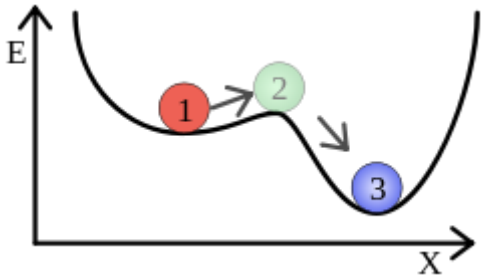


**Figure 6:** The metastable state (1) then moves to a transitional configuration (2) and finally to a stable state having minimum energy (3). Taken from reference 46.

Additionally, Gibbs free energy differences between polymorphs are usually minimal.[47] Particularly between room temperature and the melting point, one polymorph can be the thermodynamically stable form.[47] Whilst others may exist as meta-stable forms for an extended period of time, or may spontaneously convert into a more stable form. These conversions are called phase transitions in solids and have been classified as either first or second order transitions.[48] First-order transitions involve two phases in equilibrium at transition temperature, with a discontinuous change of any physical property.[48] The phase transition is believed to occur by nucleation of one phase, followed by its growth over another phase.[49] In second-order transitions there is no discontinuity in the volume or entropy at transition temperature, and are usually order-disorder transitions which are associated with a change in the degree of order in the solid.[50]

### 1.4.1 Types of polymorphism

The stability of polymorphic forms (in relation to temperature and pressure) are categorised into two relationships: monotropic or enantiotropic (Figure 7).[51] For a monotropic relationship, one polymorphic form is stable with a lower Gibbs free energy over the entire temperature and pressure range below its melting point, whilst the other polymorphic forms are metastable.[52]

The enantiotropic relationship occurs when one polymorphic form is stable over a certain temperature and pressure range, and may undergo a conversion into another polymorphic form that is stable over a different temperature range and pressure.[53] In the enantiotropic system, polymorph A has lower free energy ($G_A$) than polymorph B and is stable below the transition temperature ($T_t$).[53] As the temperature surpasses the transition point temperature, polymorph B has lower free energy ($G_B$) than that of polymorph A; thus polymorph B becomes more stable than polymorph A.[54] At the transition temperature where the free energy curves for polymorphs A and B intersect, a reversible phase transition is observed.[54] In contrast in the monotropic system, the free energy for polymorph A is less than that of the free energy of polymorph B throughout the entire temperature range below its melting point.[54] The free energy curves do not intersect and hence this system does not exhibit a reversible phase transition between polymorphs A and B below the melting points of both polymorphs.[55] However, at sufficient energy below the melting point, an irreversible phase transition may occur, where polymorph B melts followed by the crystallization of polymorph A as the most thermodynamically stable form.[55] On a final note, monotropic and enantiotropic relationships can be distinguished by determining the heats of fusion of the polymorphic forms.[55]

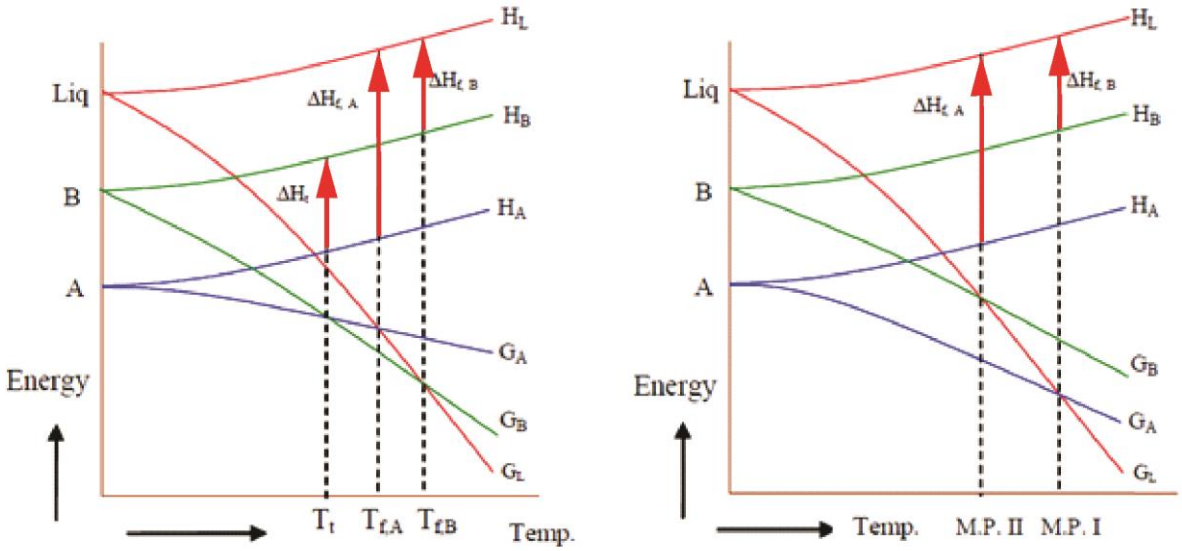


**Figure 7:** Free energy vs. temperature diagrams for the enantiotropic (left) and monotropic (right) systems for solid phases of polymorphic forms A and B. The enthalpies (heats of fusion) are represented with red arrows. Taken from reference **61**.

### 1.4.2 Characterisation of polymorphs

Analytical methods are used to characterise the different polymorphic forms, ranging from complete structural determination to melting point determination. Microscopic methods are used to study the morphology of crystals, as well as observing changes within crystal forms such as phase transitions with a change in temperature. Solid state NMR and vibrational spectroscopy are used to interpret molecular motion as well as the chemical environment. X-ray diffraction (single crystal and powder) provides unambiguous structural information where single crystal XRD provides atomic positions and complete structural information, and powder XRD provides solid state nature and purity of a bulk microcrystalline sample. Lastly, characterisation of the interrelationships of polymorphic forms can be quantified by thermal analysis. This includes differential scanning calorimetry (DSC), differential thermal analysis (DTA) and thermogravimetry.

## 1.5 The effect of solvent on the crystallization process

Crystallization of polymorphs from solvents may be under the control of kinetic or thermodynamic conditions.[56] In the case of thermodynamic conditions, there are three types of behavioral patterns are recognised that show dependence on nucleation and the specific polymorph's growth rate.[57] The three types of behavioral patterns are: i) at all concentrations the most stable polymorph form would crystallise preferentially; ii) the less stable polymorph form would crystallise out preferentially only at high concentrations; and iii) at intermediate concentrations the less stable polymorph form would crystallise out.[58] However the current (brute force) methodology for the determination of polymorphs for a given compound is to attempt to crystallise the compound from as many solvents as possible, without concern for the above situations, i.e. regardless of concentration.

The selectivity of a certain polymorph from solution is not a trivial process and the prescribed crystallization behavioral patterns do not exemplify a concrete law as the selected of one polymorph over another can result from many other factors other than crystallization that are not well understood.[59]

## 1.6 Hypotheses and aims

The hypotheses for this project are as follows:

- Preliminary studies performed by Dr Lemmerer at University of the Witwatersrand suggest that IPH has six polymorphs. Therefore a crystal structure for each of the six polymorphs can be obtained.
- The thermal phase relationship between each polymorph can be elucidated and quantified.
- The polymorphic space will be altered when the highly polymorphic isoniazid derivative is modified with additional hydrogen bond donors and acceptors.

The aims of this project are as follows:

- To synthesize isoniazid derivatives as well as nicotinic acid hydrazide and picolinic acid hydrazide derivatives, as shown in Table 1.
- To isolate IPH polymorphs from various crystallization techniques, followed by characterisation of these derivatives by physical techniques such as hot-stage microscopy (HSM), differential scanning calorimetry (DSC), single crystal and powder X-ray diffraction (SCXRD and PXRD) and infrared spectroscopy (IR).
- To obtain SCXRD quality crystals of isoniazid derivatives and its pyridyl isomers for crystal structure determination.
- To analyse the similarities and differences in intermolecular interactions and supramolecular clusters of the selected derivatives.
- To observe thermal behavior in an attempt to survey the polymorphic space for each derivative.

By applying the fundamental concepts of crystal engineering and supramolecular synthesis, it is envisaged that a diverse range of crystal structures can be obtained for the systems of interest. Ultimately, this study intends on contributing to current knowledge on these isoniazid derivatives, polymorphism, supramolecular aggregation and solid-state interactions.

**Table 1**: Detail of change in position of pyridyl nitrogen and different substituted acetophenones used in preparation of derivatives.

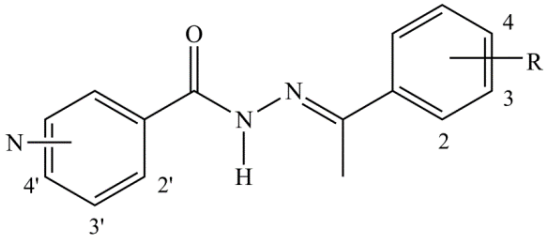


| | Pyridyl nitrogen | | |
|---|---|---|---|
| | 4'- position | 3'- position | 2'- position |
| Modification at position R | 2-OH | 2-OH | 4-OH |
| | 3-OH | 3-OH | |
| | 4-OH | 4-OH | |
| | 2-$NH_2$ | 2-$NH_2$ | |
| | 3-$NH_2$ | 3-$NH_2$ | |
| | 4-$NH_2$ | 4-$NH_2$ | |

# CHAPTER 2 MATERIALS AND METHODS

This chapter will describe the synthesis and crystallization protocols, crystal structure solution and physical characterisation procedures of this project.

## 2.1 Synthesis and crystallization

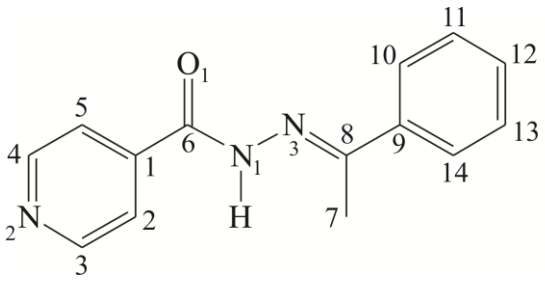


IPH **I**
IPH **II**
IPH **III**
IPH **IV**
IPH **V**
IPH **VI**

**Scheme 1:** Atomic labelling scheme of isonicotinic acid-(1-phenylphenylethylidene) hydrazide (IPH). The Roman numerals **I** – **VI** refer to the six expected polymorphs of IPH.

### 2.1.1 Synthesis of isonicotinic acid-(1-phenylphenylethylidene) hydrazide (IPH)

IPH was prepared in a yield of 95% by a Schiff Base reaction. Isoniazid (1.006 g, 7.335 mmol) (obtained from Sigma-Aldrich) and acetophenone (1.002 g, 8.343 mmol) were combined in a 100 ml round bottom flask, and dissolved in absolute ethanol (75 ml). To this mixture a catalytic amount of glacial acetic acid was added, and the solution was heated at reflux for 18 hours. A white solid precipitated from the reaction mixture which was filtered and washed with cold ethanol (3 × 25 ml). Characterisation of the product was determined by $^{1}H$ and $^{13}C$ NMR, IR and DSC (mp. 171.9°C) (see Appendices). Recrystallization was performed from using slow evaporation at ambient conditions with absolute ethanol as a solvent, yielding IPH **V**.

### 2.1.2 Preparation of diffraction quality crystals of IPH

For unequivocal proof of the existence of the IPH polymorphs, the crystal structures of each polymorph were essential. The first two diffraction quality crystals obtained were for IPH **II** and **V**. These crystals were recovered from slow cooling solution experiments using solvents acetonitrile and ethanol respectively. IPH **III** crystals were recovered from rapid evaporation of a water/ethanol solution. It should be noted that these slow cooling solution experiments exclusively produced the respective polymorphs; however the rapid evaporation experiments produced a mixture of IPH **III** and **V**. Hence diffraction quality crystals of IPH **III** were separated out under the polarizing microscope. After exhaustive solution experiments, sublimation experiments were performed using a Kofler hot bench, from which colourless needle-like IPH **I** crystals were recovered for the first time. Following this, IPH **IV** and **VI** were never isolated or seen until HSM experiments were performed. After numerous attempts, IPH **VI** was recrystallised from melt on the hot-stage and IPH **IV** was grown on the hot-stage from melt by using a very slow cooling rate methodology. This was done to provide ample time to allow sufficient crystal growth for X-ray analysis, despite which the crystals were still incredibly small (maximum size: 0.56 x 0.046 x 0.040 mm) and obtained in very limited amounts.

### 2.1.3 Synthesis and crystallization preparations of derivatives 1 – 13

Isoniazid (0.100 g, 0.729 mmol) and its pyridyl isomers were respectively mixed with the appropriate substituted acetophenone in an equimolar ratio, and dissolved in absolute ethanol (15 ml); these mixtures were then stirred at room temperature for 18 hours. The crude residue was filtered, and then washed with cold ethanol. Crystallization was achieved by slow evaporation of various solvents (see Table 2). Multiple crystallization experiments for **11** were not successful and suitable crystals for structure determination were never obtained. The melting points for each compound determined from DSC experiments are presented in Table 2.

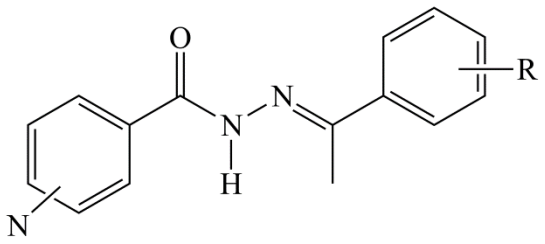


**1** - **6** (pyridyl N = 3-, 4-; R = 2-OH, 3-OH, 4-OH)

**1**: 1-(2-hydroxyphenyl)ethanone isonicotinoyl-hydrazone
**2**: 1-(3-hydroxyphenyl)ethanone isonicotinoyl-hydrazone
**3**: 1-(4-hydroxyphenyl)ethanone isonicotinoyl-hydrazone
**4**: 1-(2-hydroxyphenyl)ethanone nicotinoyl-hydrazone
**5**: 1-(3-hydroxyphenyl)ethanone nicotinoyl-hydrazone
**6**: 1-(4-hydroxyphenyl)ethanone nicotinoyl-hydrazone

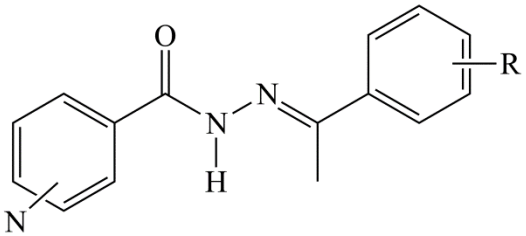


**7** - **12** (pyridyl N = 3-, 4-; R = 2-$NH_2$, 3-$NH_2$, 4-$NH_2$)

**7**: 1-(2-aminophenyl)ethanone isonicotinoyl-hydrazone
**8**: 1-(3-aminophenyl)ethanone isonicotinoyl-hydrazone
**9**: 1-(4-aminophenyl)ethanone isonicotinoyl-hydrazone
**10**: 1-(2-aminophenyl)ethanone nicotinoyl-hydrazone
**11**: 1-(3-aminophenyl)ethanone nicotinoyl-hydrazone
**12**: 1-(4-aminophenyl)ethanone nicotinoyl-hydrazone

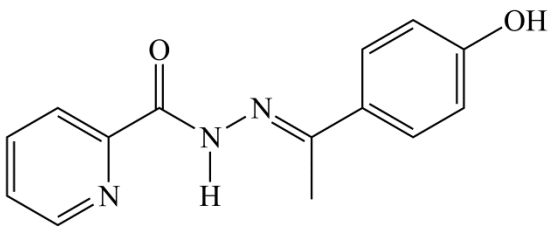


**13** (pyridyl N = 2-; R = 4-OH)

**13**: 1-(4-hydroxyphenyl)ethanone picolinoyl-hydrazone

**Scheme 2:** Compounds **1** – **13** were chosen to study the effects of donor modification and placement of pyridyl nitrogen on the supramolecular aggregates.

**Table 2**: Crystallization solvents and melting points for the isoniazid derivatives.

| Compound | Modification | Crystallization solvent | Melting point (°C) |
|---|---|---|---|
| **1** | 2-OH | ethanol | 165.5 |
| **2** | 3-OH | ethanol | 157.0 |
| **3** | 4-OH | ethanol | 289.0 |
| **4** | 2-OH | methanol | 162.3 |
| **5** | 3-OH | ethanol | 184.9 |
| **6** | 4-OH | ethanol | 261.0 |
| **7** | 2-$NH_2$ | ethanol | 141.0 |
| **8** | 3-$NH_2$ | ethanol | 144.7 |
| **9** | 4-$NH_2$ | 1-propanol | 223.6 |
| **10** | 2-$NH_2$ | methanol | 162.4 |
| **11** | 3-$NH_2$ | N/A | 152.2 |
| **12** | 4-$NH_2$ | methanol | 198.9 |
| **13** | 2-OH | methanol | 261.7 |

## 2.2 Instrumentation

### 2.2.1 Crystal data and X-ray structural analysis

The Bruker D8 VENTURE PHOTON CMOS area detector diffractometer, equipped with a graphite monochromated Mo $K\alpha_1$ radiation (50 kV, 30 mA), was used to collect all the intensity data. Crystal structures were collected at 173 K to achieve satisfactory thermal ellipsoids. The program *SAINT+*, vers. 6.02[60] was used to integrate the data and the program *SADABS* was used to make empirical absorption corrections. Space group assignments were made using *XPREP*[60] on all compounds. In all cases, the structures were solved in the *WinGX* Suite of programs[61] by direct methods using *SHELXS-97*[61] and refined using full-matrix least-squares/difference Fourier techniques on $F^2$ using *SHELXL-97*.[61] All non-hydrogen atoms were refined anisotropically. Thereafter, all hydrogen atoms attached to N atoms were located in the difference Fourier map and their coordinates refined freely with isotropic parameters 1.5 times those of the 'heavy' atoms to which they are attached. All C-H hydrogen atoms were placed at idealised positions and refined as riding atoms with isotropic parameters 1.2 times those of the 'heavy' atoms to which they are attached. Diagrams and publication material were generated using *ORTEP-3*,[62] *PLATON*[63] and *DIAMOND*.[64]

### 2.2.2 Powder X-ray diffraction

Powder X-ray diffraction data for IPH **I**, **II**, **III** and **V** were collected at 293 K on a Bruker D2 Phaser diffractometer which employs a sealed tube Co X-ray source ($\lambda$ = 1.5406 Å), operating at 30 kV and 10 mA, and LynxEye PSD detector in Bragg-Brentano geometry. Powder X-ray diffraction confirmed that the single crystal structures obtained from solution and sublimation experiments were representative of the bulk material (See Appendix).

### 2.2.3 Differential scanning calorimetry (DSC)

Differential scanning calorimetry data (Table 1) were collected using a METTLER TOLEDO with aluminium pans under air. STAR SW 9.20 was used for instrument control and data analysis. Exothermic events were shown as peaks. Various heating and cooling protocols were performed as quantitative analysis of the polymorphs. The temperature and energy calibrations were performed using pure indium (purity 99.99%, m.p 156.6°C, heat of fusion 28.45 J $g^{-1}$).

### 2.2.4 Hot-stage microscopy (HSM)

Hot stage microscopy experiments were performed using an Olympus SZ61 with stereo polarised light, and equipped with a Kofler hot stage. Various heating and cooling procedures for temperature induced crystal growth, melt and phase transitions were applied.

### 2.2.5 Fourier-transform infrared (FT-IR) and Raman spectroscopy

Infrared spectra for comparison of each form were collected for IPH **I** – **III** and **V** (see Appendices for spectra) using a Bruker Vertex 70 equipped with an ATR (MVP-Pro) sample handler. The experiment measured from 3500 $cm^{-1}$ to 400 $cm^{-1}$ and major peaks were assigned using OPUS 6.5. Infrared spectra of IPH **IV** and **VI** were not collected as sufficient quantities for IR experiments were never isolated. Complementary Raman spectra were collected for IPH **I** – **III** and **V** (see Supporting Information for spectra) using a Bruker MultiRAM FT-Raman Spectrometer fitted with an Nd-YAG laser and a Germanium diode detector. The experiment measured from 4000 $cm^{-1}$ to 400 $cm^{-1}$. Raman experiments were only performed on the forms with sufficient quantities and hence there are no spectra available for IPH **IV** and **VI**.

# CHAPTER 3 POLYMORPHISM STUDIES OF ISONICOTINIC ACID-(1-PHENYLETHYLIDENE) HYDRAZIDE

This chapter describes the in-depth study taken of IPH. The study begins with crystal structure description for each polymorph, and is then followed by delineating the phase relationships between each polymorph of IPH.

## 3.1 Introduction

To date, only one crystal structure of isonicotinic acid-(1-phenylphenylethylidene) hydrazide has been reported in the literature.[65] Five additional forms have been isolated in this study (all stable at room temperature), and their crystal structures have been determined. The six forms have been labelled as IPH **I** – **VI**, in a sequence of highest to lowest melting points. The previously known form is now known as IPH **V**. It should be noted that the isolation and subsequent determination of six different crystal structures for an organic compound is rare. For single component molecular compounds, 5-methyl-2-[(4-methyl-2-nitrophenyl)amino]-3-thiophenecarbonitrile (the famous ROY) is a well-known highly polymorphic compound (seven crystal structures),[66] and was recently superseded by flufenamic acid for the record of eight solved crystal structures.[67] Another significant polymorphic system is that of triacetone-triperoxide (TATP), for which six crystal structures have been determined to date.[68] In addition to solving the six crystal structures for IPH, the phase transformations and thermal relationships for IPH **I** – **VI** have been delineated, including the determination of thermodynamic parameters (enthalpies and temperatures of fusion and phase transitions). The use of HSM has been a critical tool in the study of these polymorphs.

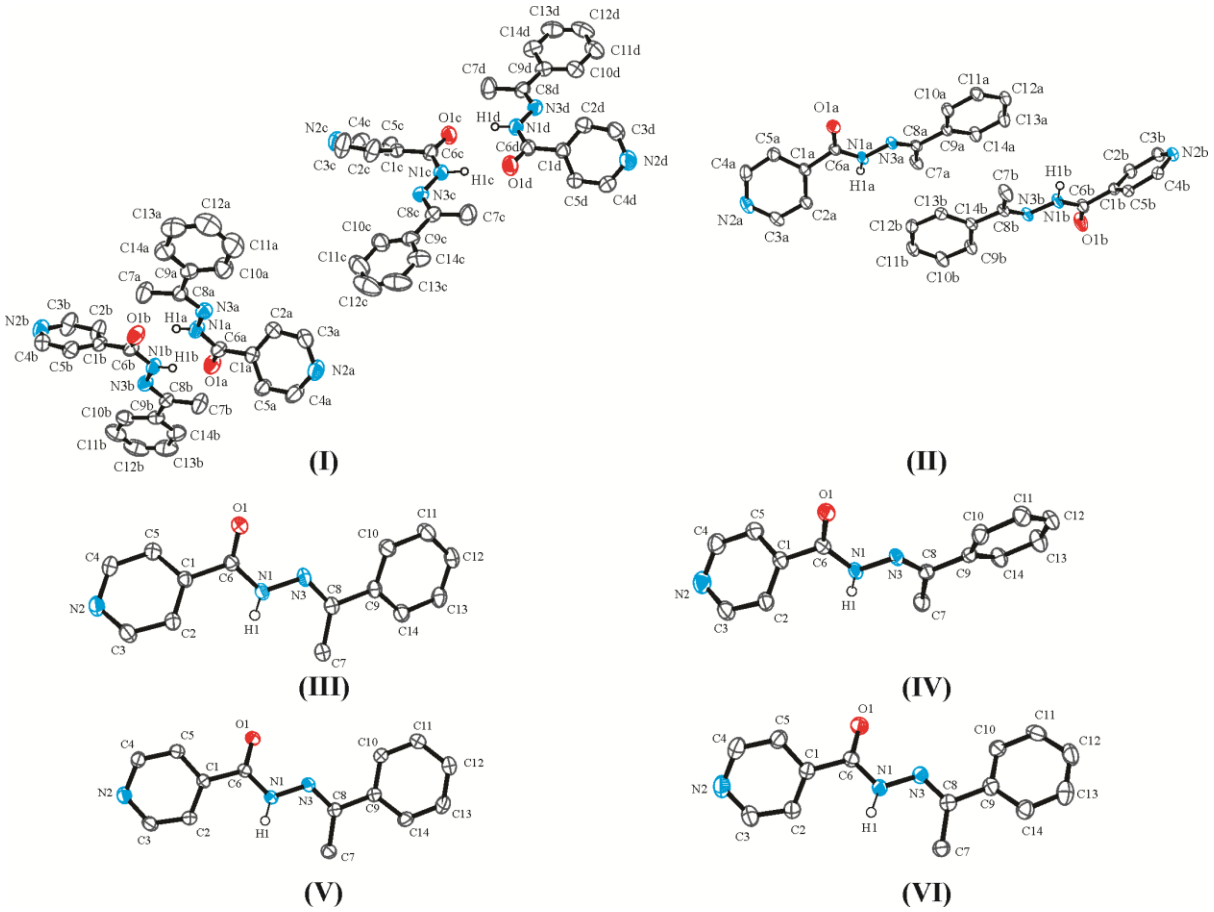


**Figure 8:** The asymmetric units of IPH **I** – **VI**. The displacement ellipsoids are drawn at 50% probability level. H on C atoms are omitted for clarity.

## 3.2 Crystal structure description of IPH I – VI

### 3.2.1 Crystal structure of IPH I

The asymmetric unit of IPH **I** consists of two pairs of symmetry independent molecules (A & B and C & D respectively) (Figure 8). These pairs hydrogen bond to one another using N-H···O bonds to form discrete dimers with graph set notation [69, 70] $R_2^2(8)$. Notable is the conformation with the amide H now *syn* to the carbonyl group (Figure 9). This is not seen in the other polymorphs.

### 3.2.2 Crystal structure of IPH II

The asymmetric unit of IPH **II** contains two symmetry independent molecules (Figure 8). In this crystal structure there are two rather distinct hydrogen bond patterns where molecule A will form a hydrogen bond pattern through the amide N1-H1···O1 hydrogen bonds which creates an infinite chain along the *c*-axis of the unit cell, graph set *C*(4). Molecule B forms a dimer using the hydrazide hydrogen and pyridine nitrogen (N1-H1···N2). This cyclic dimer has graph set notation $R_2^2(14)$ (Figure 9). The two molecules themselves have no hydrogen bonding interactions between them. IPH **II** is the only polymorph in which the pyridine nitrogen is involved in hydrogen bonding.

### 3.2.3 Crystal structures of IPH III - VI

The unit cell of IPH **III** has the longest cell axis of all the polymorphs, yet the asymmetric unit consists of only one symmetry independent molecule, resulting in a *Z* of 8 (Table 3) as seen in IPH **I** and **II** above. The asymmetric units of IPH **IV** – **VI** all have one molecule in a general position, with *Z* of 4 (Figure 8). The hydrogen bonding pattern for all these forms is a *C*(4) chain as seen in molecule A in IPH **II** (Figure 10).

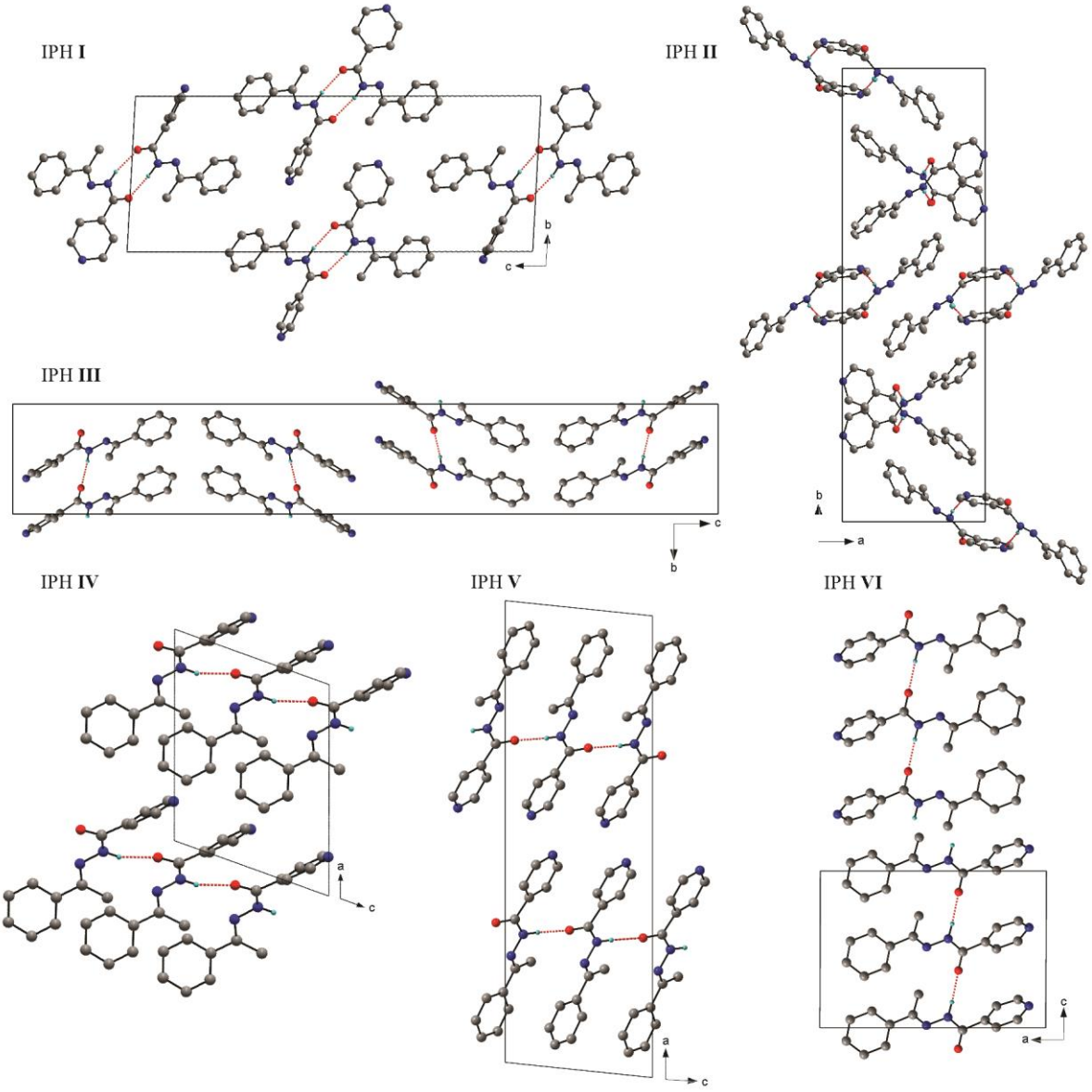


**Figure 9:** Packing arrangements of IPH **I** – **VI** viewed along their respective axes. IPH **I** demonstrates significant twisting of the pyridine ring relative to the carbonyl motif to facilitate dimerization hydrogen bonding. A common chain hydrogen bond motif is observed throughout the remaining polymorphs (with exception to IPH **II** co-forming a dimer by hydrogen bonding). Despite this commonality the unit cell parameters differ from polymorph to polymorph.

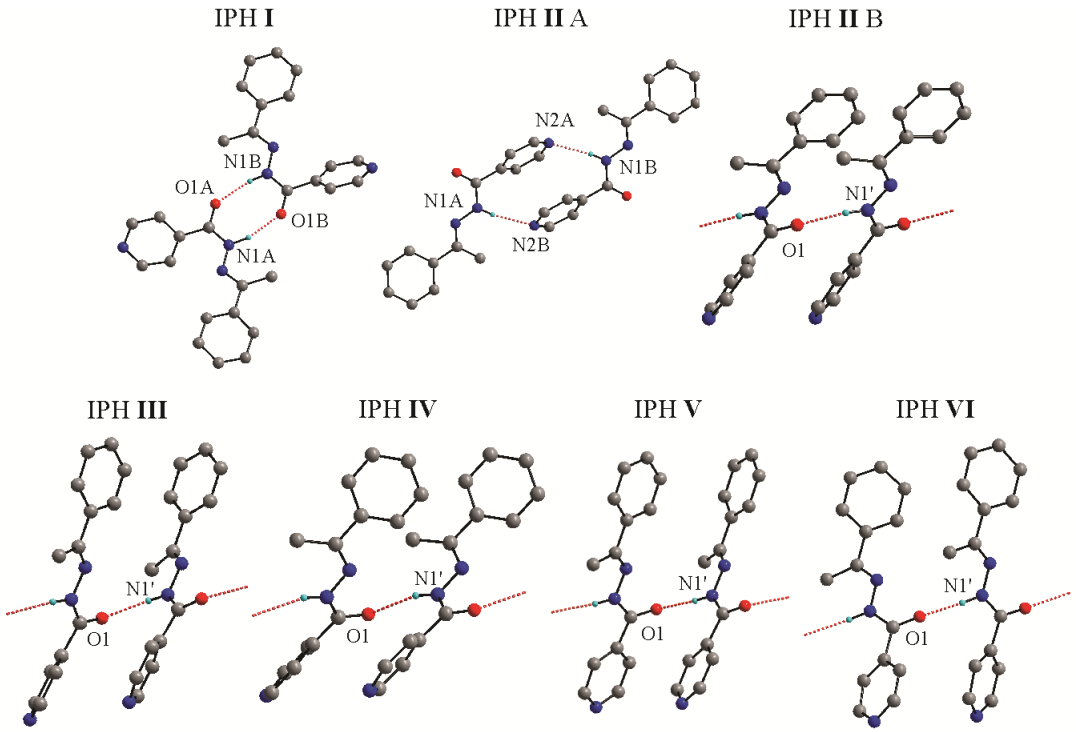


**Figure 10:** Hydrogen bond patterns for polymorphs IPH **I** – **VI**. These hydrogen bond patterns are used as a point of reference to juxtapose the conformational twisting of each polymorph.

**Table 3**: Crystallographic data for IPH **I** – **VI**.

| Compound | **I** | **II** | **III** | **IV** | **V** | **VI** |
|---|---|---|---|---|---|---|
| Formula | $C_{14}H_{13}N_3O_1$ | $C_{14}H_{13}N_3O_1$ | $C_{14}H_{13}N_3O_1$ | $C_{14}H_{13}N_3O_1$ | $C_{14}H_{13}N_3O_1$ | $C_{14}H_{13}N_3O_1$ |
| $M_r$ | 239.27 | 239.27 | 239.27 | 239.27 | 239.27 | 239.27 |
| Crystal size [$mm^{-3}$] | 0.40 x 0.061 x 0.020 | 0.55 x 0.28 x 0.10 | 0.42 x 0.11 x 0.050 | 0.56 x 0.046 x 0.040 | 0.45 x 0.20 x 0.060 | 0.42 x 0.37 x 0.040 |
| Crystal habit* | Needle | Prism | Needle | Needle | Plate | Block |
| T [K] | 173(2) | 173(2) | 173(2) | 173(2) | 173(2) | 100(2) |
| System | Triclinic | Monoclinic | Orthorhombic | Monoclinic | Monoclinic | Monoclinic |
| Space group | P-1 | $P2_1/c$ | Pbca | $P2_1/c$ | $P2_1/c$ | $P2_1/c$ |
| *a* [Å] | 9.7360(6) | 10.211(2) | 6.3540(4) | 10.621(2) | 25.899(1) | 13.488(2) |
| *b* [Å] | 9.8752(6) | 30.331(7) | 7.6624(6) | 14.442(2) | 5.5463(3) | 9.6611(1) |
| *c* [Å] | 26.154(2) | 8.2353(2) | 49.231(3) | 8.2589(2) | 8.3187(4) | 9.3604(1) |
| $\alpha$ [°] | 92.856(4) | 90 | 90 | 90 | 90 | 90 |
| $\beta$ [°] | 100.29(4) | 110.19(1) | 90 | 109.62(5) | 95.876(4) | 90.183(5) |
| $\gamma$ [°] | 91.291(4) | 90 | 90 | 90 | 90 | 90 |
| V [$Å^3$] | 2469.8 | 2393.9(9) | 2397.0(3) | 1193.3(3) | 1188.7(1) | 1219.7(3) |
| Z / Z' | 8 / 4 | 8 / 2 | 8 / 1 | 4 / 1 | 4 / 1 | 4 / 1 |
| $\rho$ [$g.cm^{-3}$] | 1.287 | 1.328 | 1.326 | 1.332 | 1.337 | 1.303 |
| $R_1$ / $wR_2$ | 0.0559/ 0.122 | 0.0400/ 0.113 | 0.0425/ 0.113 | 0.0532/ 0.107 | 0.605/ 0.148 | 0.0729/ 0.193 |

*All crystals obtained for each polymorph were colourless in appearance.

## 3.3 Phase relationships

### 3.3.1 Hot-stage microscopy of IPH

Four major phase transitions were observed and studied for IPH (Figure 11 – 13). Two phase transition cycles are presented and a video showing the phase transitions on thin film samples in action is available in the supplementary information. Beginning with IPH **V**, an endothermic transition of IPH **V** to **III** is followed by means of a large single crystal, recovered from bulk crystallization after the synthesis of the compound (Figure 11). The onset of this transition occurs at 129°C and is irreversible upon heating and cooling to room temperature. Additional phase transitions are observed in thin-film preparations.

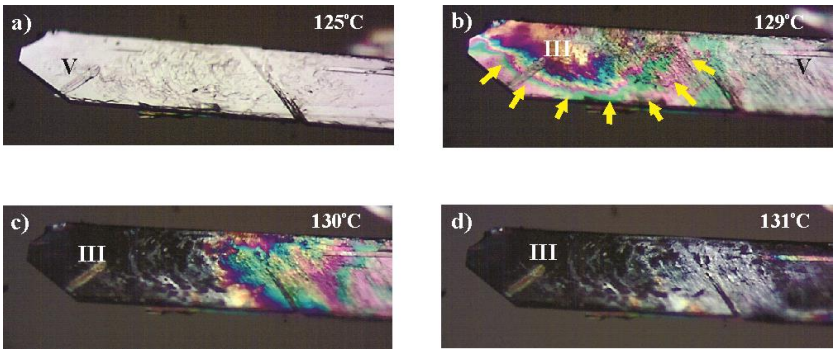


**Figure 11:** Plate-like crystal of IPH recovered from bulk recrystallization. Photograph a) shows IPH **V** before onset transition temperature (129°C), whilst b) shows the transition with the encroaching wave front (yellow arrows) in the crystal. c–d) shows the progress of the phase transition until the crystal has completely transformed into IPH **III**.

When a thin-film of IPH is taken from melt and allowed to recrystallise, four concomitant forms of IPH **I**, **III**, **IV** and **VI** are produced (Figure 12). The recrystallization process occurs at around 129°C with relative mass proportions of each form ranging from bulk coverage to only a few seed crystals within the thin film sample. Recommencing the heating cycle, after cooling to room temperature, an initial phase transition occurs with an average onset temperature of (145 - 148°C), where IPH **IV** and **VI** undergo a phase transition into IPH **III**. Additionally during this process, IPH **IV** and **VI** transform into IPH **I**; however over this lower temperature range, the transition rate for these metastable forms is slower than that into IPH **III**. Therefore after this phase transition is completed at 155°C, a large fraction of IPH **III** with a relatively minor fraction of IPH **I** are now the only forms present in the thin-film sample.

The second phase transition begins concurrently at 155°C with the end of the first phase transition, where IPH **III** reflects the transformation into IPH **I**. At *ca* 165°C the entire thin-film is converted into the high temperature form IPH **I** which then melts at 173°C. When this hot-stage cycle is repeated (bulk sample instead of thin-film) by fusing small amounts of IPH onto a glass slide coated with silicon oil, a different series of thermal events occurs (Figure 13). The advantage of such a preparation is that metastable islands are able to nucleate and grow and are not in contact with more stable form. After melting and subsequent cooling, IPH **IV** crystallises out as dendrites and needles without contact of the surrounding islands of IPH **III** and **VI** (Figure 13a – b). Therefore, it was possible to determine the homogeneous melting point of IPH **IV** at 145°C (Figure 3b) although islands of IPH **III** and **VI** are present in the close surrounding. Shortly thereafter at 150°C a phase transition begins in which IPH **VI** transforms into IPH **III** and is completed at 155°C.

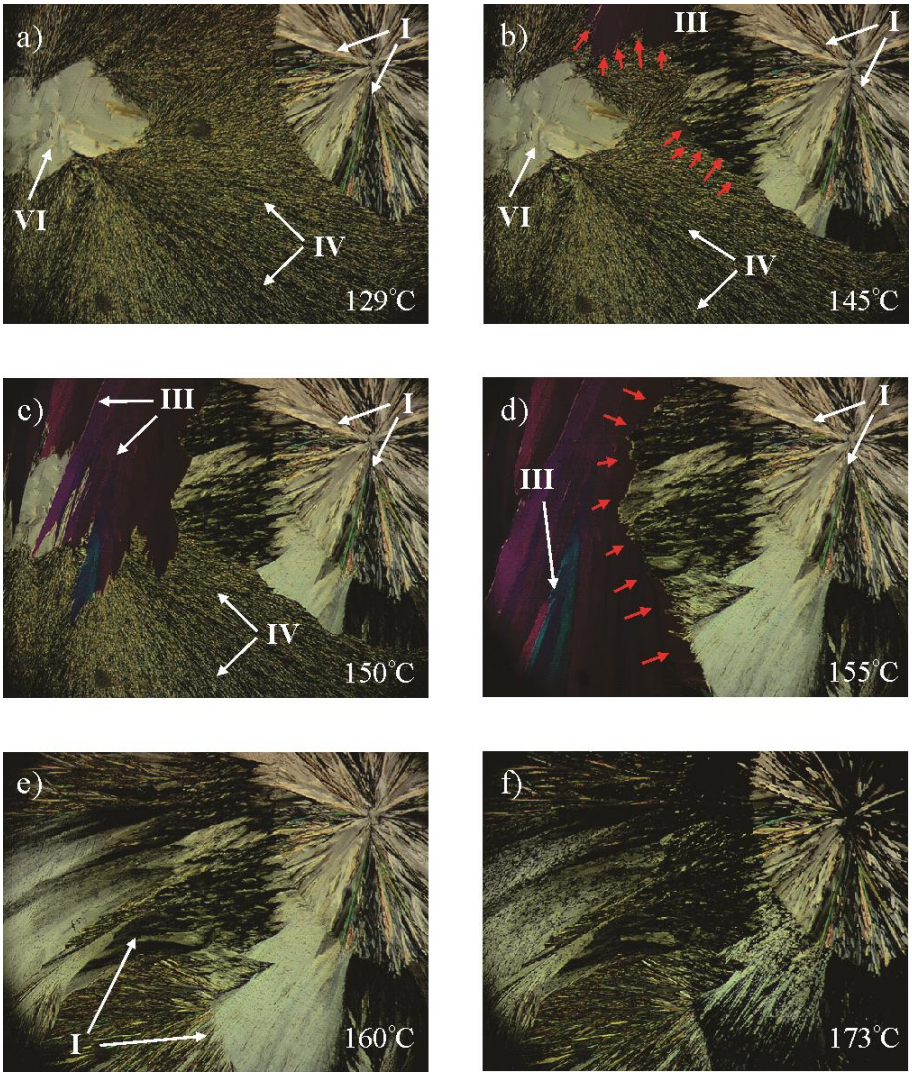


**Figure 12:** Thin-film photo micrographs of the phase transition cycle of IPH as observed on the polarised microscope. The cycle begins by recrystallization from melt, producing concomitant forms IPH **I**, **III**, **IV** and **VI**. Upon commencement of the heating cycle, the first phase transition (145°C) follows the encroaching wave front (red arrows) where IPH **IV** and **VI** transform into IPH **III**. This phase transition continues until IPH **IV** and **VI** are completely transformed into IPH **III** and **I**. The second phase transition (155°C) occurs with IPH **III** converting into IPH **I** until the sample is dominated by IPH **I**. Melting of IPH occurs with the onset of 173°C, and subsequent cooling allows for recrystallization and completion of the phase transition cycle.

Owing from the paucity of IPH **I** seeds, no further transitions occur and this series of thermal events ends with the melting of IPH **III** at 163°C. A third alternative route may be taken after melt when a sample of IPH is quenched cooled to 25°C forming an amorphous solid (Figure 14). Upon heating to 65°C the amorphous solid crystallises into IPH **I** (Figure 14b). The recrystallization of the super-cooled melt into IPH **I** is quantitatively verified in the DSC trace of Figure 15.

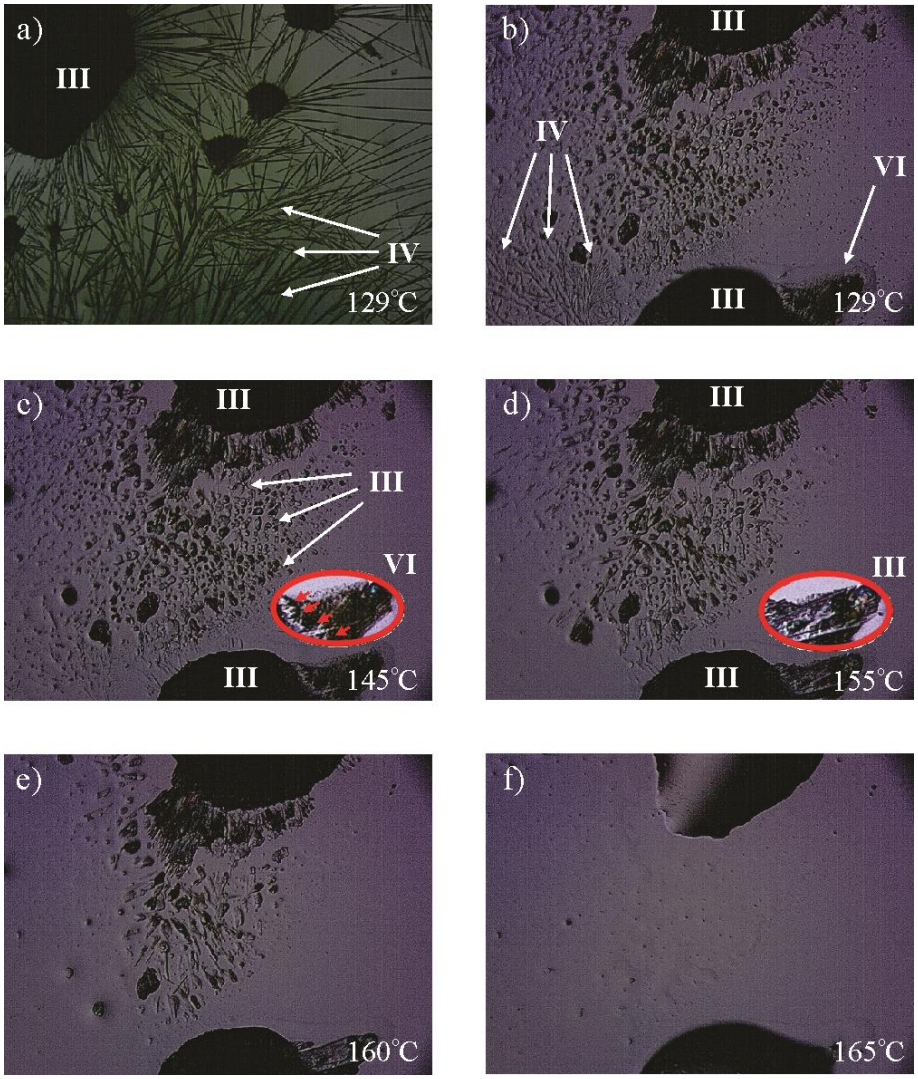


**Figure 13:** Recrystallised islands of IPH and subsequent slow heating. Photograph a) shows pronounced recrystallization of IPH **IV**; b) shows concomitant recrystallization of IPH **III**, **IV** and **VI**; c) shows the onset of melting of IPH **VI** at 145°C, while a phase transition of IPH **VI** to **III** marked by red arrows occurs; d) shows the completion of the phase transition with the onset of 155°C. Finally, melting of IPH **III** (onset of 165°C) is shown in e) and f).

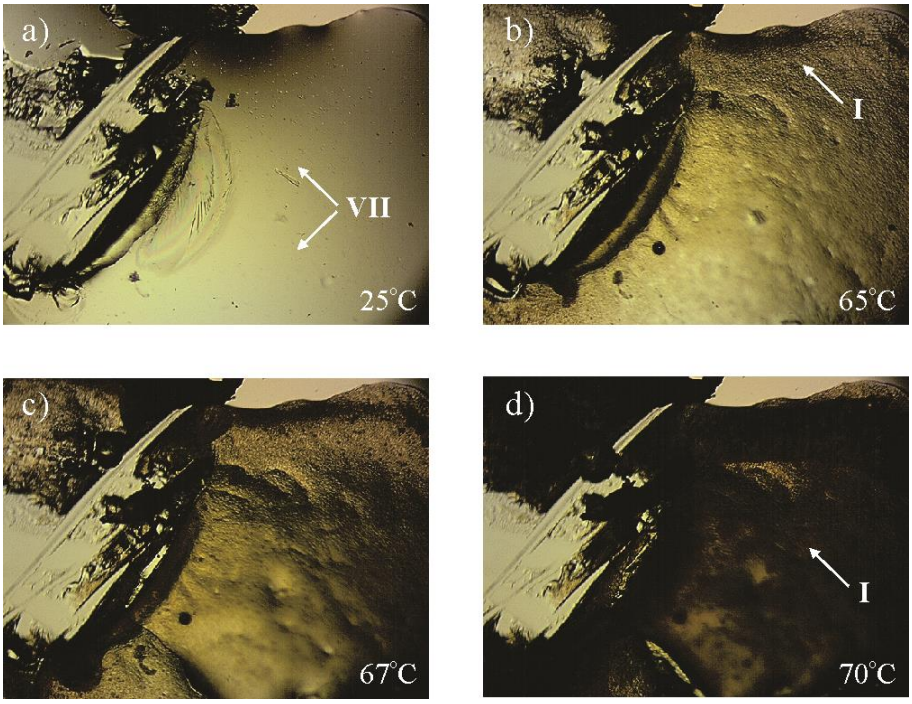


**Figure 14:** Super-cooled amorphous solid after quench cooling from melt. Photograph a) shows the amorphous solid with intentional breakage exemplifying rigidity; b) and c) show melting with the onset of 65°C of the amorphous solid with the presence of seed crystallites of IPH **I**; d) shows completed recrystallization of IPH **I**.

### 3.3.2 Differential scanning calorimetry analysis and thermodynamic data

The thermal behaviour observed on the hot-stage of all the forms of IPH was quantitatively verified and complimented using DSC experiments. In a large number of heating and cooling experiments, powdered IPH **V** was used as an initial starting point (for DSC traces beginning with other isolated IPH forms please see the appendices). Thermochemical data are calculated and summarised in Table 4.

**Table 4**: Thermochemical data for polymorphs of IPH **I** – **VI**.

| Property | IPH **I** | IPH **II** | Form IPH **III** | IPH **IV** | IPH **V** | IPH **VI** |
|---|---|---|---|---|---|---|
| $T_{fus}$ [°C] DSC | 171.9 ±0.2 | 164.7 ±0.8 | 161.1 | - | - | ~156 |
| HSM [°C] | 173 | 165 | 162 | 145 | - | 155-158 |
| $\Delta_{fus}H$ [kJ mol$^{-1}$] | 33.1 ±1.4 | - | - | - | - | - |
| transition to mod. | - | - | → **I** | → **III** | → **III** | → **III** |
| $\Delta_{trs}H$ [kJ mol$^{-1}$] | - | - | −3.1 ±0.2 | | | |
| $T_{cryst}$ [°C] | 128.9 | - | 128.9 | | - | ~130 |
| ρ [g cm$^{-3}$][a] | 1.287 | 1.328 | 1.326 | 1.332 | 1.337 | 1.303 |

[a] Calculated from crystal structure determinations at −100°C.

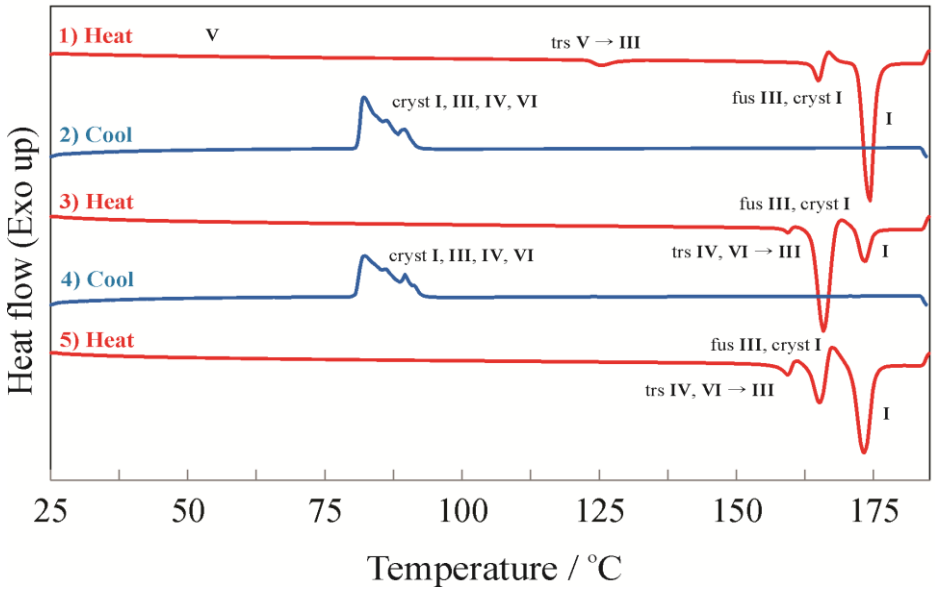


**Figure 15:** DSC traces of five successive heating /cooling runs beginning with IPH **V**. The initial trace shows the first phase transition (trs) from IPH **V** to **III** followed by a second phase transition of IPH **III** to **I**, and finally melting endotherm of IPH **I**. This is followed by the recrystallization of forms IPH **I**, **III**, **IV** and **VI** during the cooling runs. The second heating cycle shows phase transition of IPH **IV**, **VI** to **III** at 145°C and IPH **III** to **I** at 165°C respectively. The following heating/cooling cycles repeat the 2$^{nd}$ and 3$^{rd}$ heating and cooling cycles. The heating rate is 15 K/min.

As shown in Figure 11, the phase transitions can be followed along the DSC trace in the first heating cycle (Figure 15) where a weak endothermic peak with onset temperature of 123°C indicates the phase transition of IPH **V** into **III**. At 163°C the inhomogeneous melting process (melting of IPH **III** and simultaneous crystallization of IPH **I**) is observed as an *endo*/*exo* process. The final thermal event during the heating cycle is the melting of IPH **I** at 172°C. The following cooling cycle introduces IPH **IV** and **VI** by means of concomitant recrystallization reproducibly over the temperature range 80 – 95°C. The successive heating/cooling cycles repeat the thermal behaviour shown in 2) heating and 3) cooling cycles, however the relative mass percentage of each form during the concomitant recrystallization process is altered. This in turn affects the magnitude of the phase transition and melting peak endotherms in these subsequent heating/cooling cycles. As a result of the nature of IPH **VI**, no further thermochemical data were obtained as the melting and transition endotherms cannot be resolved and this form was only ever isolated during hot-stage experiments in insufficient quantities for DSC analysis.

Upon reheating the crystallised melt a weak endothermic event is visible around 157°C which is followed by the transformation of IPH **VI** to **III**, suggesting that the lower melting form IPH **IV** (145°C, see HSM experiments) underwent a solid-solid transformation to IPH **III** already at lower temperatures. The transformation of IPH **IV** into **III** is energetically very weak (as the representative peaks in the DSC traces are relatively small) and occurs over a broad temperature range. IPH **I** is the form with the highest melting point and lowest density. Therefore, we can assume that this form shows the highest entropy and a low thermodynamic stability (high free energy) at 0 K. From this, it can be inferred that IPH **I** is enantiotropically related to most, if not to all, of the other forms.

IPH **V** shows the highest density, and our data suggest that this polymorph is the thermodynamically stable form at room temperature. The observed endothermic transition of IPH **V** into IPH **III** is an indication of the enantiotropic relationship between these two forms (heat-of-transition rule[71]). Therefore there is a temperature range above room temperature where IPH **III** is more thermodynamically stable than IPH **I** and **V**. Furthermore, IPH **II** has the second highest melting point and its density is slightly higher than that of IPH **III**, suggesting that IPH **II** has greater stability with respect to IPH **III**. This suggests that there are three temperature regions containing the most thermodynamically stable form: IPH **V** at and below room temperature, IPH **II** above room temperature and below its melting point, and with IPH **I** right below its melting point. Consequently, IPH **III**, **IV** and **VI** are metastable in the entire temperature range. It should be noted that the IPH forms exhibit prolonged kinetic stability, which is indicated by the observation that IPH **I**, **II** and **III** did not transform to the room temperature stable form IPH **V** even after a storage period of one year.

When taking a different approach after quench cooling, the super-cooled amorphous solid thermal activity can be quantitatively verified. The amorphous solid resulting from crash cooling of the melt shows a broad recrystallization exotherm upon reheating at approximately 65°C with melting of form IPH **I** only (Figure 16). Upon heating to 65°C an initial broad exothermic peak is present and is attributed to the crystallization of IPH **I**.

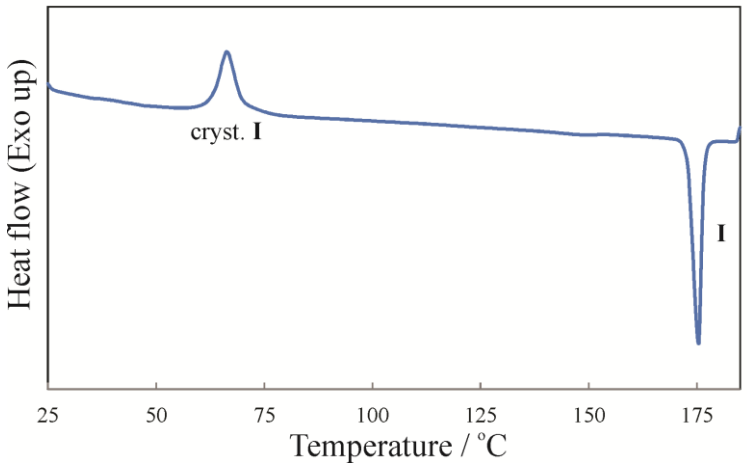


**Figure 16:** DSC trace of heating run for the super-cooled amorphous solid. At 65°C, a broad exothermic peak is observed, indicating a phase transition to IPH **I**. This is followed by eventual melting of IPH **I**.

In conclusion six crystal structures have been determined for IPH. Additionally the structural arrangements have been explored, allowing discernment between each polymorph. Each form is stabilised by N-H···O hydrogen bond, with IPH **II** utilising the N-H···N hydrogen bond in addition to the amide-carbonyl hydrogen bond. Thermal analysis was performed and three major temperature ranges have been identified. These temperature ranges include the phase relationships and melting habit of the six polymorphs. To finalise the thermal picture of this polymorphic system, isolation of practical quantities of IPH **IV** and **VI** are required.

# CHAPTER 4 SUPRAMOLECULAR AGGREGATION STUDIES OF ISONIAZID DERIVATIVES

This chapter details and compares the crystal structure arrangements and subsequent supramolecular aggregation patterns for the pyridine based isoniazid derivatives.

## 4.1 Introduction

In recent studies[4, 5] researchers have evaluated the antimicrobial activity of various analogues of *N*-isonicotinoyl arylaldehyde hydrazones. Therefore understanding the molecular structures may provide insight for researchers developing drugs of this type. Additional work on geometric isomers of *N*-isonicotinoyl arylaldehyde hydrazones have been used to study supramolecular structures arising from multiple hydrogen bonding nodes.[72] For this study the hydrogen bonding patterns and supramolecular aggregates arising when *N*-isonicotinoyl arylketones hydrazones are modified with R = OH or $NH_2$ at the *ortho*, *meta* and *para* positions of the phenyl ring, as shown in Scheme 2 will be followed. The molecule contains a number of hydrogen bonding functional groups arising from the pyridine ring and modified phenyl ring which are linked by a highly polar hydrazone group (Scheme 3). Possible interactions observed are O-H···N, N-H···N, O-H···O, N-H···O, N-H···π, π···π stacking and other weaker interactions such as C-H···N, C-H···O, C-H···N(pyridyl).

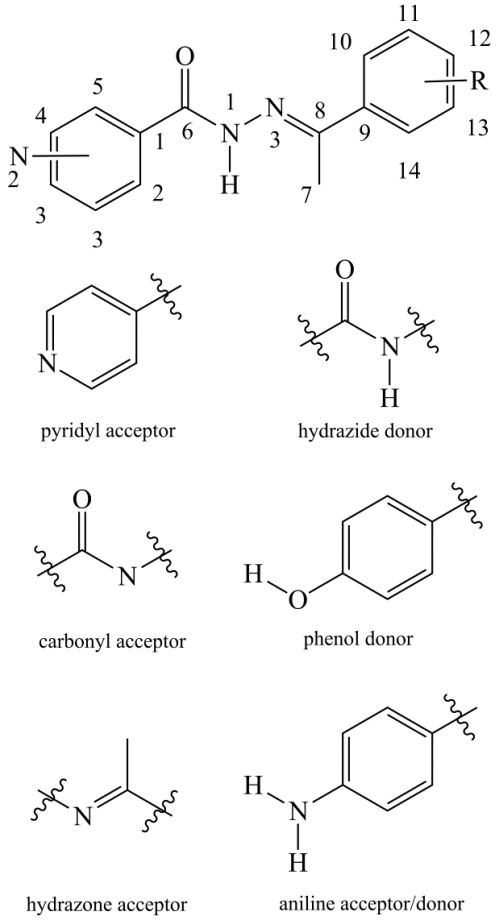


**Scheme 3**: Numbering scheme and functional groups present within the isoniazid derivatives involved in hydrogen bonding.

In an attempt to create further diversity amongst the aggregates, the skeletal backbone of the molecule was altered by shifting the pyridyl nitrogen to the 3- position from the 4- position. The intention behind these modifications is to observe the hydrogen bond patterns manifested during crystallization when the hydrogen bond nodes are shifted around to different regions of the molecule. A third pyridyl isomer was also investigated in which the pyridyl nitrogen was placed in the 2- position (Scheme 2) to determine whether this position for the pyridyl nitrogen could be useful for forming hydrogen bond nodes with neighbouring donors. Overall the compounds were found to generate one, two, and three dimensional aggregates with no distinctive predilection for a single direction-specific intermolecular interaction, as will be discussed below. Even minor alterations to the skeletal backbone by shifting the pyridyl nitrogen one position in the ring can give rise to disparate supramolecular aggregates. As a result there is paucity in the prediction of crystal structures for geometric isomers.

## 4.2 Structural determinations

The atomic numbering scheme for phenol modification of the pyridine based series **1** – **6** is shown in Figure 17 and amino modification series **7** – **12** in Figure 18 (**13** is included within Figure 17, however it is the only compound with the pyridyl nitrogen modified at the 2- position). Crystallographic data for the series **1** – **6** and **7** – **13** are shown in Tables 5 and 6 respectively. Hydrogen bonding interactions between each molecule are central to this study and therefore the donor and acceptor atoms are labelled consistently to make comparisons easier. Hydrogen bonding distances and angles for the series of compounds **1** – **6** and **7** – **13** are shown in Tables 7 and 8 respectively. The amide hydrogen is a robust donor as it may form hydrogen bonds either with the carbonyl or pyridyl acceptor of a neighbouring molecule. All compounds experience a degree of hydrogen bonding that varies in number from one hydrogen bond to five hydrogen bonds depending on the modification and position on the phenyl ring. The molecules form a variety of hydrogen bond patterns from discrete units to larger dimensional ones with many hydrogen bond rings. Selected torsional angles are present in Table 9. Each structure will be described briefly before overall trends and differences in structure generated by the modifications will be discussed.

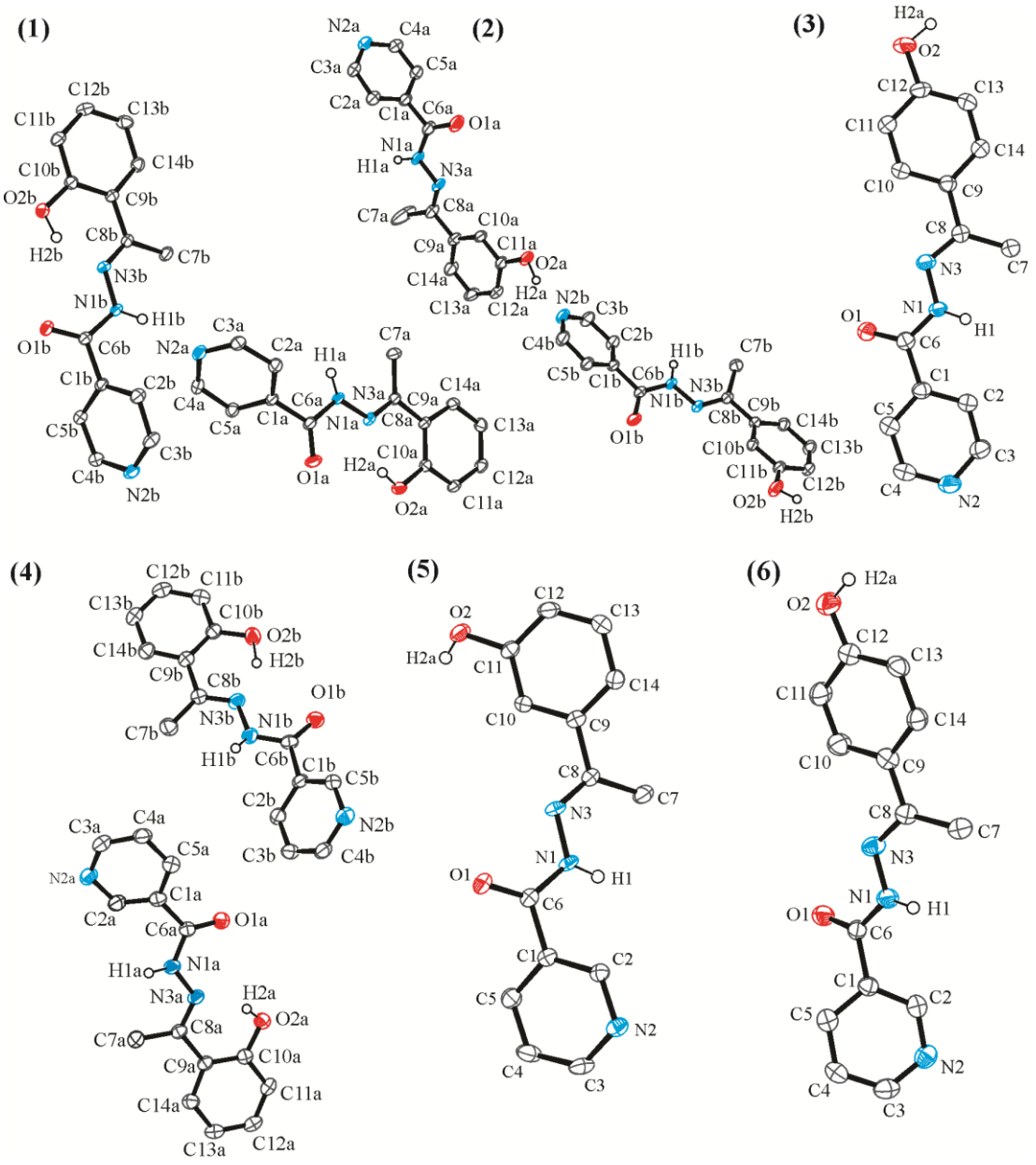


**Figure 17:** The asymmetric units **1** – **6**. The displacement ellipsoids are drawn at 50 % probability level; H on C atoms are excluded for clarity.

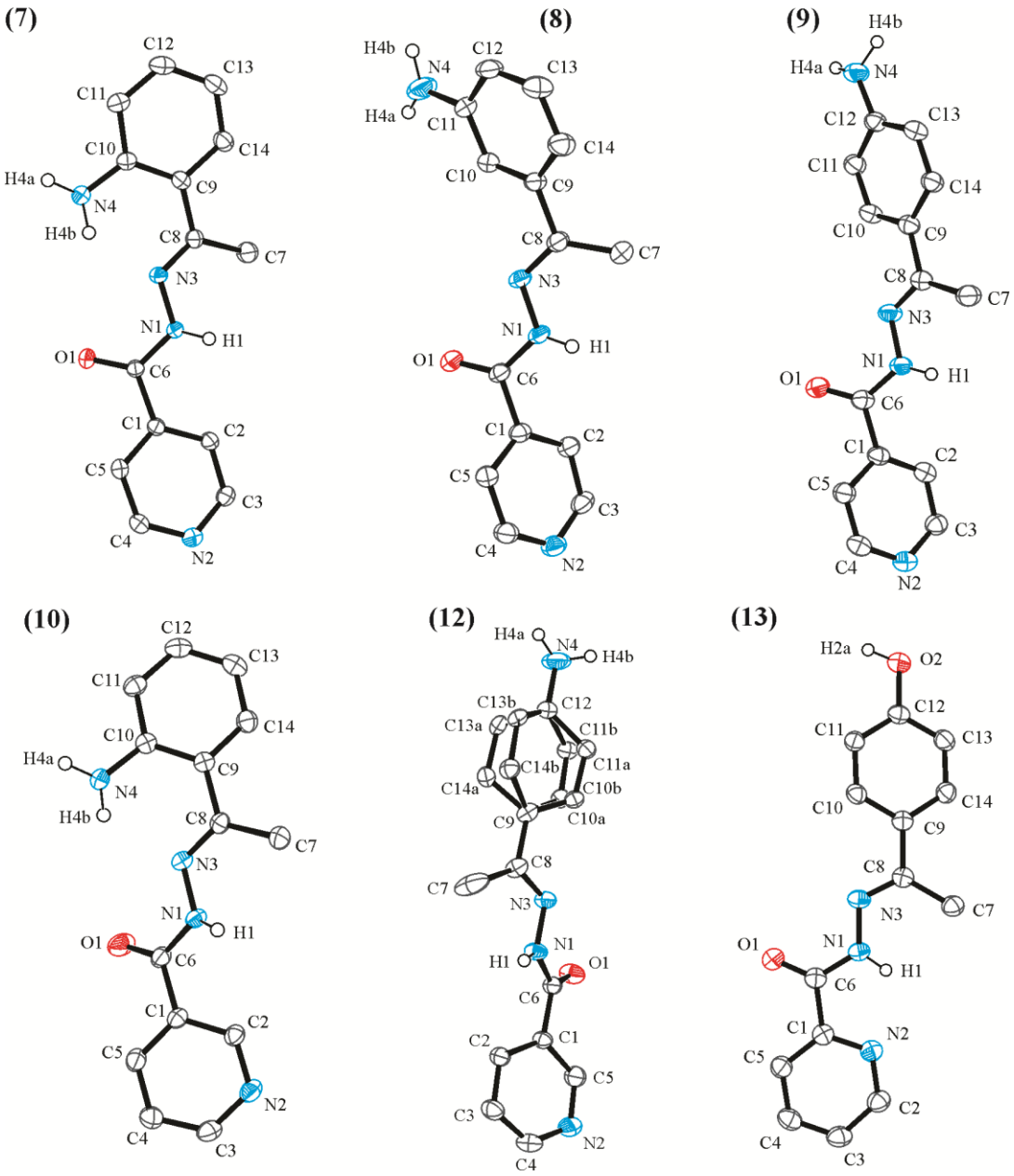


**Figure 18:** The asymmetric units **7** – **13** with **11** excluded. The displacement ellipsoids are drawn at 50 % probability level. H on C atoms are excluded for clarity. Note that **13** is the only 2-pyridyl modification made.

**Table 5**: Crystallographic data for compounds **1** – **6**.

| | **1** | **2** | **3** | **4** | **5** |
|---|---|---|---|---|---|
| Crystal data | | | | | |
| Chemical formula | $C_{14}H_{13}N_3O_2$ | $C_{14}H_{13}N_3O_2$ | $C_{14}H_{13}N_3O_2$ | $C_{14}H_{13}N_3O_2$ | $C_{14}H_{13}N_3O_2$ |
| $M_r$ | 255.27 | 255.27 | 255.27 | 255.27 | 255.27 |
| Crystal system, space group | Monoclinic, *P*2/c | Monoclinic, $P2_1/c$ | Monoclinic, $P2_1/c$ | Orthorhombic, $Pca2_1$ | Orthorhombic, *P*bcn |
| Temperature (K) | 173 | 173 | 173 | 173 | 173 |
| *a*, *b*, *c* (Å) | 19.2608 (6), 8.2010 (3), 17.4855 (6) | 21.750 (1), 7.3308 (3), 15.8777 (7) | 5.0912 (3), 29.3716 (14), 7.9954 (4) | 8.1855 (2), 11.3169 (3), 26.2683 (8) | 18.592 (9), 7.961 (4), 16.629 (12) |
| β (°) | 116.086 (1) | 103.890 (3) | 92.290 (4) | 90 | 90 |
| *V* (Å$^3$) | 2480.62 (15) | 2457.59 (19) | 1194.65 (11) | 2433.35 (11) | 2461 (2) |
| Z | 8 | 8 | 4 | 8 | 8 |
| Radiation type | Mo *K*α | Mo *K*α | Mo *K*α | Mo *K*α | Mo *K*α |
| μ (mm$^{-1}$) | 0.09 | 0.10 | 0.10 | 0.10 | 0.10 |
| Crystal size (mm) | 0.48 × 0.37 × 0.19 | 0.36 × 0.33 × 0.05 | 0.49 × 0.21 × 0.08 | 0.59 × 0.25 × 0.11 | 0.51 × 0.07 × 0.05 |
| Data collection | | | | | |
| Diffractometer | Bruker *APEX*-II CCD diffractometer | Bruker *APEX*-II CCD diffractometer | Bruker *APEX*-II CCD diffractometer | Bruker *APEX*-II CCD diffractometer | Bruker *APEX*-II CCD diffractometer |
| Absorption correction | Multi-scan *SADABS* (Sheldrick, 1996) | Multi-scan *SADABS* (Sheldrick, 1996) | Multi-scan *SADABS* (Sheldrick, 1996) | Multi-scan *SADABS* (Sheldrick, 1996) | Multi-scan *SADABS* (Sheldrick, 1996) |
| $T_{min}$, $T_{max}$ | 0.95, 0.99 | 0.96, 0.99 | 0.85, 0.95 | 0.969, 0.989 | 0.9, 0.99 |
| No. of measured, independent and observed [$I > 2\sigma(I)$] reflections | 74846, 5978, 5340 | 23608, 5268, 3526 | 8559, 2219, 1552 | 15720, 3008, 2393 | 10047, 2271, 1763 |
| $R_{int}$ | 0.024 | 0.051 | 0.051 | 0.044 | 0.094 |
| $(\sin\theta/\lambda)_{max}$ (Å$^{-1}$) | 0.661 | 0.635 | 0.606 | 0.661 | 0.606 |
| Final R indices [$I > 2\theta(I)$] | 0.0469 / 0.1297 | 0.0456 / 0.1192 | 0.0449 / 0.1011 | 0.0384 / 0.0949 | 0.0503 / 0.1418 |

**Table 5**: Crystallographic data for compounds **1** – **6** with **13** included (continued).

| | **6** | **13** |
|---|---|---|
| Crystal data | | |
| Chemical formula | $C_{14}H_{13}N_3O_2$ | $C_{14}H_{13}N_3O_2$ |
| $M_r$ | 255.27 | 255.27 |
| Crystal system, space group | Orthorhombic, $Pna2_1$ | Monoclinic, $P2_1/n$ |
| Temperature (K) | 173 | 173 |
| *a*, *b*, *c* (Å) | 7.6592 (9), 6.3516 (8), 25.292 (3) | 7.4645 (3), 19.1653 (8), 9.0435 (4) |
| β (°) | 90 | 109.968 (3) |
| *V* (Å$^3$) | 1230.4 (3) | 1215.98 (9) |
| Z | 4 | 4 |
| Radiation type | Mo *K*α | Mo *K*α |
| μ (mm$^{-1}$) | 0.10 | 0.10 |
| Crystal size (mm) | 0.42 × 0.14 × 0.03 | 0.52 × 0.27 × 0.21 |
| Data collection | | |
| Diffractometer | Bruker *APEX*-II CCD diffractometer | Bruker *APEX*-II CCD diffractometer |
| Absorption correction | Multi-scan *SADABS* (Sheldrick, 1996) | Multi-scan *SADABS* (Sheldrick, 1996) |
| $T_{min}$, $T_{max}$ | 0.98, 0.99 | 0.962, 0.971 |
| No. of measured, independent and observed [$I > 2\sigma(I)$] reflections | 10335, 1147, 1040 | 11391, 2925, 2078 |
| $R_{int}$ | 0.048 | 0.058 |
| $(\sin\theta/\lambda)_{max}$ (Å$^{-1}$) | 0.606 | 0.661 |
| Final R indices [$I > 2\theta(I)$] | 0.0429 / 0.1023 | 0.0428 / 0.0982 |

**Table 6**: Crystallographic data for compounds **7** – **12**.

| | **7** | **8** | **9** | **10** | **12** |
|---|---|---|---|---|---|
| Crystal data | | | | | |
| Chemical formula | $C_{14}H_{14}N_4O$ | $C_{14}H_{14}N_4O$ | $C_{14}H_{14}N_4O$ | $C_{14}H_{14}N_4O$ | $C_{14}H_{14}N_4O$ |
| $M_r$ | 254.29 | 254.29 | 254.29 | 254.29 | 254.29 |
| Crystal system, space group | Orthorhombic, $P2_12_12_1$ | Monoclinic, $Pc$ | Monoclinic, $P2_1/n$ | Triclinic, $P\bar{1}$ | Monoclinic, $Pc$ |
| Temperature (K) | 173 | 173 | 173 | 173 | 173 |
| $a$, $b$, $c$ (Å) | 10.3960 (3), 10.4585 (3), 11.6963 (4) | 10.2885 (4), 7.9628 (3), 7.8303 (3) | 7.7689 (3), 5.3398 (2), 29.6584 (12) | 7.7053 (2), 8.5521 (3), 9.5984 (3) | 4.8332 (7), 14.801 (2), 8.7236 (15) |
| β (°) | 90 | 102.480 (2) | 95.524 (3) | 80.815 (1), 89.535 (1), 79.932 (1) | 96.960 (6) |
| $V$ (Å$^3$) | 1271.70 (7) | 626.34 (4) | 1224.65 (8) | 614.65 (3) | 619.45 (17) |
| Z | 4 | 2 | 4 | 2 | 2 |
| Radiation type | Mo $K\alpha$ | Mo $K\alpha$ | Mo $K\alpha$ | Mo $K\alpha$ | Mo $K\alpha$ |
| μ (mm$^{-1}$) | 0.09 | 0.09 | 0.09 | 0.09 | 0.09 |
| Crystal size (mm) | 0.5 × 0.38 × 0.26 | 0.59 × 0.14 × 0.13 | 0.53 × 0.17 × 0.12 | 0.37 × 0.25 × 0.13 | 0.41 × 0.18 × 0.03 |
| Data collection | | | | | |
| Diffractometer | Bruker *APEX*-II CCD diffractometer | Bruker *APEX*-II CCD diffractometer | Bruker *APEX*-II CCD diffractometer | Bruker *APEX*-II CCD diffractometer | Bruker *APEX*-II CCD diffractometer |
| Absorption correction | Multi-scan *SADABS* (Sheldrick, 1996) | Multi-scan *SADABS* (Sheldrick, 1996) | Multi-scan *SADABS* (Sheldrick, 1996) | Multi-scan *SADABS* (Sheldrick, 1996) | Multi-scan *SADABS* (Sheldrick, 1996) |
| $T_{min}$, $T_{max}$ | 0.965, 0.98 | 0.98, 0.998 | 0.89, 0.95 | 0.97, 0.98 | 0.96, 0.989 |
| No. of measured, independent and observed [$I > 2\sigma(I)$] reflections | 10269, 1758, 1651 | 10435, 1525, 1367 | 9474, 2287, 1659 | 9868, 2265, 2049 | 8493, 1510, 1350 |
| $R_{int}$ | 0.026 | 0.049 | 0.057 | 0.019 | 0.033 |
| $(\sin\theta/\lambda)_{max}$ (Å$^{-1}$) | 0.660 | 0.661 | 0.606 | 0.606 | 0.661 |
| Final R indices [$I > 2\theta(I)$] | 0.0318 / 0.0813 | 0.0329 / 0.0794 | 0.0456 / 0.1193 | 0.0401 / 0.1091 | 0.0430 / 0.1083 |

### 4.2.1 Previous determinations

The structure of compound **9** (CSD REFCODE: SAZBOL) has been previously determined.[73] It was found that the structure contains chains of hydrogen bonds of the type N-H···N and N-H···O. However the crystal structure was never described in detail and hence redetermination was required for this purpose as well as to obtain data for comparison purposes for this study. Compound **4** (YESTOG) is also found in the Cambridge Crystallographic Structural Database (CSD) and *Zeitschrift für Kristallographie - New Crystal Structures*,[74] however the crystal structure contains a single water molecule in the asymmetric unit resulting in an altered crystal structure. Therefore it was necessary to determine and elucidate the anhydrous crystal structure for structural comparison.

### 4.2.2 Structural aggregations of derivatised isoniazid with phenol donor

**Compound 1.** Crystallises in the space group $P2_1/c$ and contains two symmetry independent molecules (A and B) in the asymmetric unit (Figure 19). Molecules A and B are interrelated by N-H···N chain hydrogen bonds of the type –A-B-A-B- (of the graph set notation (*C*7)) with pyridyl acceptor of A and donor amide of B. The phenol modification in the *ortho* position results in an intramolecular O-H···N hydrogen bond (with graph set notation (*S*6)) with the phenol hydrogen donor and the lone pairs of the hydrazone nitrogen as the acceptor. The intramolecular hydrogen bond reduces conformational flexibility of the backbone where it is aligned along the same plane as the phenyl ring.

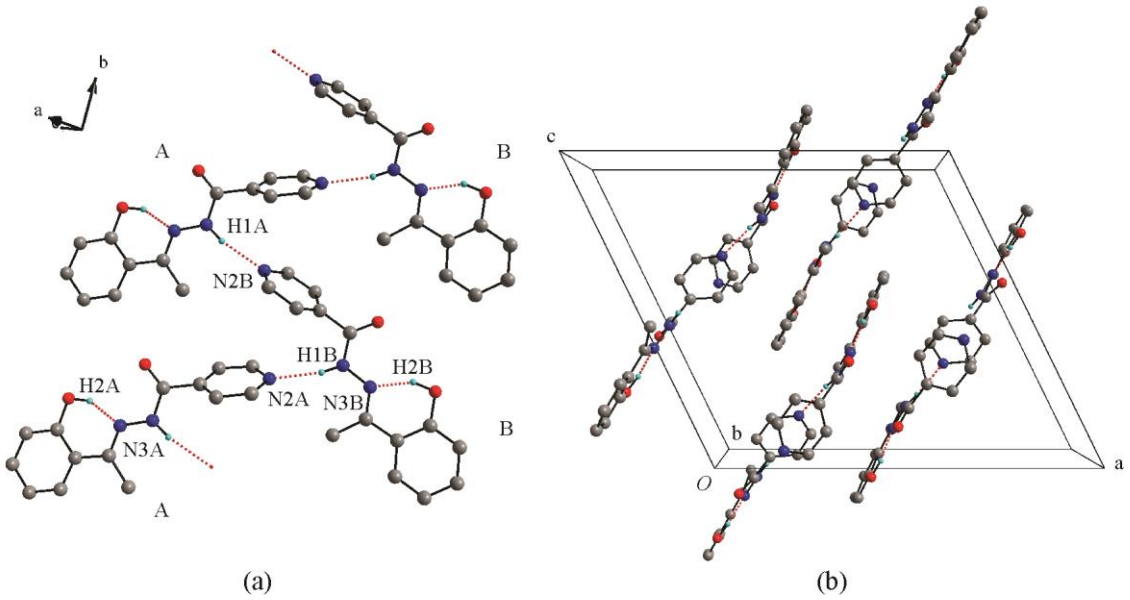


**Figure 19:** (a) Hydrogen bond motif of **1**, where molecule A and B interchangeably form a hydrogen bond chain. (b) Viewing along the *b*-axis, the alignment of the backbone with the phenyl ring is observed.

**Compound 2.** Crystallises in the space group $P2_1/c$ with two symmetry independent molecules A and B in the asymmetric unit (Figure 20). Molecules A and B form chain linkages -A-B-A-B- by utilising the N-H···N hydrogen bond. When viewing along the *b*-axis of the unit cell, the molecules form additional hydrogen bonds creating columns of -A-A-A-A- and -B-B-B-B-. Column A is characterised by the N-H···N hydrogen bond utilising the amide donor and pyridyl acceptor. The column is further characterised by π···π (3.820(1) Å) stacking interactions occurring between the pyridine rings.

Column B is characterised by the O-H···O hydrogen bond utilising a phenol donor and carbonyl acceptor. It should be noted that the aromatic rings of molecule B do not exhibit π···π stacking interactions. The contribution of the phenol donor placed in *meta* position contributes to an overall large order hydrogen bond ring with graph set notation $R_6^6(60)$. These observed hydrogen bond rings result from the hydrogen bond connectivity of the columns internally and externally when joined together.

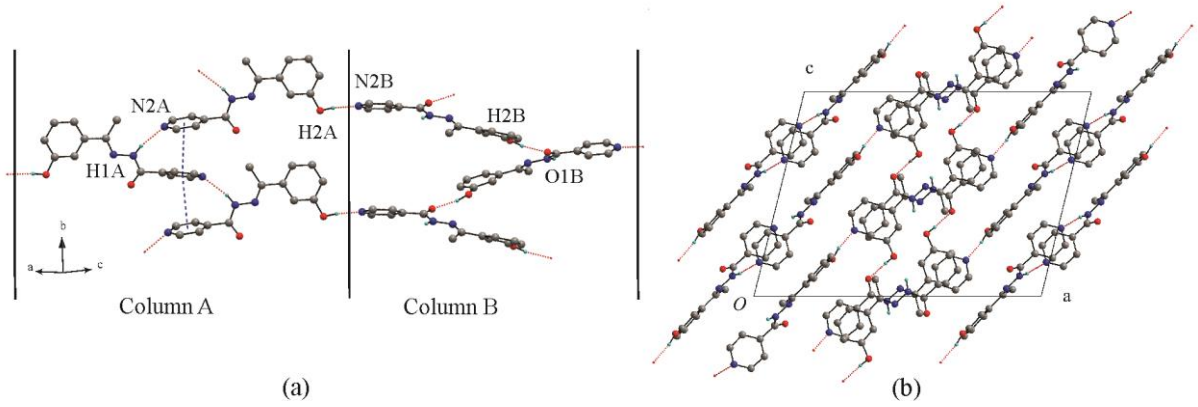


**Figure 20:** (a) Two hydrogen bond columns are formed, including larger hydrogen bond rings are formed between connecting the columns by utilising the phenol donor in the *meta* position of the phenyl ring in **2**. (b) Viewing along the *b*-axis, the hydrogen bond rings are observed as well as the chains running along the *ac* direction.

**Compound 3.** Crystallises in the space group $P2_1/c$ with a single molecule in the asymmetric unit (Figure 21). This compound forms a N-H···O hydrogen bond between amide donor and carbonyl acceptor and O-H···N hydrogen bond between phenol donor (now in the *para* position) and pyridyl *N* acceptor along the *b*-axis. The amide hydrogen bond (2.31 Å) is the longer of the two hydrogen bonds where the phenol hydrogen bond is 1.94 Å. The molecules adopt a head to tail conformation and in conjunction with both hydrogen bond nodes a larger hydrogen bond ring system is observed with graph set notation $R_4^4(34)$.

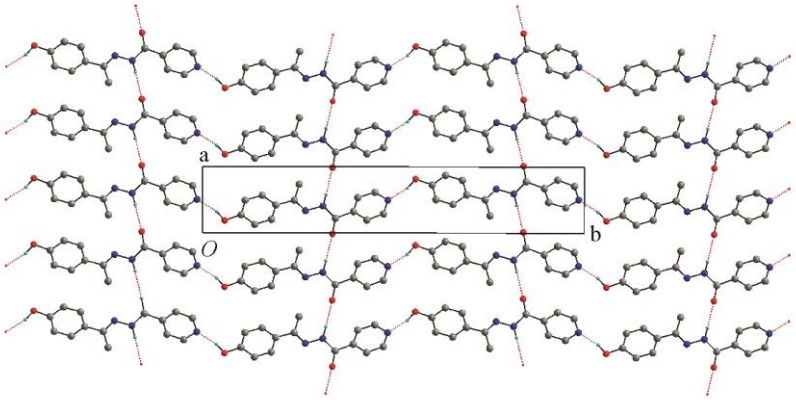


**Figure 21:** Compound **3** forms a 2D hydrogen bond array with amide donor and phenol donor in the *para* position.

**Compound 4**. With compound **4** the phenol donor is now changed to the *ortho* position and pyridyl nitrogen shifted to the 3-position in the pyridine ring (Figure 22). This compound crystallises in the space group *P*ca2$_1$ with two symmetry independent molecules A and B in the asymmetric unit. Molecules A and B form an array of chain hydrogen bonds; by utilising the amide donor and carbonyl acceptor of the form N-H···O. The hydrogen bond chains form independently of one another in an -A-A-A-A- and -B-B-B-B- chains; however they do run in a parallel fashion along the *b*-axis of the unit cell. For both molecules A and B the phenol donor in the *ortho* position forms an intramolecular O-H···N hydrogen bond with the acceptor lone pair of the hydrazone nitrogen in the same way as seen in compound **1**. Three π···π interactions are observed within this structure: the pyridine rings of both molecules A and B with a comparable distances of 4.094(1) Å for A and 4.106(1) Å for B; and between the phenol rings (Figure 22c) for A and B with distance 3.167(1) Å.

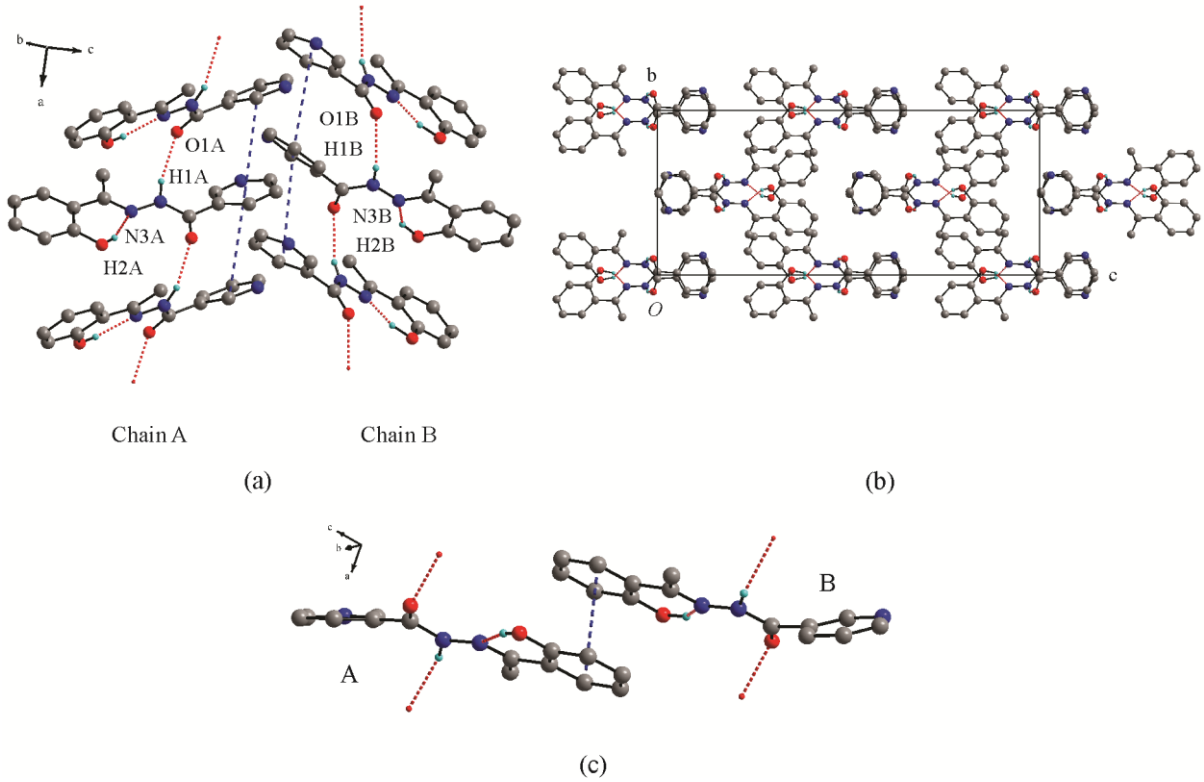


**Figure 22:** Packing representations of compound **4**. (a) With pyridyl nitrogen in the 3-position; parallel hydrogen bond chains are formed from symmetry independent molecules A and B. The hydrogen bond chains run along the *a*-axis with the pyridine rings involved in π···π interactions. (b) Hydrogen bond chains for A and B form along the *a* axis whilst these columns pack along each other along the *c* direction and alternate between column A and B along the *b* axis. (c) π···π interactions between phenol rings of molecule A and B are observed.

**Compound 5**. This compound crystallises in the space group *P*bcn with a single molecule in the asymmetric unit (Figure 23). A N-H···O hydrogen bond is formed between amide donor and carbonyl acceptor. When both the phenol donor and pyridine nitrogen are placed in the *meta* position, a O-H···O hydrogen bond chain is observed running along the *c*-axis. These chain hydrogen creates a 2D network hydrogen bond and additionally a hydrogen bond ring with graph set notation $R_4^4(32)$.

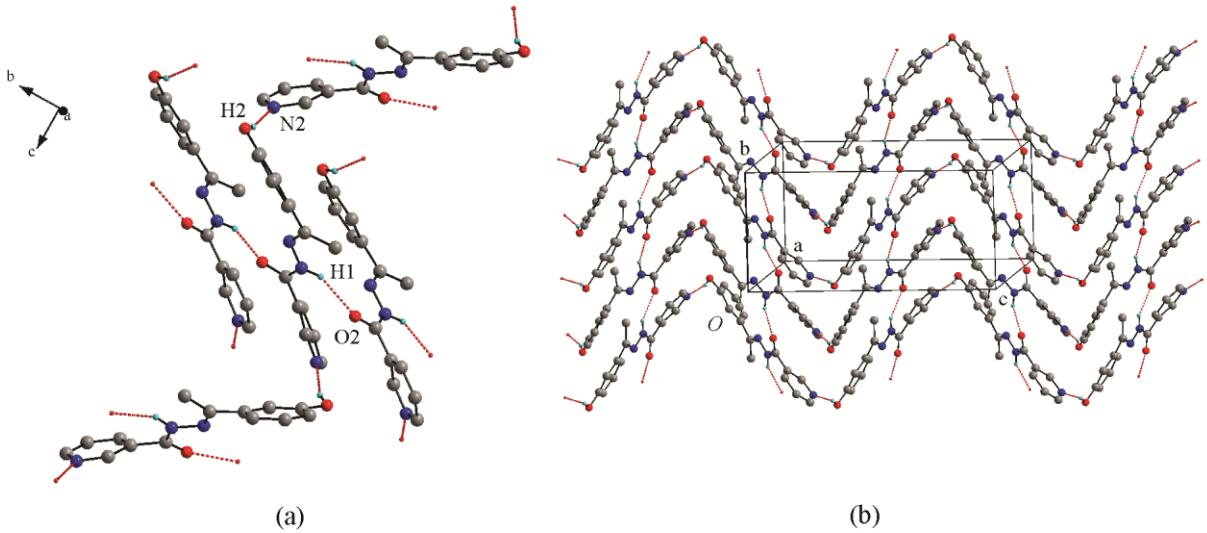


**Figure 23:** Packing representations for compound **5**. (a) Hydrogen bond chains are observed with the *meta* positioned phenol donor and 3-positioned pyridyl nitrogen. (b) A head-to-tail molecular aggregate is observed running along the *c*-axis.

**Compound 6.** This compound crystallises in the space group *P*na2$_1$ with a single molecule in the asymmetric unit (Figure 24). A N-H···O hydrogen bond is created between the amide hydrogen donor and carbonyl acceptor of the neighbouring molecule. With the phenol donor in the *para* position, it forms an O-H···H hydrogen bond with the pyridyl acceptor along the *c*-axis of the unit cell and contributes to an overall hydrogen bond ring ($R_6^6(40)$). When the packing motif is viewed along the *b*-axis, a head-to-tail zig-zag aggregation is observed including a 2D chain hydrogen bond in the direction of the *a* and *c* axes.

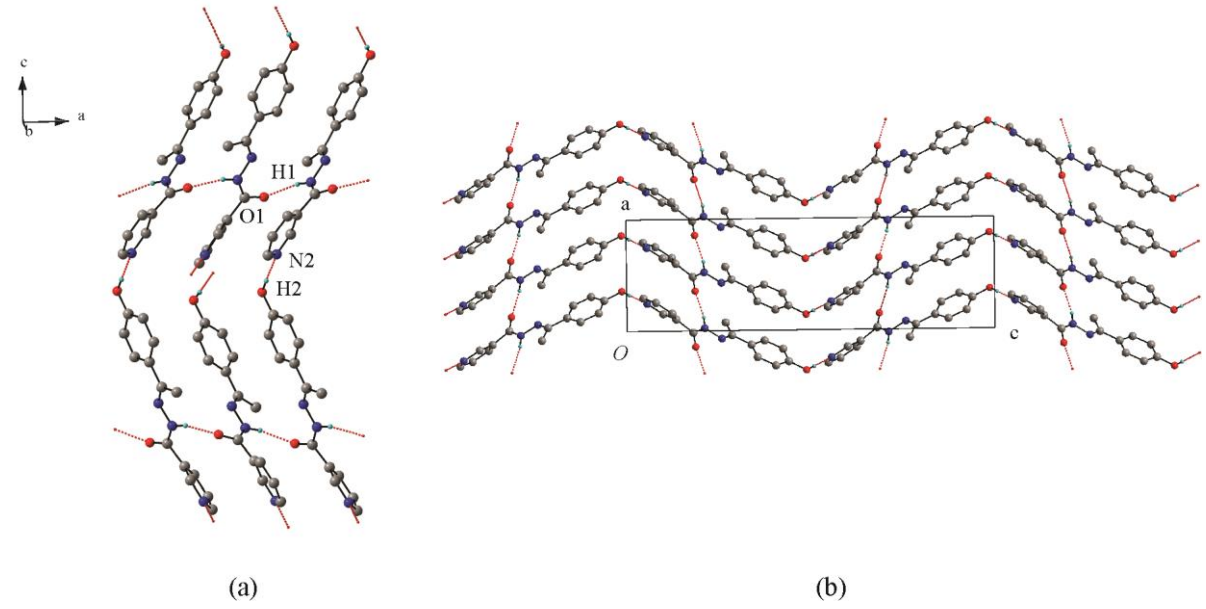


**Figure 24:** (a) Compound **6** forms a 2D sheet of hydrogen bonds by utilising the amide donor and carbonyl acceptor pair along with the phenol donor and pyridyl *N* pair. By utilising six hydrogen bonded molecules, a larger ring is formed with graph set notation $\mathbf{R_6^6}(40)$ while the centre of this ring formation provides further linkage of neighbouring molecules. (b) The head-to-tail molecular aggregation is observed with the hydrogen bond chains running in the *a* and *c* axis.

### 4.2.3 Structural aggregations of derivatised isoniazid with amino donor

**Compound 7**. This compound crystallises in the $P2_12_12_1$ space group with one molecule in the asymmetric unit (Figure 25). This molecule has an amino group in the *ortho* position on the phenyl ring. This modification acts as a potential bifurcated hydrogen bond donor and single acceptor. This molecule contains the largest number of hydrogen bonds amongst the isoniazid derivatives. The first hydrogen bond takes place between amide hydrogen donor and pyridyl *N* acceptor to form a N-H···N hydrogen bond chain with graph set notation *C*(7). The amino group forms an intramolecular N-H···N hydrogen bond by donating to the acceptor lone pair of the hydrazone nitrogen. The second hydrogen bond that the amino group forms is a N-H···O chain hydrogen bond by donating to a neighbouring carbonyl acceptor. The hydrogen bond chains form an infinite 2D array and combination of these hydrogen bonds forms a hydrogen bonded ring with graph set notation $R_6^6(26)$.

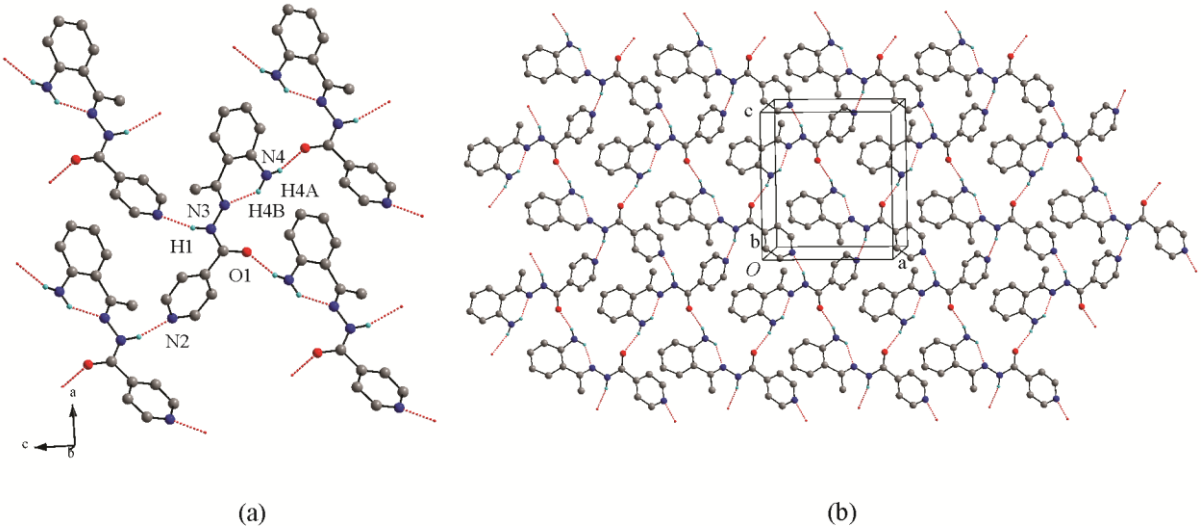


(a) (b)

**Figure 25:** (a) Compound **7** possesses the greatest number of hydrogen bonds amongst the isoniazid derivatives and forms a 2D hydrogen bond chain array. (b) The 2D hydrogen sheets are demonstrated extending along the *a* and *c* axes forming larger hydrogen bond rings.

**Compound 8**. This compound crystallises in the space group *P*c with one molecule in the asymmetric unit (Figure 26). This compound has the $–NH_2$ group on the *meta*- position of the phenyl ring. The amide hydrogen donates to the carbonyl acceptor of a neighbouring molecule to form a N-H···O chain hydrogen bond. The interaction between the amino hydrogen donor and pyridyl nitrogen acceptor may appear to be a hydrogen bond however the distance of DHA is more indicative of a short contact interaction (2.416 Å) with a DHA angle of 160°. The amino donor groups are all aligned in the direction of the *c*-axis of the unit cell.

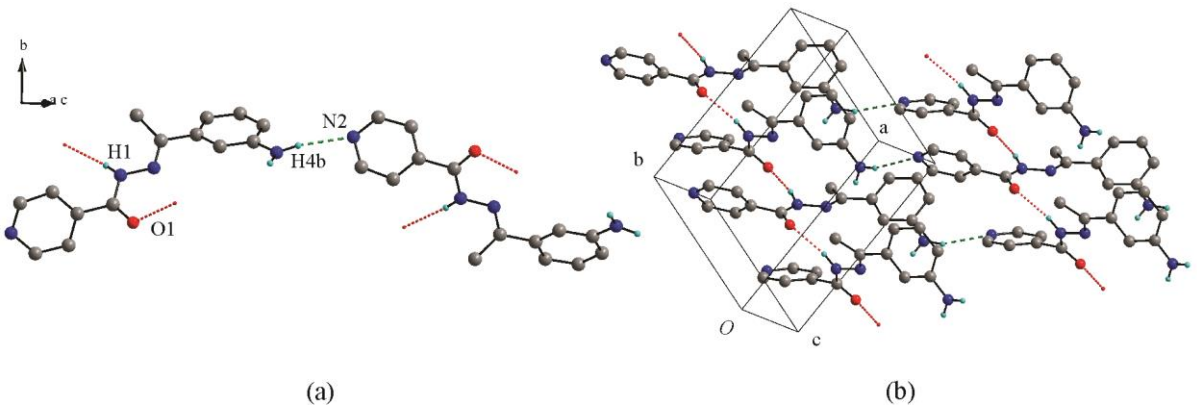


**Figure 26:** (a) Compound **8** forms a hydrogen bond with amide donor and carbonyl acceptor. The N-H···N(pyridyl) is a short contact interaction (2.416 Å). (b) The *meta* positioned amino group always faces the same direction for each molecule.

**Compound 9**. This compound crystallises in the space group $P2_1/n$ with one molecule in the asymmetric unit (Figure 27). This compound has the amino donor group modified in the *para*- position of the phenyl ring. In this position the modification is utilised in this crystal structure by forming chain hydrogen bonds. By donating to the neighbouring pyridyl acceptor, it forms linear head to tail N-H···N chains with graph set notation *C*(14). A short contact interaction is formed between amide donor and carbonyl acceptor (2.485 Å) with DHA of 166°. The unit cell is filled by two hydrogen bonded chains in parallel with carbonyl acceptors facing opposing directions to each other. Furthermore the crystal structure contains a second amino hydrogen interacting with the neighbouring phenyl ring N-H···π (2.830 A).

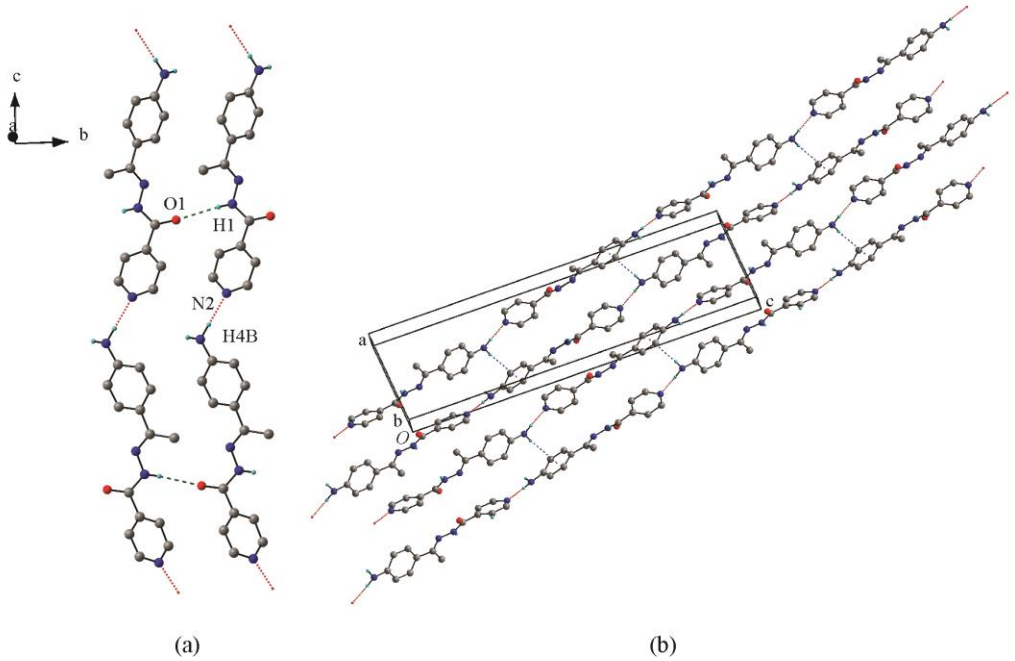


**Figure 27:** (a) Compound **9** forms a hydrogen bond between the amino donor and pyridyl acceptor; however a short contact interaction is observed between the amide donor and carbonyl acceptor (2.485 Å). (b) A head-to-tail motif is observed with amino hydrogen donor contributing to a N-H···π (2.830 A) interaction.

**Compound 10**. This compound crystallises in the space group *P*-1with one molecule in the asymmetric unit (Figure 28). This molecule has the pyridyl nitrogen placed in the 3- position whilst modifying the phenyl ring by the addition of an amino donor group to the *ortho* position. The amide hydrogen donor forms a N-H···N hydrogen bond by donating to the acceptor lone pair of the amino group. An intramolecular N-H···N hydrogen bond is formed between amino hydrogen donor and hydrazone acceptor. The second hydrogen coming off the amino group donates to the pyridyl acceptor of the neighbouring molecule in a N-H···N hydrogen bond. These hydrogen bonding nodes contribute to a hydrogen bond ring (exclusively containing nitrogen and hydrogen) with graph set notation $R_4^4(10)$. A secondary hydrogen bond ring is formed between four molecules with graph set notation $R_4^4(20)$. The carbonyl acceptors are only involved in short contact interactions and face opposite directions during the ring formations. Lastly, $\pi\cdots\pi$ interactions are observed between the phenyl and pyridyl rings (3.630 Å).

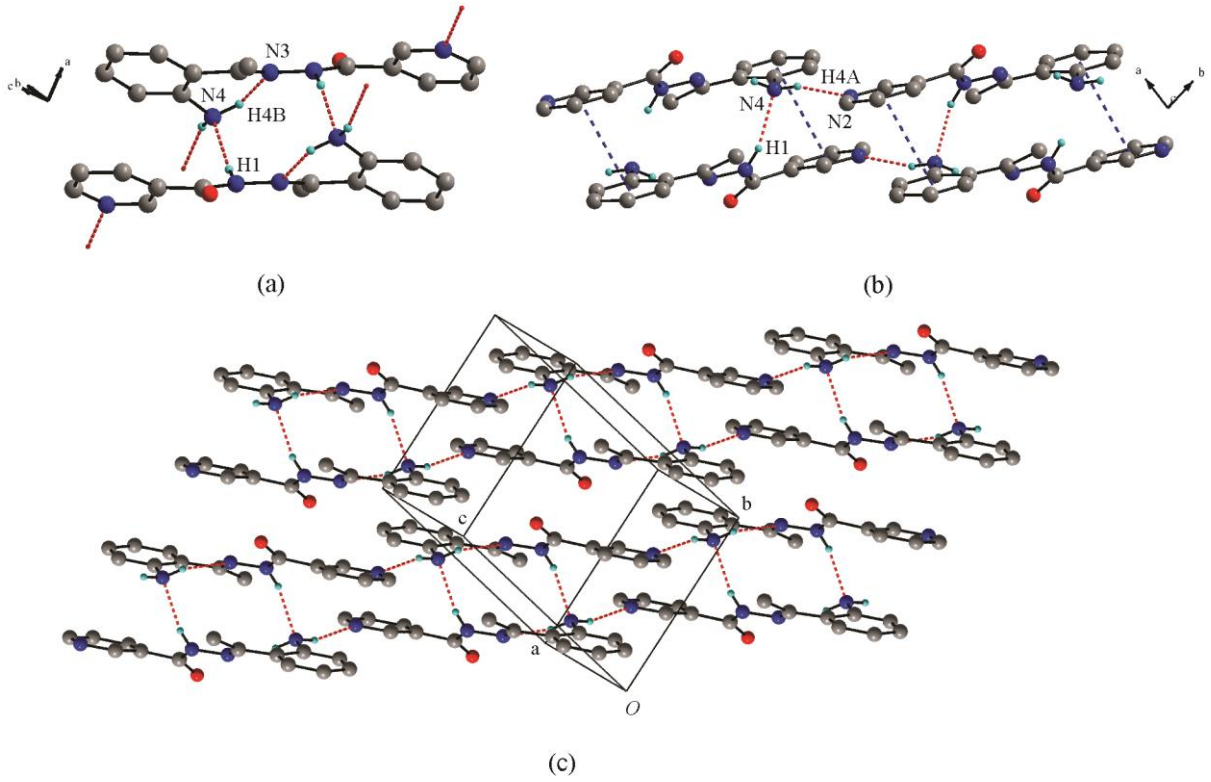


**Figure 28:** (a) The *ortho* positioned amino group of compound **10** generates a variety of hydrogen bond rings. By utilising the amino, amide and hydrazone groups, a hydrogen bonded ring is formed using exclusively N-H···N bonds. (b) With the pyridyl nitrogen in the 3- position, a larger hydrogen ring is formed by utilising the second amino hydrogen donating to pyridyl nitrogen. $\pi\cdots\pi$ interactions are shown in blue (c) The hydrogen bond interactions are placed in context with the rings forming side by side.

**Compound 12**. This compound crystallises in the space group *P*c with one molecule in the asymmetric unit (Figure 29) with a 50% disorder about the amino rings. This compound has the amino donor group attached to the *para* position of the phenyl ring. This position enables the molecule to crystallise in a 2D chain hydrogen bond array. The first N-H···O hydrogen bond chain extends along the *a*-axis of the unit cell where the molecule utilises the amide donor and carbonyl acceptor. The second N-H···N hydrogen bond is a chain hydrogen bond running along the *b*-axis of the unit cell where the amino group donates to pyridyl acceptor.

Only short contact interactions are observed for the second hydrogen coming off the amino donor. In conjunction with the first and second hydrogen bond chain described, a ring hydrogen bond with graph set notation $R_4^4(32)$ is formed.

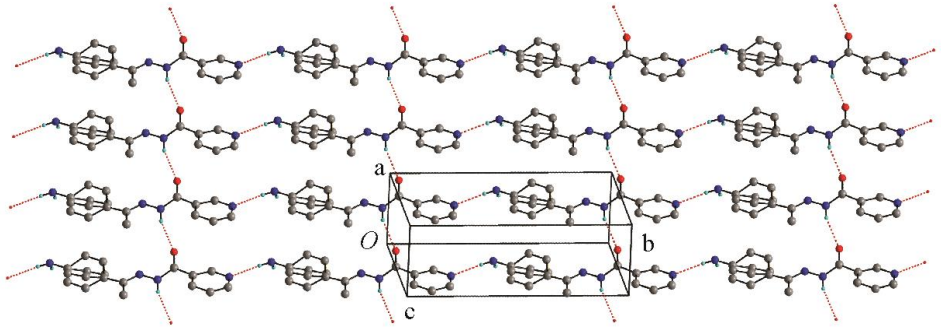


**Figure 29:** In compound **12** the amino donor placed in the *para* position with pyridyl nitrogen in the 3-position creates a 2D array of hydrogen bond chains (the amide donor and carbonyl acceptor utilised as the second hydrogen bond chain). A disorder of 50 % for the phenyl rings is observed.

### 4.2.4 Structural description of pyridyl isomer at the 2- position

**Compound 13**. This compound crystallises in the space group $P2_1/n$ with one molecule in the asymmetric unit (Figure 30). With the pyridyl nitrogen placed at the 2-position it interacts favourably with the amide donor to form a short contact of 2.16 Å. This essentially 'locks up' the pyridyl nitrogen, preventing hydrogen bond formation to any neighbouring donors. A dimeric hydrogen bond ring is formed with the phenol donor and carbonyl acceptor O-H···O; notably, this hydrogen bond has a distance of 1.81 Å. The dimeric clusters are found to arrange themselves in a planar arrangement with a larger zig-zag formation proceeding throughout the unit cell.

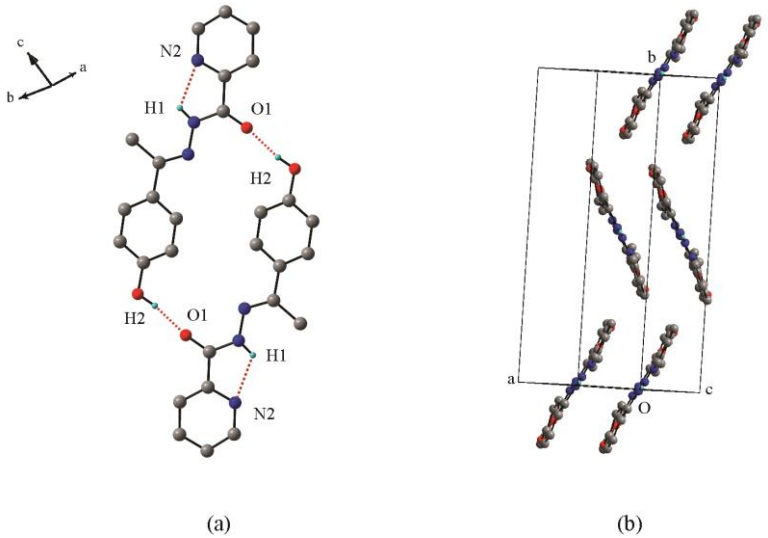


**Figure 30:** (a) Compound **13** forms a dimeric cluster with phenol donor and carbonyl acceptor. The pyridyl nitrogen forms an interaction with the amide hydrogen. (b) The linear dimeric clusters form zig-zag patterns proceeding along the *b*-axis.

**Table 7**: Hydrogen bond parameters for compounds **1** – **6**.

| D-H···A | D-H(Å) | H···A (Å) | D···A (Å) | D-H···A (°) | Symmetry Transformations |
|---|---|---|---|---|---|
| **1** | | | | | |
| N(1A)-H(1A)···N(2B) | 0.92(2) | 2.11(2) | 3.009(2) | 167(2) | x, y-1, z |
| O(2A)-H(2A)···N(3A) | 0.93(2) | 1.73(2) | 2.571(1) | 150(2) | - |
| N(1B)-H(1B)···N(2A) | 0.90(2) | 2.10(2) | 2.987(2) | 169(2) | - |
| O(2B)-H(2B)···N(3B) | 0.94(2) | 1.71(2) | 2.565(1) | 149(2) | - |
| **2** | | | | | |
| O(2A)-H(2A)···N(2B) | 0.84(1) | 1.92(1) | 2.754(2) | 171(1) | - |
| O(2B)-H(2B)···O(1B) | 0.84(2) | 1.90(2) | 2.733(2) | 172(3) | -x+1, y-1/2, -z+1/2 |
| N(1A)-H(2A1)···N(2A) | 0.88(2) | 2.16(1) | 3.021(2) | 165(2) | -x, y+1/2, -z+5/2 |
| N(1B)-H(2B1)···O(2B) | 0.88(1) | 2.61(1) | 3.249(2) | 131(2) | x, -y+3/2, z+1/2 |
| **3** | | | | | |
| N(1)-H(1)··· O(1) | 0.88(1) | 2.31(3) | 3.099(2) | 149(1) | x+1, y, z |
| O(2)-H(2)···N(2) | 0.84(2) | 1.94(1) | 2.717(3) | 154(3) | -x+1, y-1/2, -z+3/2 |
| **4** | | | | | |
| N(1B)-H(1B)···O(1B) | 0.83(3) | 2.23(3) | 2.987(3) | 153(3) | x-1/2, -y, z |
| N(1A)-H(1A)···O(1A) | 0.94(4) | 2.10(4) | 2.953(3) | 149(3) | x-1/2, -y+1, z |
| **5** | | | | | |
| N(1)-H(1)···O(1) | 0.90(3) | 2.37(3) | 3.200(3) | 154(2) | -x+1/2, y-1/2, z |
| O(2)-H(2A)···N(2) | 0.83(3) | 1.99(3) | 2.790(3) | 162(3) | x, -y+1, z-1/2 |
| **6** | | | | | |
| N(1)-H(1)···O(1) | 0.91(5) | 2.02(5) | 2.896(4) | 160(4) | x-1/2, -y+1/2, z |
| O(2)-H(2A)···N(2) | 0.89(5) | 1.85(6) | 2.735(4) | 175(5) | -x+1, -y, z+1/2 |

**Table 8**: Hydrogen bond parameters for compounds **7** – **13**.

| D-H···A | D-H(Å) | H···A (Å) | D···A (Å) | D-H···A (°) | Symmetry Transformations |
|---|---|---|---|---|---|
| **7** | | | | | |
| N(4)-H(4A)···O(1) | 0.91(2) | 2.13(2) | 3.019(2) | 163(2) | x-1/2, -y+1/2, -z+1 |
| **8** | | | | | |
| N(4)-H(4B)···N(2) | 0.91(4) | 2.41(4) | 3.289(3) | 161(3) | x+1,-y+1,z+3/2 |
| **9** | | | | | |
| N(4)-H(4B)···N(2) | 0.96(2) | 2.04(3) | 3.001(3) | 179(2) | x+1/2, -y+1/2, z+1/2 |
| **10** | | | | | |
| N(1)-H(1)···N(4) | 0.92(2) | 2.13(2) | 3.008(1) | 159(1) | -x, -y+1, -z+1 |
| N(4)-H(4A)···N(2) | 0.90(2) | 2.18(2) | 3.059(2) | 163(1) | x-1, y+1, z |
| N(4)-H(4B)···N(3) | 0.89(2) | 2.12(2) | 2.707(1) | 122(1) | - |
| **12** | | | | | |
| N(1)-H(1)···O(1) | 0.90(3) | 2.20(3) | 3.004(3) | 149(3) | x-1, y, z |
| **13** | | | | | |
| N(1)-H(1)···N(2) | 0.86(2) | 2.16(2) | 2.632(2) | 114(1) | |
| O(2)-H(2A)···O(1) | 0.89(2) | 1.81(2) | 2.683(2) | 168(1) | -x+1, -y, -z |

### 4.3 Comparisons of changing substituted positions

Altering the donor position on the phenyl ring whilst keeping the pyridyl nitrogen constant (or shifting the pyridyl nitrogen) creates an unpredictable variety of supramolecular aggregations amongst the isomeric compounds. In order to advance structural prescience of the series, trends need to be identified. The phenol and amino donors with the exception of **2**, **7** and **9** have a preference to form hydrogen bonds with the pyridyl nitrogen as opposed to the available carbonyl acceptor. Consequently it is observed that the carbonyl acceptors are frequently positioned towards the periphery of the molecule during hydrogen bond creation. The molecules utilise the carbonyl acceptor to form chain hydrogen bonds with amide donor. This orientation is noticed throughout the entire series. Notably when the pyridyl nitrogen is shifted to the 2-position the acceptor becomes unavailable to a form hydrogen bond with neighbouring acceptors. This effect of locking the aromatic ring in place with a hydrogen bond is observed in the interaction of the *ortho* donor and hydrazone acceptor locking up the ring. It is favourable for the 2-pyridyl ring to be orientated closest to the amide hydrogen as it is not only able to form a strained hydrogen bond interaction but the lone-pair repulsions are minimised between the carbonyl acceptor and pyridyl nitrogen. With these conditions in place it is safe to assume that the 2-pyridyl nitrogen and amide donor will always be unavailable for hydrogen bond formation to neighbouring molecules. The addition of a secondary hydrogen donor (amino) over a primary hydrogen donor (phenol) is only manifested in the generation of hydrogen bonds when placed in the *ortho* position of the phenyl ring. The hydrogen bond count is increased by the self-intramolecular bond available via the hydrazone.

This effect induces planarity within the backbone and the phenyl ring of the molecule; however this planarity is only strongly felt up to the hydrazone nitrogen. Some compounds **1** and **4** may express this planarity as far as the carbonyl acceptor; however, this effect is only observed for the phenol donor. A trend is observed when the donor is placed in the *meta* position as it always forms a hydrogen bond with the pyridyl nitrogen. Whereas the phenol donor only donates to the pyridyl acceptor, in some cases the amino donor will donate a hydrogen to form an N-H···π interaction with a neighbouring aromatic ring. Therefore the identity of the donor in this position has little effect on maximising the hydrogen bond count within the crystal structure. When the donor is placed in the *para* position, chain hydrogen bonds running along the skeletal backbone of the molecule are observed. The shifting of nitrogen by one position in the pyridine ring does not disrupt hydrogen bond formation, however an alteration in supramolecular aggregation is observed. When the position the amino group is poised in the direction of pyridyl lone pairs, it enables the orientation of the molecules to favourably enable the hydrogen bond chain formed between the amide donor and carbonyl acceptor.

The conformations of each molecule can be described by defining the orientations of the rings and conformations of the backbone linking the aromatic rings (see Scheme 2 and Table 9). The presence of the double bond constricts the conformational flexibility of the hydrazone functional group and it is found that all the compounds presented in this study are synthesised in the *E* conformation at the C-N double bond. Consequently H(1A) on the amide group is also found to be *trans* to the carbonyl acceptor O1 and shares the same region of space as the methyl group. The backbone (C-N-N-C) torsional angles deviate by no more than 20° from 180° therefore these angles correspond to the observed *trans* amide linkages in all the compounds. These deviations from 180° suggest that the compounds are conformationally flexible when subjected to various packing conditions.

Overall there is a greater deviation from the plane for the pyridyl ring than that of the phenyl ring with the greatest deviation experienced by molecule A in compound **1** (easily observed in Figure 19). However it is common amongst these compounds for the pyridyl ring to deviate out of plane with a mean deviation of 143°. The exception is compound **13** where the pyridyl ring is closest to the plane with 175°. This effect is observed by the locking in of the pyridyl nitrogen in the 2- position with the amide hydrogen. Overall there is less of an effect of shifting out of plane for the phenyl ring with mean deviation of 164° with notable exceptions of **5**, **8** and ring A of disordered compound **12**. It is noticed most when the phenol donor is in the *ortho* position, the phenyl ring is aligned closest to the plane of the back bone for the series of compounds; whereas with the amino donor in the *ortho* the deviation from the backbone is greater.

**Table 9**: Selected torsional angles for compounds **1** – **13** (**11** excluded).

| | **Pyridyl ring (°)** | **Backbone (°)** | **Phenyl ring (°)** |
|---|---|---|---|
| | **C5-C1-C6-N1** | **C6-N1-N3-C8** | **N3-C8-C9-C14** |
| **1A** | 121.01(1) | 174.55(1) | -177.65(1) |
| **B** | -124.05(1) | -165.48(1) | 170.90(1) |
| **2A** | -125.0(2) | -166.43(2) | -177.90(2) |
| **B** | -148.89(2) | -176.24(2) | 154.76(2) |
| **3** | 153.70(2) | -161.78(2) | -177.60(2) |
| **4A** | 151.2(4) | -175.0(3) | 177.0(2) |
| **B** | -138.8(4) | 178.8(3) | -177.1(2) |
| **5** | -138.3(2) | -178.51(2) | 138.6(2) |
| **6** | 135.8(4) | -174.6(3) | 172.6(3) |
| **7** | 155.82(2) | -162.78(1) | 164.34(2) |
| **8** | 131.75(2) | 178.17(2) | 145.8(2) |
| **9** | 142.2(2) | 159.93(2) | 167.05(2) |
| **10** | 151.43(1) | -171.27(1) | -153.16(1) |
| **12A** | -150.7(2) | 161.0(2) | 149.2(3) |
| **B** | | | -164.5(4) |
| **13** | 175.65(1) | 177.26(1) | -164.37(1) |

# CHAPTER 5 THERMAL BEHAVIOUR STUDIES FOR ISONIAZID DERIVATIVES

This chapter introduces the thermal behaviour for the pyridine based isoniazid derivatives. Compounds that have been identified for further polymorphic investigation are highlighted.

## 5.1 Introduction

In addition to describing the supramolecular aggregates of the compounds **1** – **13**, a preliminary study was undertaken to assess the polymorphic space for these compounds. The main idea behind this is determine whether or not the modification and/or position of the hydrogen bond donor disrupts or enhances the polymorphic ability observed compared to the highly polymorphic parent IPH. Selected compounds are presented below that show either interesting or promising thermal behaviour when heating from 25°C to its respective melting point and cooled back down to 25°C.

## 5.2 Thermal behaviour of IPH

The thermal behaviour of IPH has been comprehensively covered in Chapter 3. However, for comparison purposes, the phase relationships represented by DSC traces of IPH is reproduced here. For a full description of the events in Figure 15 refer to Chapter 3, and for representative traces for other heating cycles polymorphs of IPH refer to the Appendices.

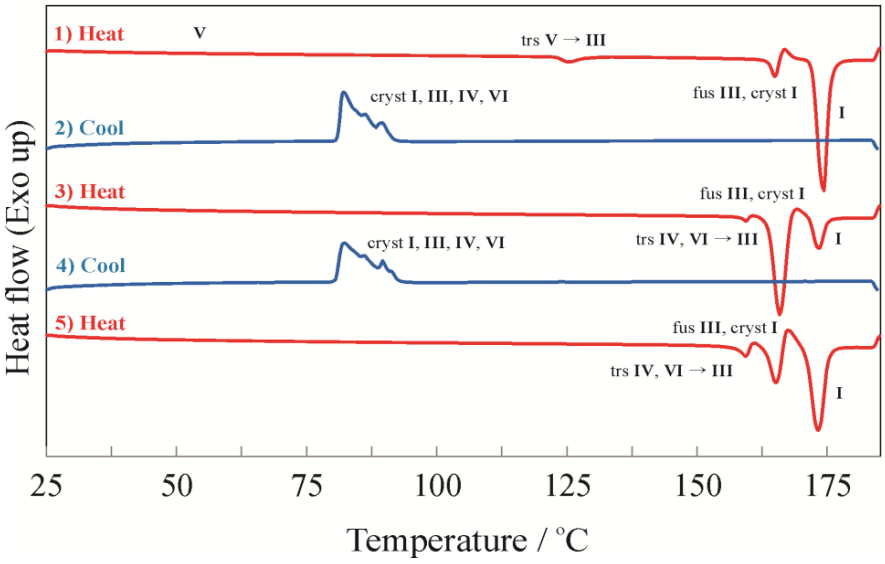


**Figure 15:** DSC traces of five successive heating /cooling runs beginning with IPH **V**. The heating rate is 15°C/min.

## 5.3 Thermal events of interest for compounds 1 – 13

Representative DSC traces for compounds **1** – **13** are given below. For the remaining traces not shown here, refer to the Appendices. Thermal events of interest for the compounds include super-cooled melts, higher melting points and new melting points after recrystallization from the melt.

### 5.3.1 Thermal events of interest for phenol modified compounds

Figure 31 is chosen as a representative trace for compounds **1** – **3**, **5** and **6** as these compounds do not recrystallise after melting and no further thermal events for such compounds are observed. It should be noted that compounds **3** and **6** with the modification placed in the *para* positions show significantly higher melting points compared to the rest of the phenol compounds.

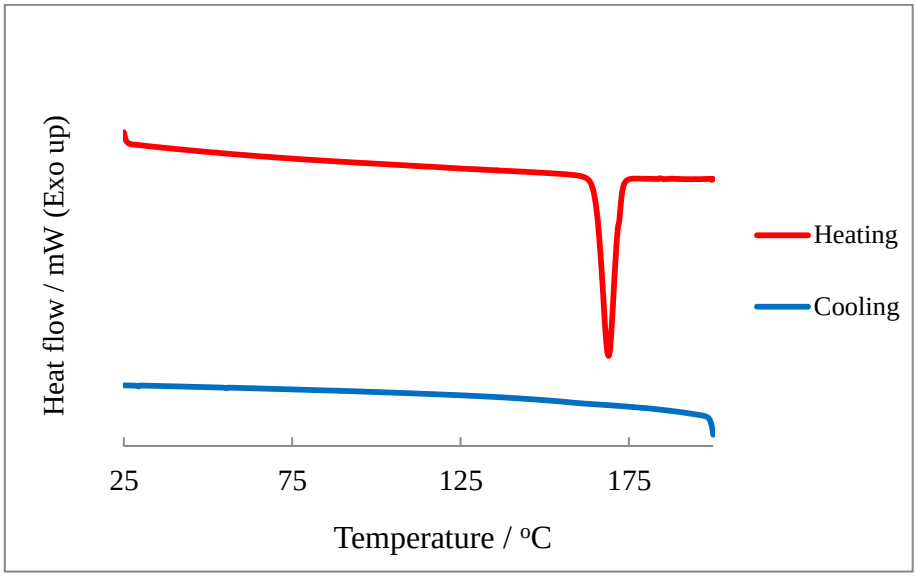


**Figure 31:** DSC trace of **1** showing the lack of a crystallization exotherm on cooling, forming a super-cooled melt.

Compound **4** is the first of the phenol modifications that potentially represents new forms as the melting point for the new phase after recrystallization from melting is significantly different to warrant further investigation. The compound does not crystallise upon cooling, however during the heating cycle at 128°C a broad exotherm is observed representing crystallization. Upon further heating a new melting point is observed (174°C) which indicates a new form. This lower melting point is continuously observed when repeating multiple heating and cooling cycles. Furthermore the crystallization of this new single form appears to be homogenous in the DSC pan as there is no indication of the phase present with the higher melting point.

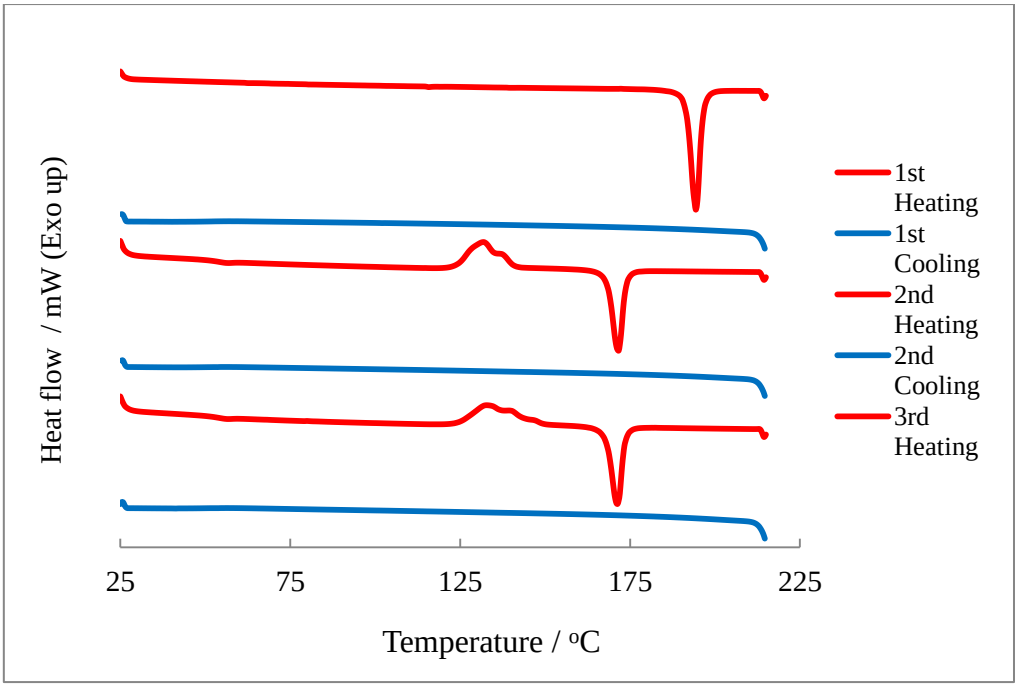


**Figure 32:** DSC trace of **4**. Recrystallization occurs only during the 2nd heating cycle, when a lower melting point for this form is observed. This thermal cycle is then repeated for the 3rd heating/cooling cycle.

### 5.3.2 Thermal events of interest for amino modified compounds

The DSC trace for compound **8** is shown in Figure 33 where there may be a secondary form crystallising for this compound. Upon cooling after melt a slight exotherm is observed at 113°C (could be recrystallization) and again when the heating cycle is recommenced (phase transition or further recrystallization). Thereafter a lower melting point is observed at 195°C as opposed to the original 203°C. Further heating and cooling do not significantly alter the thermal events; however, no exotherm peaks are observed during the cooling cycle. For the 3rd heating cycle a greater exotherm is observed, indicating that recrystallization is a single event as opposed to the separate crystallizations during the 1st cooling and 2nd heating.

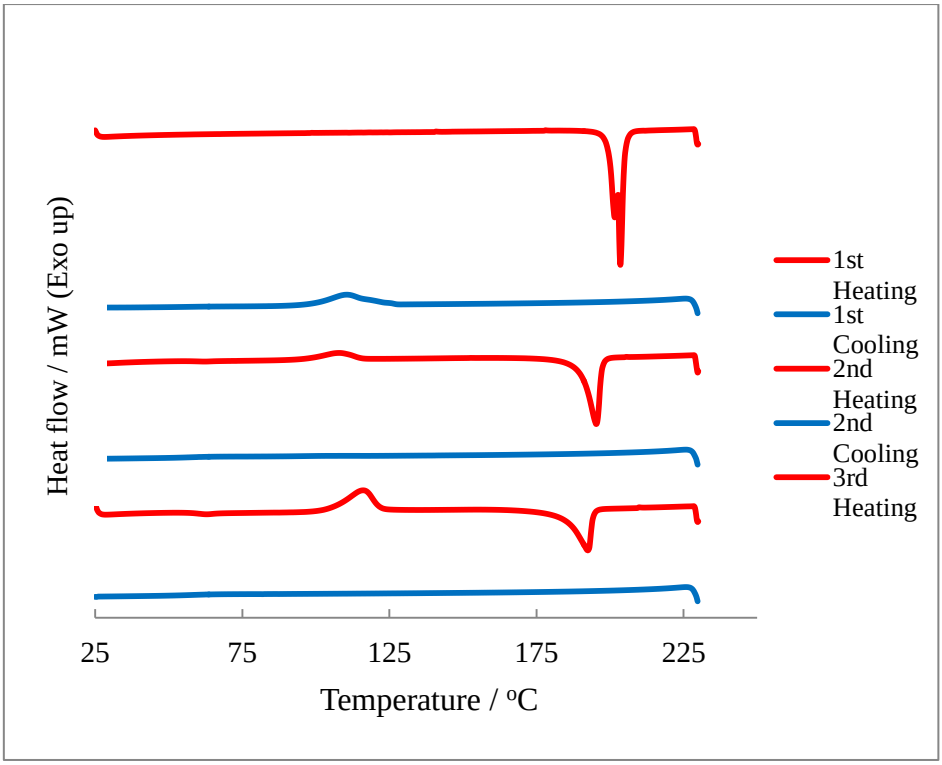


**Figure 33:** DSC trace for **8** where the initial melting is observed as a doublet. Upon cooling and sequential heating crystallization occurs and a new melting point is observed.

For compound **9** the first endothermic thermal event is observed at 97°C and thereafter the melting occurs at 160°C. The sample from which the single crystal for crystal structure studies was obtained was the same sample used for the DSC thermal event determination, which suggests that the crystals are anhydrous. However the thermal event at this temperature is ambiguous to quantify as this temperature closely resembles that of vaporisation of water within crystal lattices. Despite this uncertainty other thermal events occur during the cooling and following heating cycles. During the cooling cycle a slight exotherm peak is observed at 77°C and a further exotherm during the heating cycle until melting is commenced at 149°C. Further cooling yields no significant events.

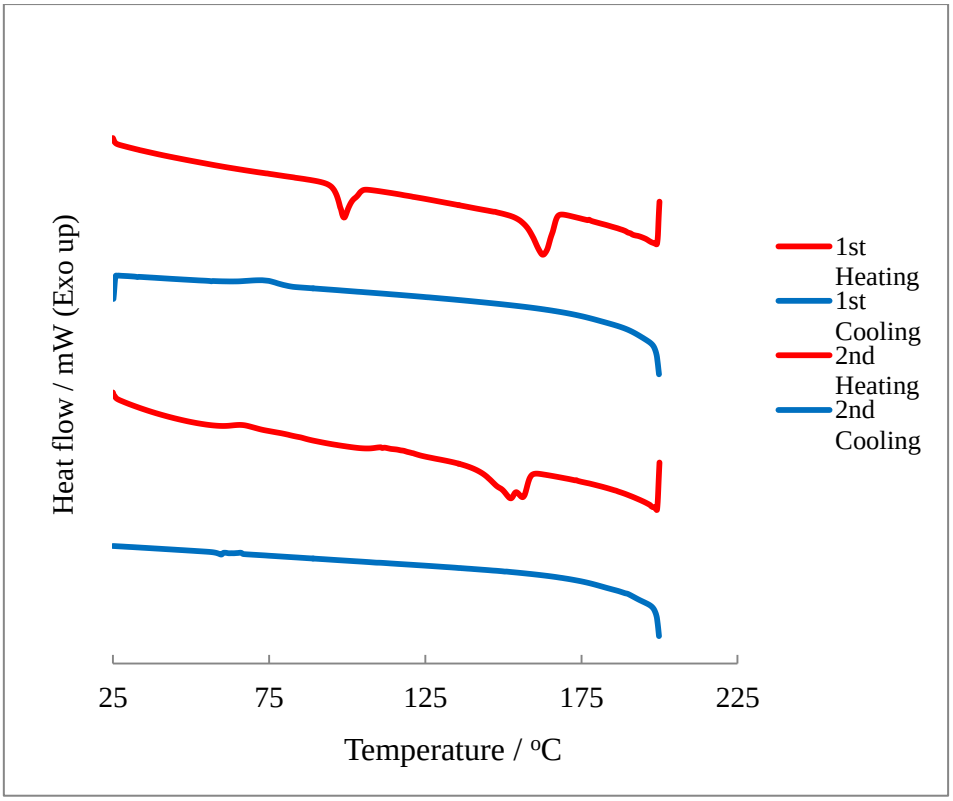


**Figure 34:** DSC trace for **9** where an initial thermal event occurs before melting. During cooling minimal crystallization is observed and upon heating a lower doublet melting point is observed.

The thermal events for **11** are indicative of decomposition at 154°C as no other thermal events are observed for this compound. This trace exemplifies the difficulties faced when trying to recrystallise this compound from melt in an effort to obtain X-ray structure quality crystals. The thermal events for **12** are shown in Figure 36 with the first thermal event (onset of 78°C) represented as a broad endothermic event. This peak occurs around the region for the vaporisation of water, however the single crystal selected from this sample was determined to be anhydrous; further examination is required. After melting no further events are observed which is akin to the thermal behaviour of compound **7**. Overall the compounds exhibit significantly less polymorphic behaviour over ambient and melting point temperatures. It should be noted that the DSC traces for IPH **I**, **II** and **III** initially (see appendices) show no significant thermal behaviour upon heating. However during the cooling cycle the sample will revert to the phase cycle observed in Chapter 3 and hence still shows significant polymorphic behaviour.

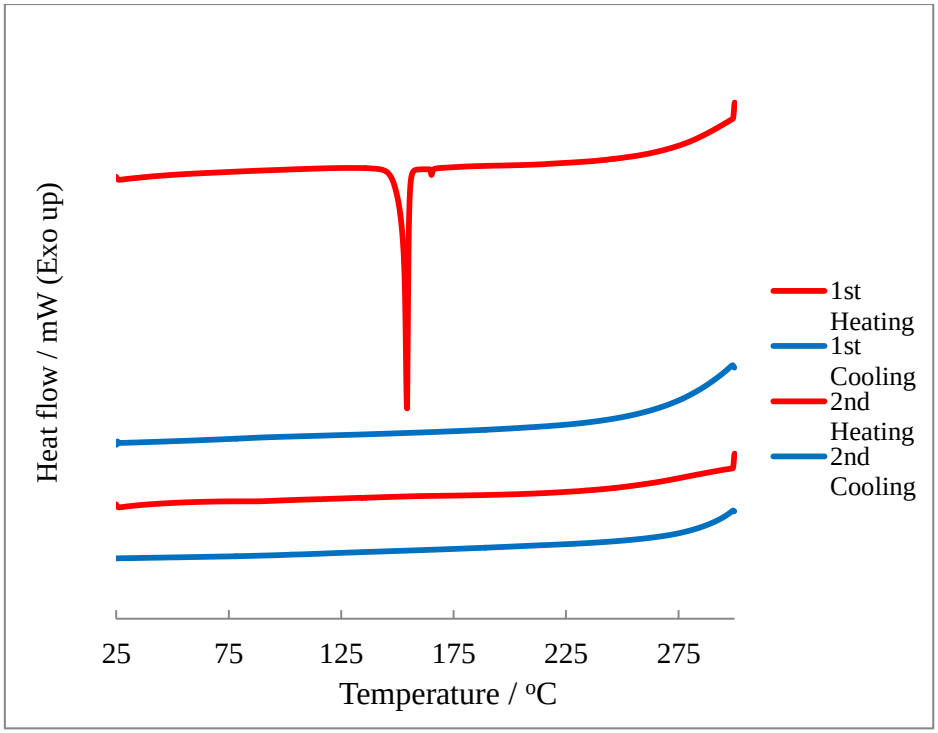


**Figure 35:** DSC trace exemplifying decomposition of **11**.

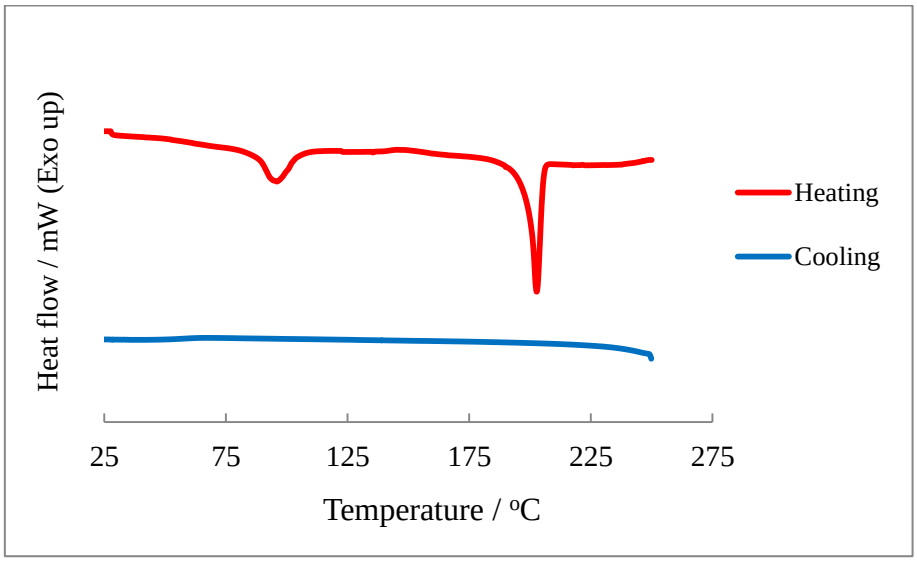


**Figure 36:** DSC trace for **12** where a thermal event occurs with the onset of 78°C thereafter which melting occurs. During cooling, crystallization is not observed.

# CHAPTER 6 CONCLUDING REMARKS AND FUTURE WORK

## 6.1 Concluding remarks

Polymorphism is a well-known phenomenon that requires significant attention during pharmaceutical production as a result of its not predictable appearance. An extreme example of polymorphism in drug compounds has been shown by the investigation of IPH, where six polymorphs of IPH have been identified, characterised and described, when initially only one crystal structure was reported in the literature.[65] Five additional solid state structures have been reported in the present investigation. The analysis of IPH by HSM illustrates that HSM is a powerful and versatile tool for the analysis of polymorphism of drug compounds. The functionality of HSM ranges from crystal growth and melting point analysis to qualitative descriptions of thermal phase transitions. Further analysis of this compound may yield more isolatable polymorphs, becoming a contender for the polymorphic crystal structure record.

The addition of hydrogen bond donors and shifting of pyridyl position in the isoniazid derivatives result in diverse arrangements of molecular aggregations. The shifting of the pyridyl nitrogen atom around the ring induces a slight deviation in the trends of the hydrogen bond motifs; however the deviation is mostly observed when the pyridyl nitrogen is "locked away" at the 2- position of the pyridine ring becoming unavailable to form the hydrogen bonds as demonstrated in the structures with nitrogen at the 3- and 4- position. Higher dimensional motifs using combinations of hydrogen bonds are observed in the structures where the donor and acceptor are aligned in the appropriate manner for hydrogen bond formation. Compounds **1**, **2**, **3**, **5**, **8** and **11** are not viable targets for polymorph investigation by applying thermal methods used in this study. This is because the recrystallization requirements of these derivatives are often difficult to achieve as these compounds solidify as opposed to crystallising after melt. Therefore obtaining new polymorphic forms from the melt may prove to be a fruitless attempt. The overall observed thermal activity for these compounds indicate lack of polymorphic activity. It appears that the polymorphic tendency is reduced when a phenol donor is modified to the phenyl ring and more favourable when an amine group is present for polymorph screening and investigation.

The polymorphic ability of IPH and the molecular interactions and aggregations of compounds **1 - 13** exemplify the application of crystal engineering on molecular structure. The opportunities arising from the nascent field of crystal engineering allows for in-depth crystal structure exploration. Compounds with potential for biological applications such as *N*-isonicotinoyl arylketone hydrazones are an important target to aim for when exploring molecular structure with crystal engineering.

## 6.2 Future work

To broaden the search for further polymorph elucidation, pressure induced structure determination may be applied as a function of constant temperature. This may unlock other unforeseen polymorphs as current work was performed only under ambient pressure. Compounds **4**, **7**, **9** and **12** exhibit the potential for the discovery of further polymorphs, and if further hot-stage and exhaustive solution experiments were to be applied, an array of polymorphs for these compounds may arise. Compound **11** may yet crystallise to afford structure determination quality crystals if the correct solvent system and surrounding conditions are met. Finally, it may be of considerable interest to perform polymorph propensity calculations through the CSD.

## REFERENCES


1. H. Meyer and J. Mally, *Monatshefte für Chemie*, 1912, 33, 393-414.
2. H. H. Fox and J. T. Gibas, *The Journal of Organic Chemistry*, 1953, 18, 983-989.
3. M. Malhotra, S. Sharma and A. Deep, *Med Chem Res*, 2012, 21, 1237-1244.
4. M. Malhotra, G. Sharma and A. Deep, *Acta poloniae pharmaceutica*, 2012, 69, 637-644.
5. M. Malhotra, V. Monga, S. Sharma, J. Jain, A. Samad, J. Stables and A. Deep, *Med Chem Res*, 2012, 21, 2145-2152.
6. C. G. Wermuth, C. R. Ganellin, P. Lindberg and L. A. Mitscher, in *Pure and Applied Chemistry*, 1998, vol. 70, p. 1129.
7. N. K. Nath, S. S. Kumar and n. Nangia, *Cryst. Growth Des.*, 2011, 11, 4594.
8. J. R. Dimmock, S. C. Vashishtha and J. P. Stables, *European Journal of Medicinal Chemistry*, 2000, 35, 241-248.
9. G. Desiraju, *J Chem Sci*, 2010, 122, 667-675.
10. A. Lemmerer, J. Bernstein and V. Kahlenberg, *CrystEngComm*, 2011, 13, 5692-5708.
11. D. Braga, L. Brammer and N. R. Champness, *CrystEngComm*, 2005, 7, 1-19.
12. G. R. Desiraju, *Nature*, 2003, 423, 485-485.
13. P. Ganguly and G. R. Desiraju, *CrystEngComm*, 2010, 12, 817-833.
14. R. Mondal, J. A. K. Howard, R. Banerjee and G. R. Desiraju, *Crystal Growth & Design*, 2006, 6, 2507-2516.
15. R. Banerjee, P. M. Bhatt, M. T. Kirchner and G. R. Desiraju, *Angewandte Chemie International Edition*, 2005, 44, 2515-2520.
16. R. J. Davey, G. Dent, R. K. Mughal and S. Parveen, *Crystal Growth & Design*, 2006, 6, 1788-1796.
17. S. S. Kuduva, D. Bläser, R. Boese and G. R. Desiraju, *The Journal of Organic Chemistry*, 2001, 66, 1621-1626.
18. G. R. Desiraju, *Angewandte Chemie International Edition in English*, 1995, 34, 2311-2327.
19. A. Lemmerer, S. A. Bourne and M. A. Fernandes, *CrystEngComm*, 2008, 10, 1605-1612.
20. B. Moulton and M. J. Zaworotko, *Chemical Reviews*, 2001, 101, 1629-1658.
21. J.-M. Lehn, *Angewandte Chemie International Edition in English*, 1988, 27, 89-112.
22. D. S. Reddy, D. C. Craig and G. R. Desiraju, *Journal of the American Chemical Society*, 1996, 118, 4090-4093.
23. J. Dunitz, *Acta Crystallographica Section B*, 1995, 51, 619-631.
24. C. Desgranges and J. Delhommelle, *Journal of the American Chemical Society*, 2006, 128, 15104-15105.
25. A. Nangia, *Accounts of chemical research*, 2008, 41, 595-604.
26. T. Steiner, *Angewandte Chemie International Edition*, 2002, 41, 48-76.
27. D. Buttar, M. H. Charlton, R. Docherty and J. Starbuck, *Journal of the Chemical Society, Perkin Transactions 2*, 1998, DOI: 10.1039/A706978B, 763-772.
28. A. Bashkirava, P. C. Andrews, P. C. Junk, E. G. Robertson, L. Spiccia and N. Vanderhoek, *Chemistry – An Asian Journal*, 2007, 2, 530-538.
29. G. R. Desiraju, *Accounts of chemical research*, 2002, 35, 565-573.
30. W. Cabri, P. Ghetti, G. Pozzi and M. Alpegiani, *Organic Process Research & Development*, 2006, 11, 64-72.
31. A. J. Aguiar and J. E. Zelmer, *Journal of Pharmaceutical Sciences*, 1969, 58, 983-987.
32. A. J. Aguiar, J. Krc, A. W. Kinkel and J. C. Samyn, *Journal of Pharmaceutical Sciences*, 1967, 56, 847-853.
33. T. Ueto, N. Takata, N. Muroyama, A. Nedu, A. Sasaki, S. Tanida and K. Terada, *Crystal Growth & Design*, 2011, 12, 485-494.
34. R. J. Craven and R. W. Lencki, *Chemical Reviews*, 2013, 113, 7402-7420.
35. A. J. Ardell, *Acta Metallurgica*, 1963, 11, 591-594.
36. H. G. Brittain, *Journal of Pharmaceutical Sciences*, 2002, 91, 1573-1580.
37. J. Haleblian and W. McCrone, *Journal of Pharmaceutical Sciences*, 1969, 58, 911-929.
38. R. Chadha, P. Arora and S. Bhandari, *ISRN Thermodynamics*, 2012, 2012, 8.
39. S. L. Morissette, Ö. Almarsson, M. L. Peterson, J. F. Remenar, M. J. Read, A. V. Lemmo, S. Ellis, M. J. Cima and C. R. Gardner, *Advanced drug delivery reviews*, 2004, 56, 275-300.
40. J. D. Dunitz and J. Bernstein, *Accounts of chemical research*, 1995, 28, 193-200.
41. A. J. Cruz-Cabeza and J. Bernstein, *Chemical Reviews*, 2013, 114, 2170-2191.
42. A. Y. Lee, D. Erdemir and A. S. Myerson, *Annual review of chemical and biomolecular engineering*, 2011, 2, 259-280.

43. R. J. Davey, N. Blagden, G. D. Potts and R. Docherty, *Journal of the American Chemical Society*, 1997, 119, 1767-1772.
44. C. Rustichelli, G. Gamberini, V. Ferioli, M. C. Gamberini, R. Ficarra and S. Tommasini, *Journal of Pharmaceutical and Biomedical Analysis*, 2000, 23, 41-54.
45. A. D. Jana, S. C. Manna, G. M. Rosair, M. G. B. Drew, G. Mostafa and N. Ray Chaudhuri, *Crystal Growth & Design*, 2007, 7, 1365-1372.
46. J. D. Dunitz and A. Gavezzotti, *Angewandte Chemie International Edition*, 2005, 44, 1766-1787.
47. J. D. Dunitz, in *Pure and Applied Chemistry*, 1991, vol. 63, p. 177.
48. L. Yu, *Advanced drug delivery reviews*, 2001, 48, 27-42.
49. T. L. Threlfall, *Analyst*, 1995, 120, 2435-2460.
50. A. Huller, *Faraday Discussions of the Chemical Society*, 1980, 69, 66-74.
51. B. Rodriguez-Spong, C. P. Price, A. Jayasankar, A. J. Matzger and N. Rodriguez-Hornedo, *Advanced drug delivery reviews*, 2004, 56, 241-274.
52. A. Grunenberg, J. O. Henck and H. W. Siesler, *International Journal of Pharmaceutics*, 1996, 129, 147-158.
53. R. Purohit and P. Venugopalan, *Reson*, 2009, 14, 882-893.
54. A. Burger and R. Ramberger, *Mikrochim Acta*, 1979, 72, 273-316.
55. S. Roy, R. Banerjee, A. Nangia and G. J. Kruger, *Chemistry-A European Journal*, 2006, 12, 3777-3788.
56. T. Threlfall, *Organic Process Research & Development*, 2000, 4, 384-390.
57. X. Zhao, X.-Z. Wang, X.-K. Jiang, Y.-Q. Chen, Z.-T. Li and G.-J. Chen, *Journal of the American Chemical Society*, 2003, 125, 15128-15139.
58. N. Blagden, R. J. Davey, H. F. Lieberman, L. Williams, R. Payne, R. Roberts, R. Rowe and R. Docherty, *Journal of the Chemical Society, Faraday Transactions*, 1998, 94, 1035-1044.
59. J. Anwar, S. E. Tarling and P. Barnes, *Journal of Pharmaceutical Sciences*, 1989, 78, 337-342.
60. Bruker, *SAINT+, version 6.02 (including XPREP), Bruker AXS Inc., Madison, WI, USA*, 1999.
61. G. M. Sheldrick, *SHELX, release 97-2 (includes SHELXS and SHELXL), University of Göttingen*, 1997.
62. L. Farrugia, *Journal of Applied Crystallography*, 1997, 30, 565.
63. A. Spek, *Journal of Applied Crystallography*, 2003, 36, 7-13.
64. H. Putz and K. Brandenburg, *Diamond Version. 3.0e - Crystal and Molecular Structure Visualization - Crystal Impact GbR, Kreuzherrenstr. 102, 53227 Bonn, Germany*.
65. J.-h. Jiang, J. Chen, J. Yang and F.-F. Jian, *Acta Crystallographica Section E*, 2009, 65, o3125.
66. S. Chen, I. A. Guzei and L. Yu, *Journal of the American Chemical Society*, 2005, 127, 9881-9885.
67. V. López-Mejías, J. W. Kampf and A. J. Matzger, *Journal of the American Chemical Society*, 2012, 134, 9872-9875.
68. O. Reany, M. Kapon, M. Botoshansky and E. Keinan, *Crystal Growth & Design*, 2009, 9, 3661-3670.
69. M. C. Etter, *Acc. Chem. Res.*, 1990, 23, 120.
70. J. Bernstein, R. E. Davis, L. Shimoni and N.-L. Chang, *Angewandte Chemie International Edition in English*, 1995, 34, 1555-1573.
71. A. Burger and R. Ramberger, *Mikrochim Acta*, 1979, 72, 259-271.
72. S. M. S. V. Wardell, M. V. N. de Souza, J. L. Wardell, J. N. Low and C. Glidewell, *Acta Crystallographica Section B*, 2007, 63, 879-895.
73. S.-S. Chen, S.-P. Zhang, C.-B. Huang and S.-C. Shao, *Acta Crystallographica Section E*, 2006, 62, o31-o32.
74. X. S. Tai and F. Y. Kong, in *Zeitschrift für Kristallographie - New Crystal Structures*, 2006, vol. 221, p. 341.

# APPENDICES

## 1.1 Supporting Information for polymorphism studies of IPH

### 1.1.1 Representative DSC traces for IPH I – III

IPH **I**

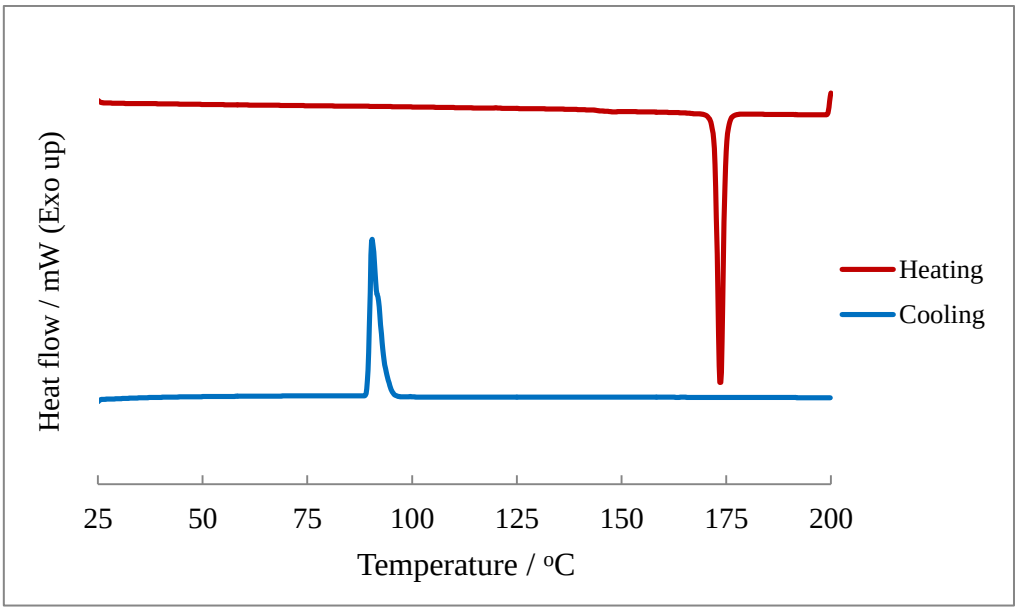


**Figure A1**: Representative DSC trace for numerous experiments for the melting and cool of IPH **I**. The DSC trace exemplifies the single melting endotherm characteristic of IPH **I**.

IPH **II**

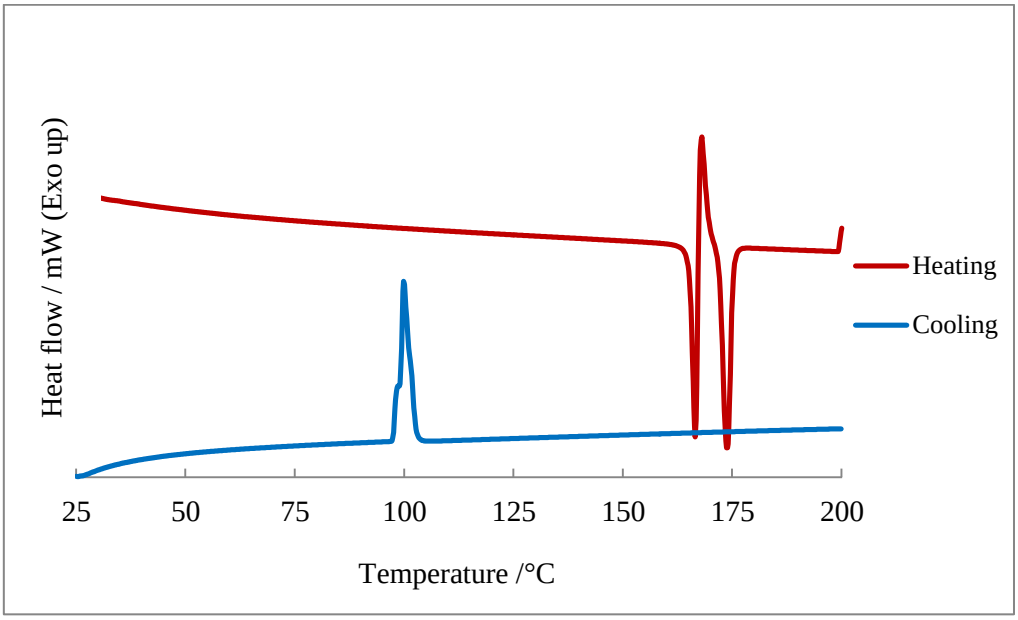


**Figure A2**: Representative DSC trace for numerous experiments for the melting and cool of IPH **II**. The DSC trace shows the melting point of IPH **II** and subsequent recrystallization and melt of IPH **I**.

IPH **III**

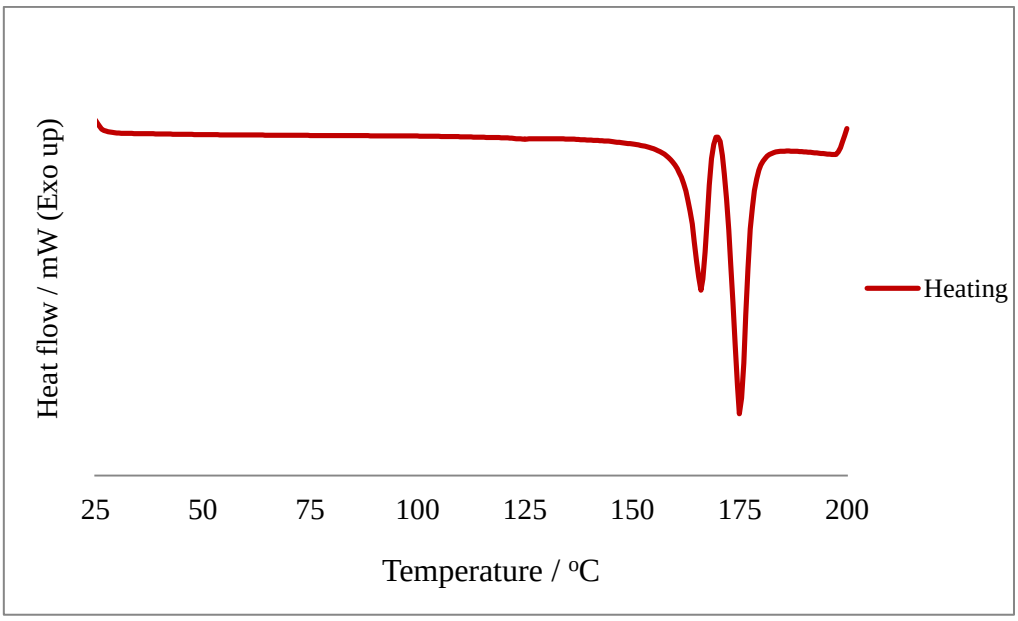


**Figure A3**: Representative DSC trace for numerous experiments for the melting and cool of IPH **III**. The DSC trace shows a similar behaviour as IPH **II**; however the onset of melt for the endotherm has shifted to 161.1°C indicating a different melting point.

### 1.1.2 Powder X-ray diffraction patterns for forms IPH I – III and V

IPH **I**

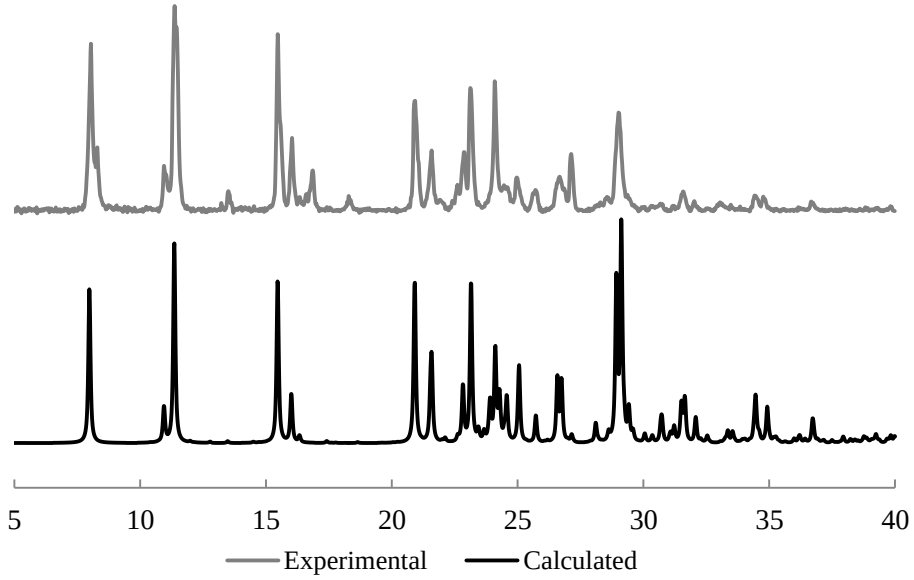


**Figure A4**: PXRD of IPH **I** compared to PXRD of single crystal structure determination of IPH **I**. The experimental pattern was calculated at room temperature and the calculated pattern at 173 K.

IPH **II**

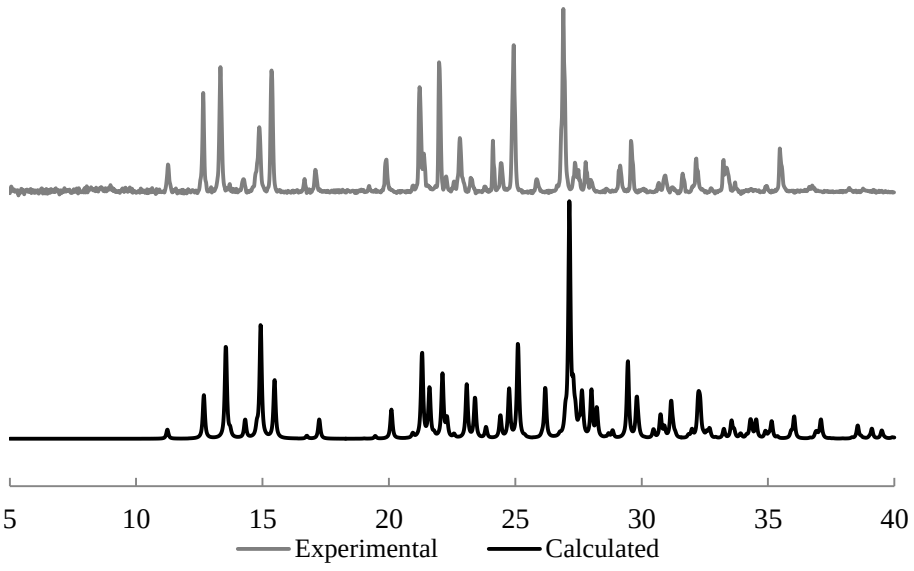


**Figure A5**: PXRD of IPH **II** compared to PXRD of single crystal structure determination of IPH **II**. The experimental pattern was calculated at room temperature and the calculated pattern at 173 K.

IPH **III**

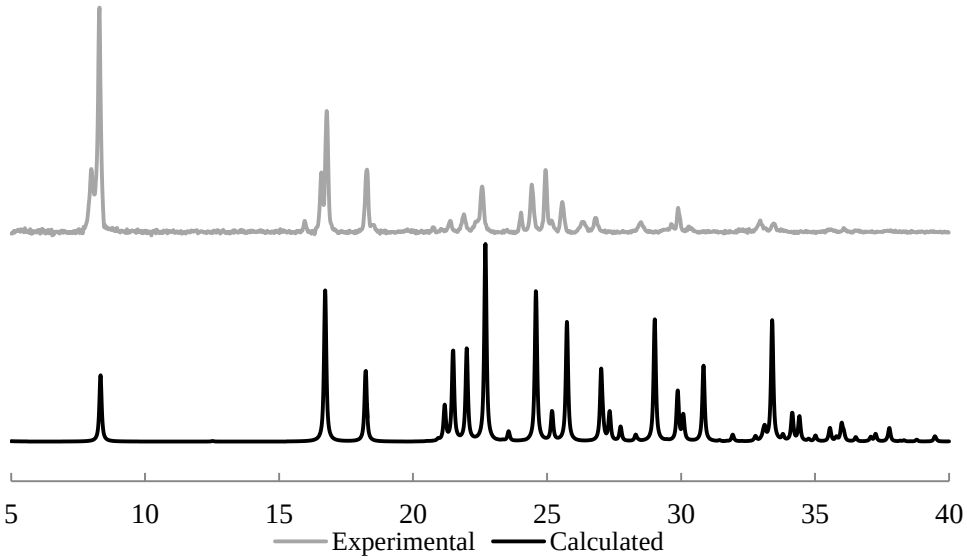


**Figure A6**: PXRD of IPH **III** compared to PXRD of single crystal structure determination of IPH **III**. The experimental pattern was calculated at room temperature and the calculated pattern at 173 K.

IPH **V**

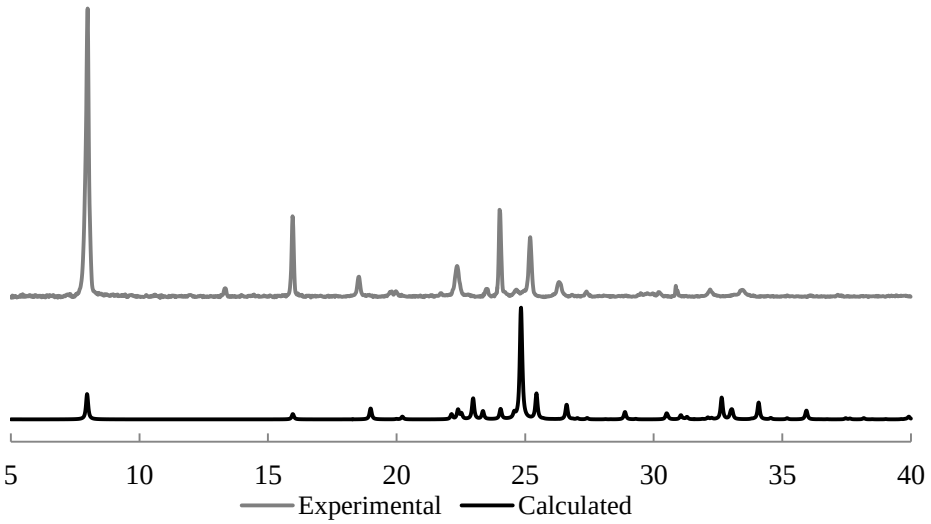


**Figure A7**: PXRD of IPH **V** compared to PXRD of single crystal structure determination of IPH **V**. The experimental pattern was calculated at room temperature and the calculated pattern at 173 K.

### 1.1.3 FT-IR and Raman spectra of IPH I – III and V

FT-IR spectra of IPH **I** – **III** and **V**

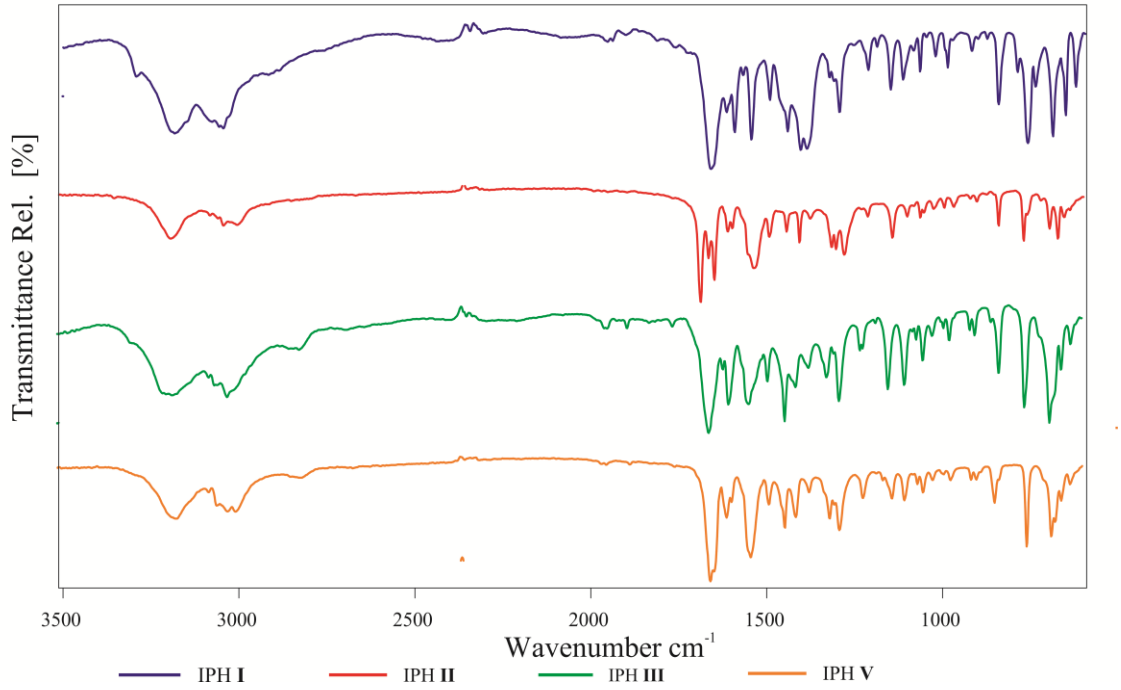


**Figure A8**: FT-IR spectra of IPH **I** – **III** and **V**. A spectrum for IPH **IV** and **VI** is unavailable as result from the insufficient quantities recovered.

Raman spectroscopy of IPH **I** – **III** and **V**

IPH **I**

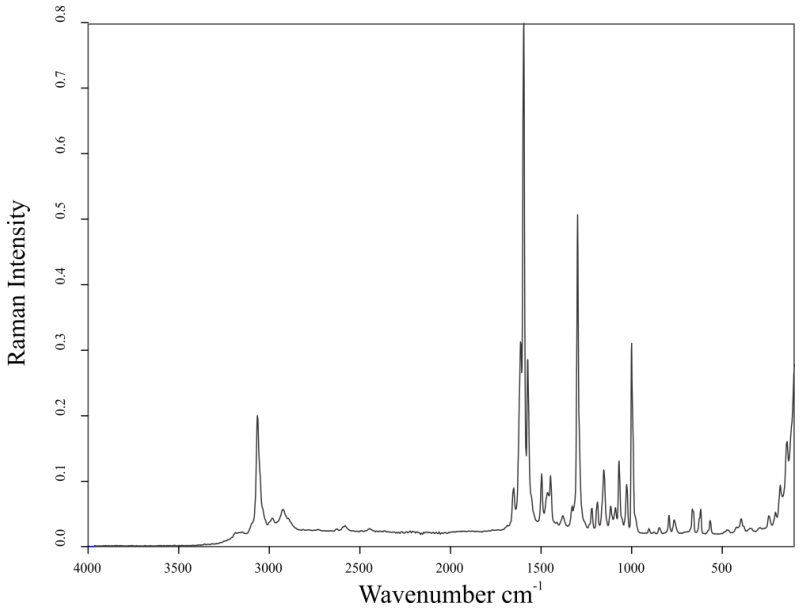


**Figure A9**: Raman spectrum of IPH **I**.

IPH **II**

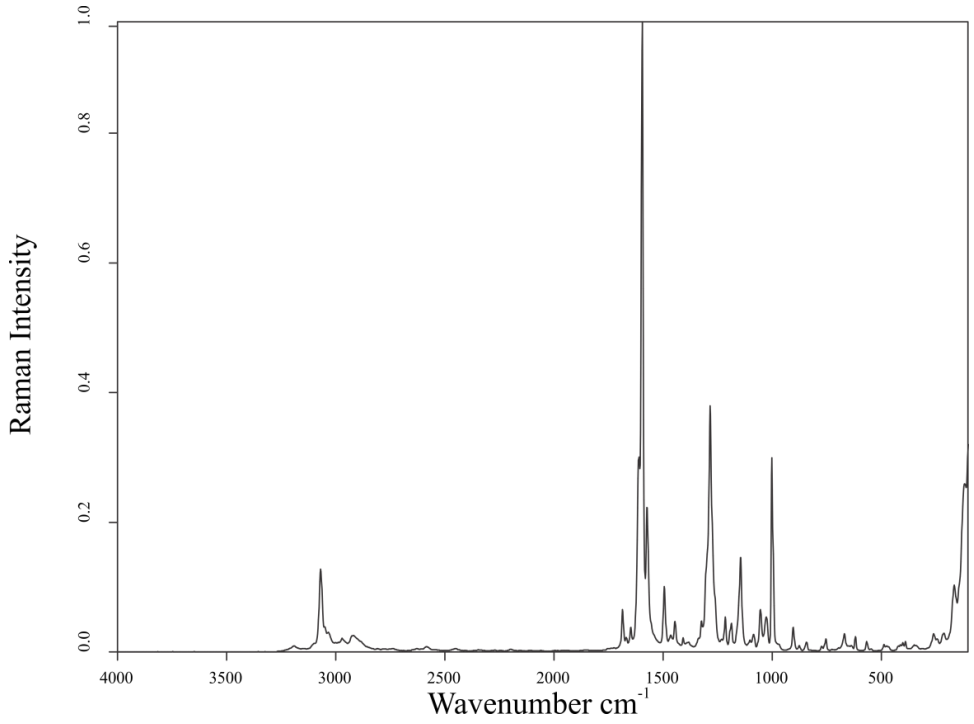


**Figure A10**: Raman spectrum of IPH **II**.

IPH **III**

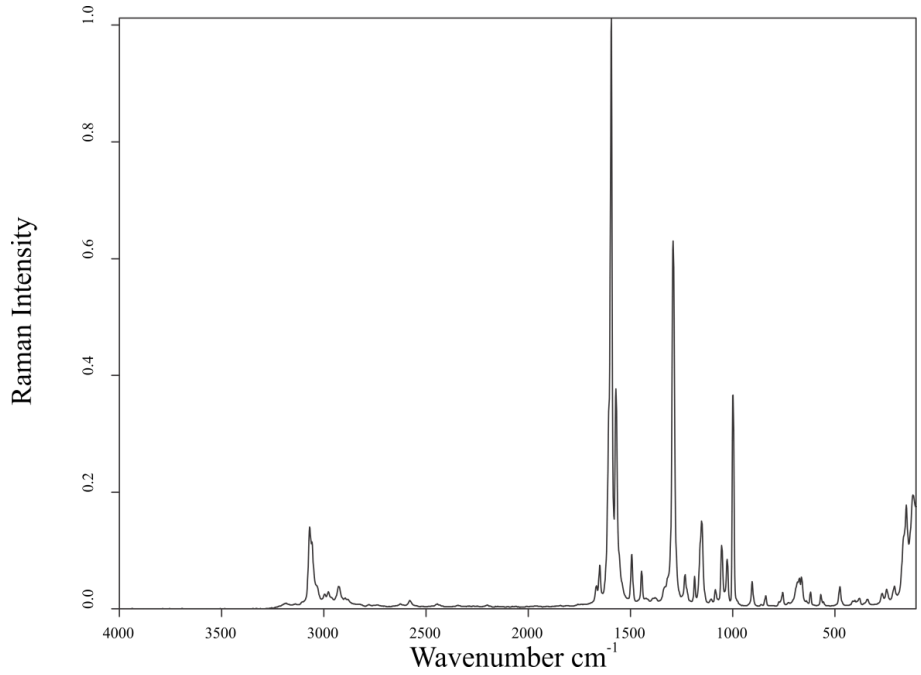


**Figure A11**: Raman spectrum of IPH **III**.

IPH **V**

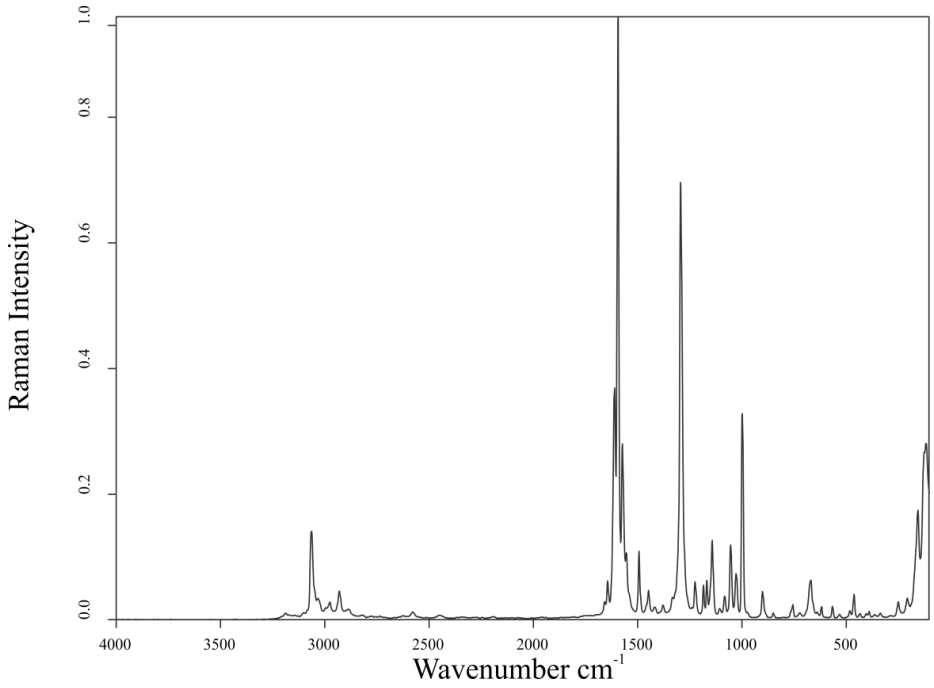


**Figure A12**: Raman spectrum of IPH **V**.

## 1.2 Supporting thermal activity information for supramolecular aggregate studies of isoniazid derivatives

Compound **2**

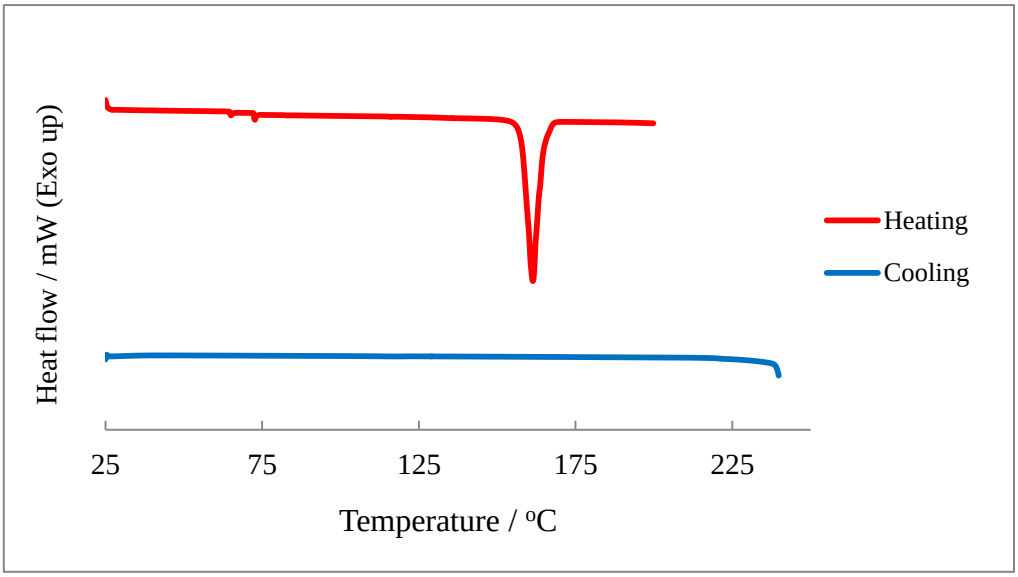


**Figure A13**: Representative DSC trace for numerous experiments for the melting and cool of **2**.

Compound **3**

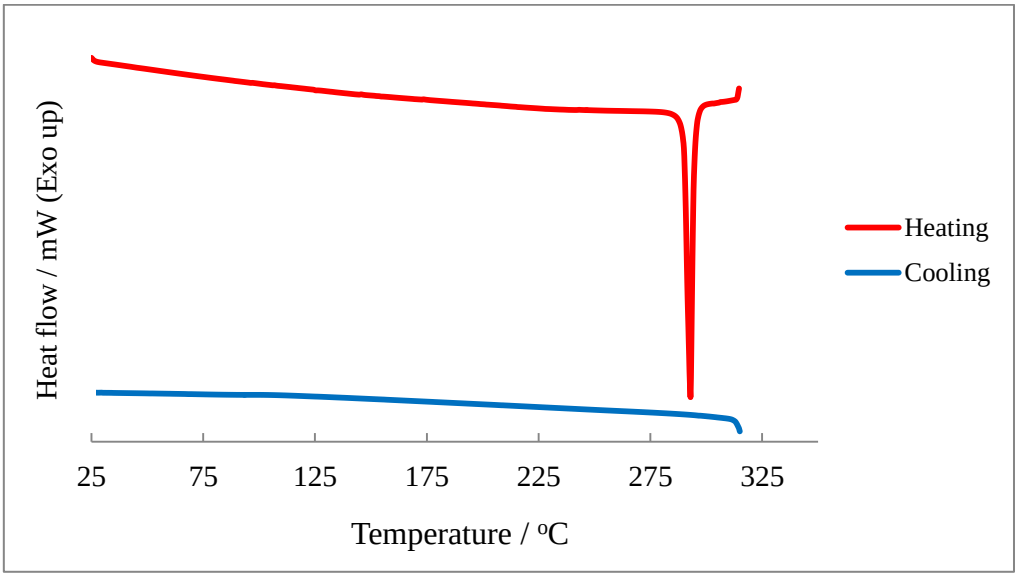


**Figure A14**: Representative DSC trace for numerous experiments for the melting and cool of **3**.

Compound **5**

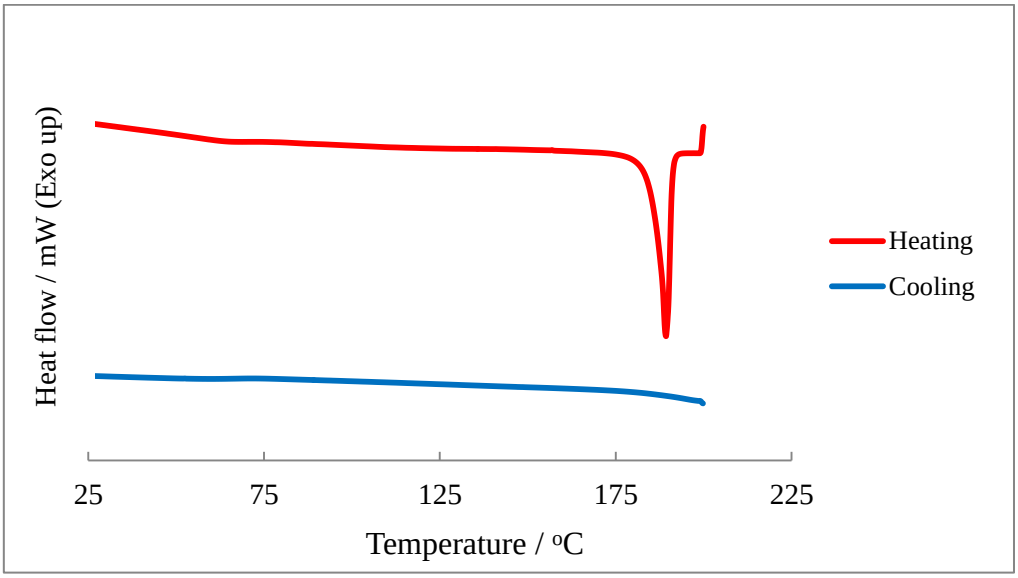


**Figure A15**: Representative DSC trace for numerous experiments for the melting and cool of **5**.

Compound **6**

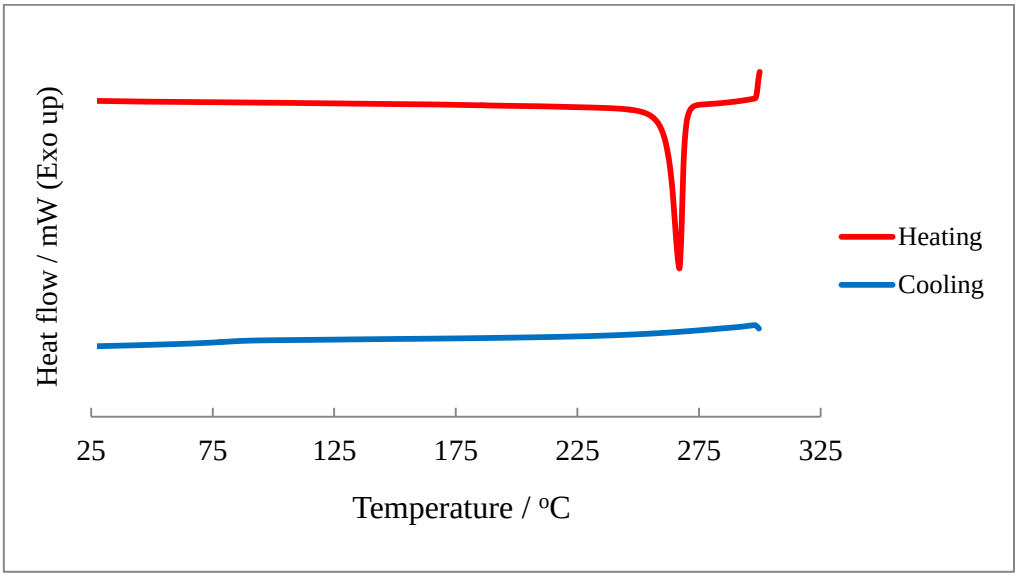


**Figure A16**: Representative DSC trace for numerous experiments for the melting and cool of **6**.

Compound **7**

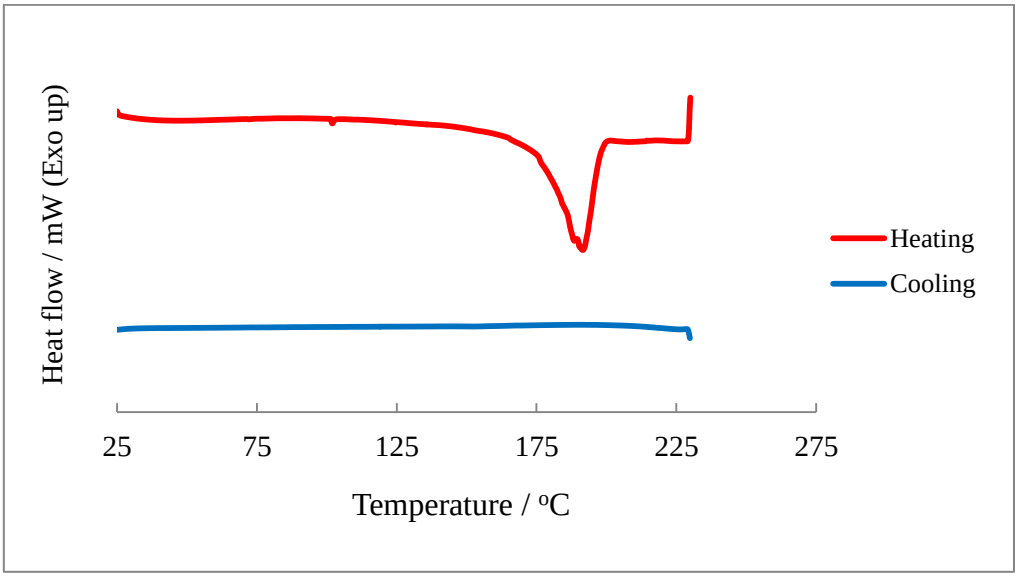


**Figure A17**: Representative DSC trace for numerous experiments for the melting and cool of **7**.

Compound **10**

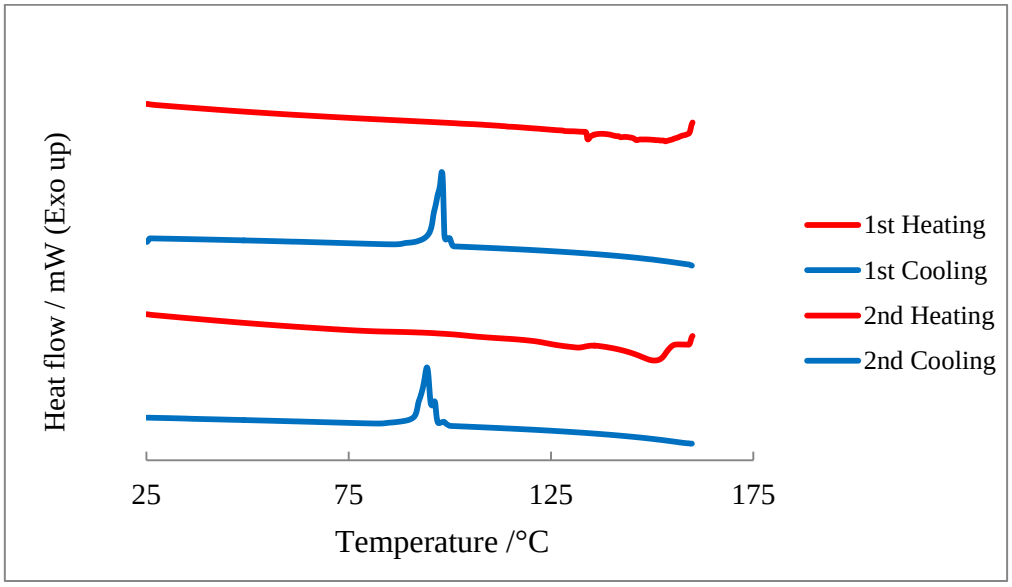


**Figure A18**: Representative DSC trace for numerous experiments for the melting and cool of **10**.

Compound **13**

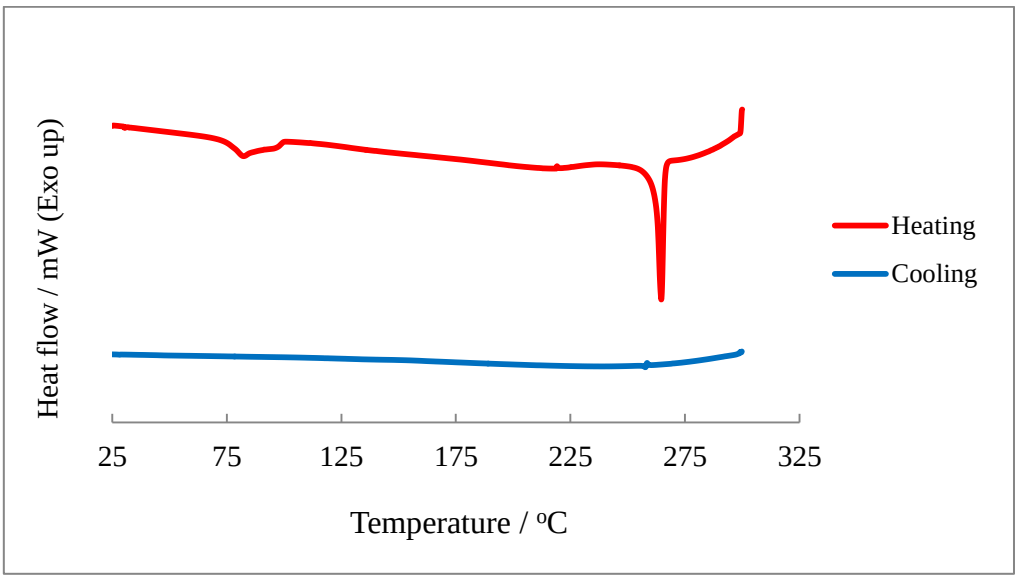


**Figure A19**: Representative DSC trace for numerous experiments for the melting and cool of **13**.